AD-A164 253 THERMODYNAMICS OF HIGH TEMPERATURE MATERIALS(U) 1/2
NATIONAL BUREAU OF STANDARDS GAITHERSBURG MD
S ABRAMOWITZ 24 DEC 85 AFOSR-TR-86-0008
UNCLASSIFIED AFOSR-85-ISSA-00029 F/G 11/2 NL

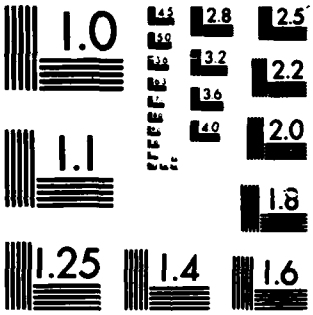

MICROCOPY RESOLUTION TEST CHART

NATIONAL BUREAU OF STANDARDS-1963-A

AFOSR-TR- 86-0008

(2)

Thermodynamics of High Temperature Materials

Annual Report for the Period

1 October 1984 - 30 September 1985

AIR FORCE OFFICE OF SCIENTIFIC RESEARCH

AFOSR-ISSA-85-00029

AD-A164 253

DTIC FILE COPY

DTIC
ELECTE
FEB 12 1986
S D
B

Approved for public release;
distribution unlimited.

86 2 11 114

UNCLASSIFIED
SECURITY CLASSIFICATION OF THIS PAGE

AD-A164 353

REPORT DOCUMENTATION PAGE

1a. REPORT SECURITY CLASSIFICATION UNCLASSIFIED	1b. RESTRICTIVE MARKINGS
2a. SECURITY CLASSIFICATION AUTHORITY	3. DISTRIBUTION/AVAILABILITY OF REPORT Approved for public release; distribution unlimited.
2b. DECLASSIFICATION/DOWNGRADING SCHEDULE	
4. PERFORMING ORGANIZATION REPORT NUMBER(S)	5. MONITORING ORGANIZATION REPORT NUMBER(S) AFOSR-TR- 86-0008
6a. NAME OF PERFORMING ORGANIZATION National Bureau of Standards 6b. OFFICE SYMBOL (If applicable)	7a. NAME OF MONITORING ORGANIZATION Air Force Office of Scientific Research/NE
6c. ADDRESS (City, State and ZIP Code) United States Department of Commerce National Bureau of Standards Gaithersburg, Maryland 20899	7b. ADDRESS (City, State and ZIP Code) Building 410 Bolling AFB Washington, DC 20332-6448
8a. NAME OF FUNDING/SPONSORING ORGANIZATION AFOSR/ 8b. OFFICE SYMBOL (If applicable) NE	9. PROCUREMENT INSTRUMENT IDENTIFICATION NUMBER AFOSR-85-ISSA-00029
8c. ADDRESS (City, State and ZIP Code) Building 410 Bolling AFB Washington, DC 20332-6448	10. SOURCE OF FUNDING NOS. PROGRAM ELEMENT NO.: 61102F PROJECT NO.: 2306 TASK NO.: A2 WORK UNIT NO.:
11. TITLE (Include Security Classification) Thermodynamics of High-Temperature Materials	
12. PERSONAL AUTHOR(S) Stanley Abramowitz	
13a. TYPE OF REPORT ANNUAL 13b. TIME COVERED FROM 1 Oct 84 TO 30 Sep 85	14. DATE OF REPORT (Yr., Mo., Day) 24 December 85 15. PAGE COUNT 124
16. SUPPLEMENTARY NOTATION	

17. COSATI CODES			18. SUBJECT TERMS (Continue on reverse if necessary and identify by block number)
FIELD	GROUP	SUB. GR.	
			Thermodynamic, Photodissociation, Franck-condon.

19. ABSTRACT (Continue on reverse if necessary and identify by block number)

The research described encompasses six tasks each of which treats, from either an experimental or theoretical base, the measurement or interpretation of the high-temperature thermophysical behavior of model systems. Measurements have been initiated in a specifically designed apparatus using state of the art pyronetery, to measure the triple point of graphite by a pulse heating method. Thermodynamic properties of silicon nitride (a, b) and boron nitride (hex, cub) have been determined to 1300K. Calculational algorythms have been developed to calculate photodissociation cross sections for broad band continuum transitions, including molecular dissociation. Preliminary calculations have been performed to study the pressure broadening of atomic and molecular species in strong laser fields. Franck-condon matrix elements for bound-continuum transitions are being used to obtain estimates of total cross-sections. A combined theoretical and experimental program is being pursued to increase the understanding of the relationship of structure and reactivity of graphitic structures.

20. DISTRIBUTION/AVAILABILITY OF ABSTRACT UNCLASSIFIED/UNLIMITED ☒ SAME AS RPT. ☒ DTIC USERS ☐	21. ABSTRACT SECURITY CLASSIFICATION UNCLASSIFIED
22a. NAME OF RESPONSIBLE INDIVIDUAL Maj Joseph Hager	22b. TELEPHONE NUMBER (Include Area Code) 202-767-4933 22c. OFFICE SYMBOL NE

DD FORM 1473, 83 APR EDITION OF 1 JAN 73 IS OBSOLETE.

UNCLASSIFIED
SECURITY CLASSIFICATION OF THIS PAGE

Results of this investigation have been interpreted in terms of the number of available reactive sites. The rates and mechanism of ionic polymerization in highly unsaturated organic compounds, structures and thermochemistry of relevant ions, photdissociation of the polymeric ions, and the repair mechanisms which generate polymeric ions after photodissociation have been studied. The work focusses on the elucidation of the gas phase polymerization and reactions mechanisms following laser irradiation induced breakdown in aromatic hydrocarbons, particularly those with acetylenic and olefinic side chains such as phenylacetylene and phenylethylene (styrene). Development of apparatus and techniques to study the molecular basis for laser induced vaporization of refractory materials such as graphite continued. Special features in the vaporization of graphite have been examined. The gas phase species from C(1) to C(5) have been observed.

TABLE OF CONTENTS

CHAPTER	PAGE
Abstract	iii
I. Research on Thermophysical Properties	1
a. Preliminary Measurements of the Triple Point Temperature of Graphite by a Pulse Heating Technique	1
II. High Temperature Enthalpy Measurements	12
a. Thermodynamic Properties of Environmentally Resistant Ceramics and Refractories	12
b. Heat Capacity of bcc Calcium; Enthalpy of fcc/bcc Transition	16
III. Broad Band Spectroscopy of Small Molecules in Intense Laser Fields	23
a. Analytic Multichannel Theory of Molecular Dissociation	27
b. A Convergent Analysis of Radiative Matrix Elements in Atomic Lineshape Theory	37
IV. Growth and Decomposition of Graphitic Structures	71
V. Build Up and Irradiation of Obscuring Clouds Under Near Vacuum Conditions - Application to Spacecraft Survivability and	88
VI. Molecular Basis for Laser Induced Vaporization of Refractory Materials	96

Keywords: heat resistant materials; photodissociation; silicon nitrides; sporogation; graphite; ceramics; boron nitrides.

Accession For
NTIS GRA&I ☑
DTIC TAB ☐
Unannounced ☐
Justification
Distribution/
Availability Codes
Dist
A-1

AIR FORCE OFFICE OF SCIENTIFIC RESEARCH (AFSC)
NOTICE OF TRANSMITTAL TO DTIC
This technical report has been reviewed and is
approved for public release IAW AFR 190-12.
Distribution is unlimited.
MATTHEW J. KERPER
Chief, Technical Information Division

DTIC
ELECTE
FEB 1 2 1986
S D
B

ABSTRACT

The research described encompasses six tasks each of which treats, from either an experimental or theoretical base, the measurement or interpretation of the high-temperature thermophysical behavior of model systems which show potential applications to the environmental resistant materials and the spacecraft survivability programs. While there is significant overlap between these tasks, the first two chapters are addressed to the environmental resistant materials programs, while the later four chapters are addressed to the spacecraft survivability program.

Measurements have been initiated, in a specially designed apparatus using state of the art pyrometery, to measure the triple point of graphite by a pulse heating method. Preliminary results indicate that the surface radiance temperature of melting graphite at effective wavelengths between 0.5 and 0.9 micrometers are in the range of 4300 to 4400 K.

Thermodynamic properties of silicon nitride (α, β) and boron nitride (hex, cub) have been determined to 1300 K. The heat capacity of bcc calcium has been determined in the range of 273 to 929 K. The enthalpy of the phase transition to fcc structure has also been determined. These data are to be used to test theories and models for predicting the thermodynamic properties of metals.

Calculational algorithms have been developed to calculate photodissociation cross sections for broad band continuum transitions, including molecular dissociation. Preliminary calculations have been performed to study the pressure broadening of atomic and molecular species in strong laser fields. Franck-Condon matrix elements for bound-continuum transitions are being used to obtain estimates of total cross-sections.

A combined theoretical and experimental program is being pursued to increase the understanding of the relationship of structure and reactivity of graphitic structures. Kinetics of the phenyl radical deposition on pyrolytic graphite surfaces have been investigated. Results of this investigation have been interpreted in terms of the number of available reactive sites.

The rates and mechanism of ionic polymerization in highly unsaturated organic compounds, structures and thermochemistry of relevant ions, photodissociation of the polymeric ions, and the repair mechanisms which generate polymeric ions after photodissociation have been studied. The work focusses on the elucidation of the gas phase polymerization and reactions mechanisms following laser irradiation induced breakdown in aromatic hydrocarbons, particularly those with acetylenic and olefinic side chains such as phenylacetylene and phenylethylene (styrene). Kinetics and mechanisms of the reactions of phenyl ions were also examined, and structures of this species generated from a number of organic molecules have been elucidated.

Development of apparatus and techniques to study the molecular basis for laser induced vaporization of refractory materials such as graphite continued. Special features in the vaporization of graphite have been examined. The gas phase species from C_1 to C_5 have been observed. The computation of thermodynamic temperature using the ratios of these species observed using mass spectrometric techniques have been elucidated. The effects of laser energy on the mass spectrum have also been studied.

PRELIMINARY MEASUREMENTS OF THE TRIPLE-POINT TEMPERATURE OF GRAPHITE BY A PULSE-HEATING TECHNIQUE

A. Cezairliyan, A. P. Miiller and J. L. McClure

ABSTRACT

Measurements have been initiated to accurately determine the triple-point temperature of graphite by a rapid pulse-heating technique. The basic method involves heating the specimen in a pressurized inert gas environment (14 MPa) from room temperature to the melting temperature in less than 0.1 s by the passage of an electrical current pulse through it; and simultaneously determining the specimen temperature every 0.1 ms by means of a newly-constructed pyrometer which measures the spectral radiance temperatures in six wavebands. Final testing and calibration of the multi-wavelength pyrometer is near completion. Preliminary results indicate that the surface radiance temperatures of melting graphite at effective wavelengths between 0.5 and 0.9 μm are approximately in the range 4300 to 4400 K.

1. INTRODUCTION

The solid-liquid-vapor triple point of graphite has been the subject of numerous studies, particularly during the past decade or so; reviews of the investigations may be found in the literature [1,2]. Although most measurements yield a triple-point pressure of about 110 atm, considerable controversy still exists as to the triple-point temperature with reported values spanning the range of approximately 4000 to 5000 K. A major problem in such measurements arises from the high vapor pressure of graphite: a plume of cooler carbon vapor (in the form of soot) forms near the specimen surface as the triple point is approached, thereby severely limiting the accuracy of optical pyrometry.

A feasibility study [3] was performed recently in our laboratory to determine if the effects of specimen evaporation

on pyrometric temperature measurements could be suppressed, or at least minimized. Surface radiance data, obtained by means of a single-wavelength (0.65 μm) high-speed pyrometer, showed that a reasonably well-defined melting plateau in the temperature-time function could be obtained under certain conditions: (1) a small amount of oxygen (10 to 30%) must be added to the inert gas environment of the specimen. The carbon vapor combines with the oxygen to form optically transparent gases CO and CO_2; (2) the specimens must be rapidly heated at rates of about 10^5 $K \cdot s^{-1}$ or higher. The very short heating times (less than 0.1 s) tend to minimize the effects of convective turbulence in the sighting path of the pyrometer.

As a result of this study, a multi-wavelength pyrometer was designed and constructed [4] to provide a means of estimating the true temperature of a specimen from surface radiance data. The final testing and calibration of this instrument is nearing completion.

In the present report, we briefly describe (1) the major components of the measurement system and (2) preliminary results obtained from measurements on graphite with the multi-wavelength pyrometer at temperatures in the vicinity of the triple-point.

2. MEASUREMENT SYSTEM

The high-speed measurement system includes an electric power-pulsing circuit and its associated measuring and control circuits, a high-pressure experiment chamber, a multi-wavelength pyrometer, and a data acquisition system. A functional diagram

of the measurement system is shown in Fig. 1.

2.1. Pulsing Circuit

The power-pulsing circuit consists of the specimen in series with a battery bank, an adjustable resistance (water-cooled Inconel tube), and a fast acting switch. Adjustments to the battery bank voltage (up to 38 V) and to the length (hence, resistance) of the Inconel tube in the circuit, prior to pulse heating, enable control of the specimen heating rate. The timing of various events, such as closing and opening of the switch and triggering of electronic instruments, is achieved by means of time-delay pulse generators.

2.2. Experiment Chamber

The experiment chamber is an ultra-high pressure cell capable of providing an inert gas environment at pressures up to 200 MPa (~ 2000 atm). Two optical ports through the cylindrical wall on opposite sides of the vessel (viewing cone of about 20°) facilitate the alignment of the specimens and provide a sighting path for the pyrometer through sapphire windows (diameter, 25 mm; thickness, 32 mm). The specimen/mount assembly is supported from the closure head which contains electrical feedthroughs for the pulse-heating current.

The specimen is clamped onto two electrodes in the mounting assembly: a stationary lower electrode and an upper electrode which is connected to an expansion joint (flexible phosphor-bronze bellows). This arrangement allows for thermal expansion of the specimen along its axial direction during rapid pulse heating.

2.3. Specimens

The specimen material, designated by the manufacturer as POCO AXM-5Q1 graphite, was supplied in the form of thin (0.5 mm) sheets. The specimens were fabricated into rectangular strips with nominal dimensions of 25 mm long by 3 mm wide. The center portion of each specimen was then "necked-down" to define an "effective" portion of the specimen which undergoes melting. The dimensions of the effective specimen were nominally: length, 2 mm; width, 1 mm; thichness, 0.5 mm.

2.4. Multi-Wavelength Pyrometer

The pyrometer is capable of measuring the spectral radiance temperatures of a rapidly heating speacimen in six wavebands with a time response of 50 μs (for each spectral band). Thermal radiation from a circular target area (0.5 mm diameter) on the specimen is focussed by the lens system in the pyrometer onto a fiber optic bundle. The latter is divided (nominally at random) into six separate bundles which illuminate six interference filters and silicon diode detectors. Five of the interference filters have a spectral bandwidth of about 0.1 μm, centered at 0.5, 0.6, 0.7, 0.8 and 0.9 μm. The sixth filter has a bandwidth of 0.03 μm centered at 0.65 μm. The photocurrents from the diodes are converted by high-stability amplifiers to proportionate voltages, which are switched sequentially every 0.1 ms through a multiplexer to the pyrometer output.

The calibration of the pyrometer involves two steps. First, the 0.65 μm channel is calibrated in a steady state

experiment with a tungsten-filament standard lamp which, in turn, had been calibrated against the NBS Photoelectric Pyrometer operating at the same effective wavelength. The calibration is then transferred to the other five channels by dynamically recording the radiation from a blackbody hole in a graphite tube as it is heated by a pulse of electric current.

Additional details concerning the design, operation and calibration of the multi-wavelength pyrometer are given elsewhere [4].

2.5. Data Acquisition

The multiplexed analog signals from the pyrometer are digitized (15-bit resolution) and stored by a digital oscilloscope having a memory capacity of 16K data points. The timebase of the digital oscilloscope is supplied by the pyrometer electronics which provide a sequence of TTL-compatible "memory-address advance" pulses synchronous with the multiplexer switching. After each experiment, the data is transferred from the oscilloscope to an off-line computer for subsequent analyses.

3. MEASUREMENTS AND PRELIMINARY RESULTS

During the course of successive calibration experiments, the new pyrometer was found to exhibit a long-term drift in its response. As a result of extensive testing of pyrometer components, the source of instability was determined to be the interference filters. Replacement filters were ordered and should be available early in FY86. In spite of the instability,

however, useful information could still be obtained with the pyrometer and therefore, the series of pulse experiments to determine the triple-point temperature of graphite was begun.

Prior to each pulse experiment, a strip specimen was mounted in the experiment cell which was then pressurized to 14 MPa ($\sim$ 140 atm) with an argon/oxygen gas mixture; the oxygen content varied with experiment between 5 and 33 %. The specimen was then rapidly heated from room temperature to its melting temperature in less than 0.1 s by passing an electrical current pulse through it. The duration of the current pulse ranged from approximately 40 to 70 ms. Heating rates were nominally between 1.5 and 3 x 10^5 $K \cdot s^{-1}$.

The results of a typical pulse experiment are presented in Fig. 2 which illustrates the variation of spectral radiance from the specimen surface with time, as measured by the six channels of the pyrometer. Plateaus in the radiance versus time functions indicate that the specimen has undergone melting. Further evidence of melting may be seen in Fig. 3 which shows that the surface of the remaining portion of effective specimen is glassy in appearance.

For a given experiment, radiance temperatures along the flat portion of the melting plateau were averaged for each channel. A typical mean value involved approximately 15 temperatures and a standard deviation of about 10 K.

The mean values of radiance temperature coresponding to the 0.65 μm channel are plotted in Fig. 4 as a function of oxygen content in the pressurizing gas environment. As may be

seen, the measured radiance temperature (at 0.65 μm) of graphite at the triple point decreases linearly with decreasing oxygen content. A similar behavior was observed in the results recorded by the other five channels. This effect appears to arise from the reaction of excess oxygen with carbon in the specimen surface, which suggests that the "correct" value of radiance temperature at melting may be determined by extrapolation of the measured results to zero oxygen content.

The preliminary results indicate that the radiance temperatures of graphite at its triple point for effective wavelengths between 0.5 and 0.9 μm are approximately in the range 4300 to 4400 K. However, no reliable estimate of the true triple-point temperature could be made because of the uncertainties created by the unstable interference filters in the pyrometer.

The final testing and calibration of the pyrometer will be completed early in FY86 after replacing the filters with more stable units. Subsequent pulse experiments should then enable an accurate determination of the triple-point temperature of graphite.

REFERENCES

[1] F. P. Bundy, J. Geophysical Research 85, 6930 (1980).

[2] M. A. Sheindlin, High Temperature 19, 467 (1981).

[3] A. Cezairliyan, A. P. Miiller and J. L. McClure, Report AFOSIR-ISSA-83-00038, 1983, p.1.

[4] G. M. Foley, to be published.

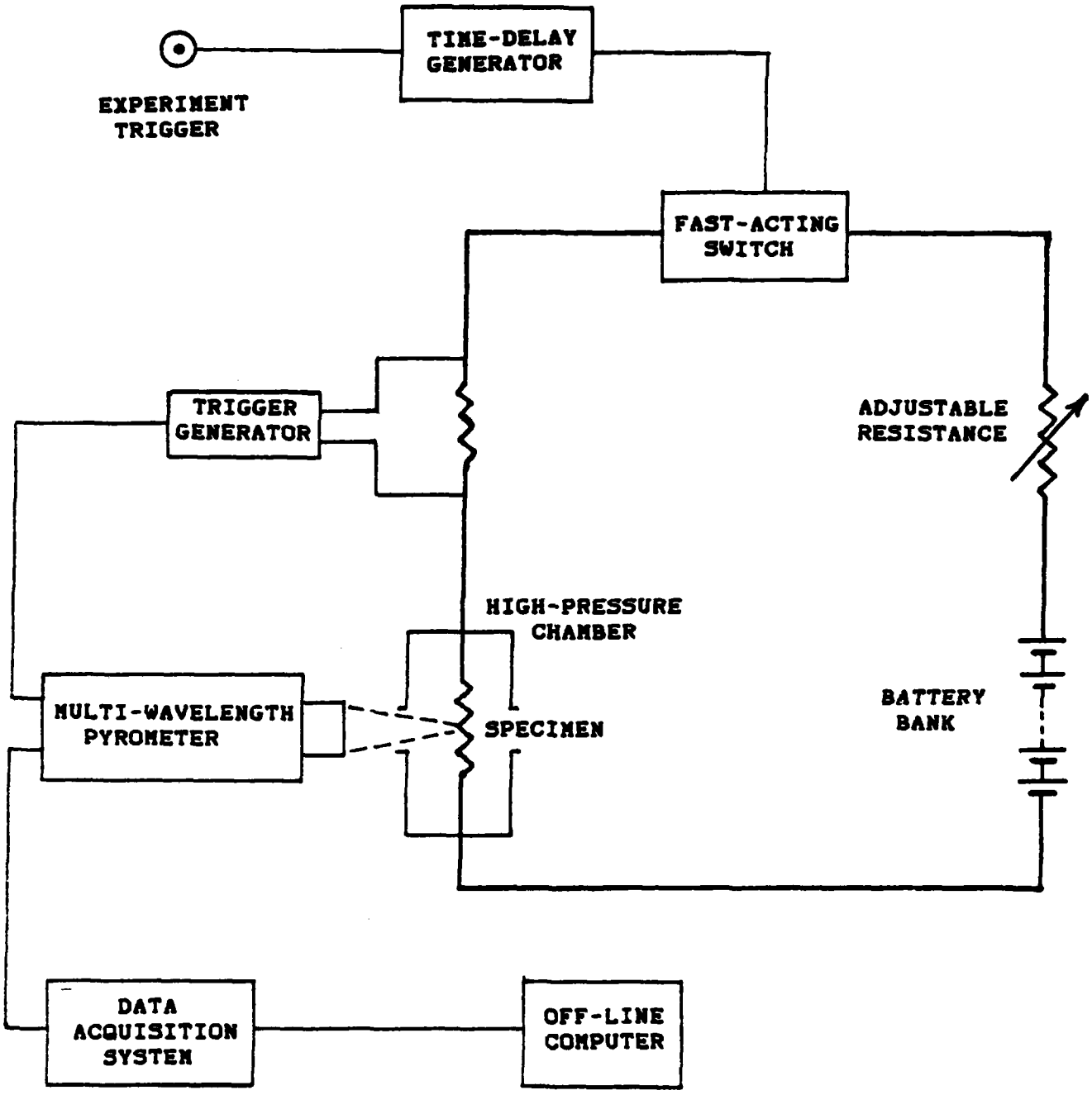

Fig. 1. A functional diagram of the high-speed measurement system.

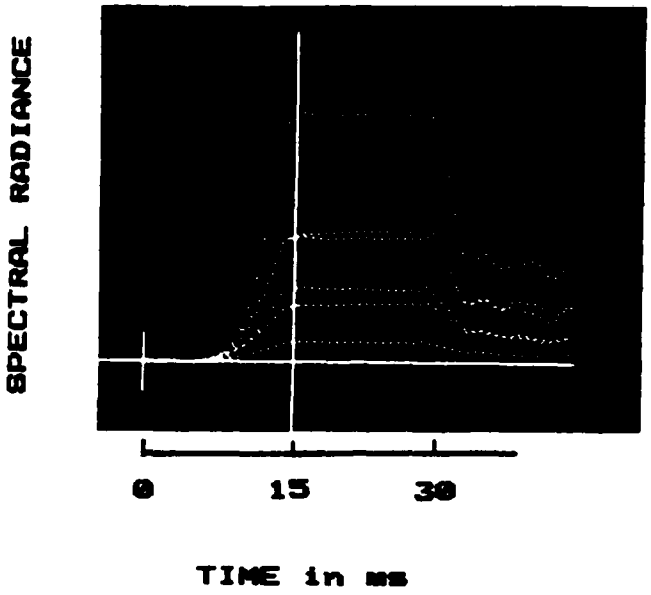

Fig. 2. Oscilloscope trace photograph showing the variation with time of the spectral radiance from the specimen surface, as seen by six channels of the multi-wavelength pyrometer, during a typical experiment in which the specimen was pulse heated to its melting point in a pressurized gas environment (80% argon, 20% oxygen) at 14 MPa and at a heating rate of $3 \times 10^5 K \cdot s^{-1}$.

Fig. 3. A photograph of the lower portion of the specimen after it was pulse heated in a 80% argon/ 20% oxygen environment. The glassy appearance exhibited by the surface of the remaining portion of effective specimen indicates that melting has occurred.

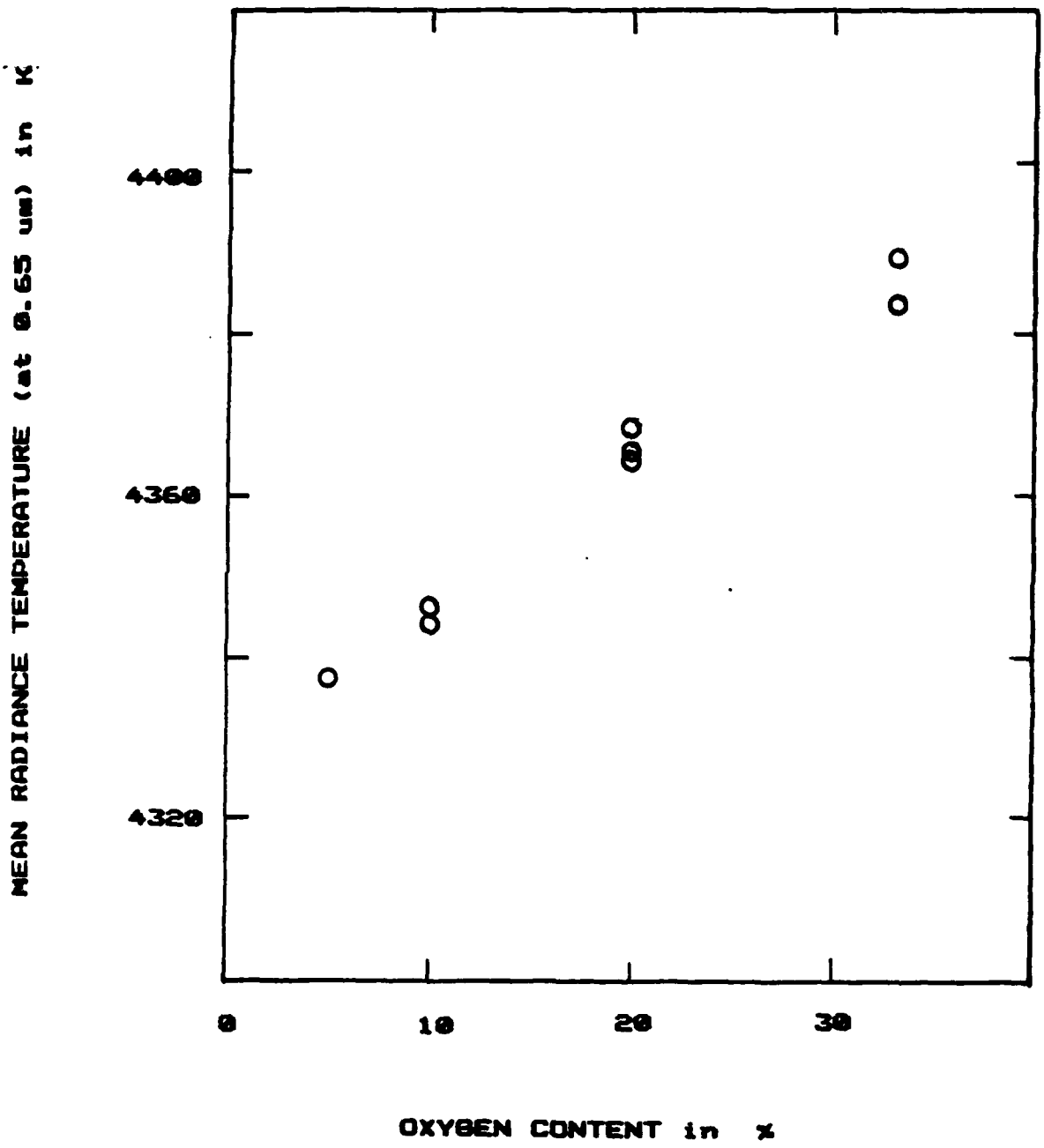

Fig. 4. Variation of the mean radiance temperature at 0.65 um of graphite during melting as a function of oxygen content in the pressurizing argon gas environment.

HIGH TEMPERATURE ENTHALPY MEASUREMENTS
David A. Ditmars, Principal Investigator

I. Thermodynamic Properties of Environmentally Resistant Ceramics and Refractories

Introduction

Heat-capacity calorimetry is one of most cost-effective approaches (often, it is the only available approach) for obtaining accurate fundamental thermodynamic property data for materials which are candidates for applications involving high temperatures and corrosive, hostile operating environments. Such data may have direct engineering applications in optimizing heat transfer, guarding against thermal shock, and in evaluating the accuracy of some thermophysical property data measured by independent transient methods. It is also used in the calculation of high-temperature chemical equilibria and in the generation and analysis of ceramic and alloy phase diagrams.

The NBS high-temperature calorimetry facility, maintains an isothermal drop calorimeter for the temperature range 273-1200 K and an adiabatic receiving calorimeter for the temperature range 1200-2600 K. The temperature range of the latter instrument overlaps that of the NBS millisecond pulse calorimeter and provides a valuable check on the transient measurement approach of the pulse technique. Substances investigated may be liquid or solid and include both electrical conductors and non-conductors. NBS has employed this facility to investigate refractory and other materials of interest to the Air Force. Attempts are made to identify materials for which currently available thermodynamic data are incomplete or unreliable due to poor characterization of the samples or inaccuracies in measurement technique.

Nitrides, borides, and carbides form three very important classes of refractory materials finding application in high-temperature design and as components of composite materials. Silicon nitride and boron nitride, for instance, are two important refractory construction materials for which the thermodynamic data is of questionable reliability. Heat measurements on these materials are sparse and their interpretation is complicated by the simultaneous occurrence of two crystalline forms of each of these substances.

Measurements

The enthalpy of silicon nitride (α,β) relative to 273 K and that of boron nitride (hex, cubic) relative to 273 K have both been measured to 1200 K. The two crystalline forms of Si_3N_4 are based on a hexagonal unit cell and differ principally in having a slightly different arrangement of the nitrogen tetrahedra enclosing each Si atom. The β-phase is thought to be metastable at room temperature. No low temperature (below 273 K) heat capacity data on Si_3N_4 have appeared in the literature. Only two high temperature heat capacity studies for Si_3N_4 have been reported [1,2] and these differ by as much as 30% below 1300 K. No structural characterization of the material investigated in [1,2] was given. The present samples of αSi_3N_4 and βSi_3N_4 were submitted for both structural and chemical analysis. They showed 98^+ percent chemical purity and $\geq$ 95 percent phase purity. The heat-capacity data derived from the experiments are presented below:

$\underline{\alpha Si_3N_4}$:

$$C_p = (-0.3262989)\times10^{-4}t^2 + (0.6552924)\times10^{-1}t + (0.1384411)\times10^3 + (-0.1558073)\times10^5 \times (273.15/T^2) \quad (1)$$

$\underline{\beta Si_3N_4}$:

$$C_p = (-0.5183574)\times10^{-4}t^2 + (0.9274656)10^{-1}t + (0.1295339)\times10^3 + (-0.1324359)\times10^5 \times (273.15/T^2) \quad (2)$$

where,

C_p = heat capacity/$J \cdot K^{-1} \cdot mol^{-1}$

t = Celsius temperature

T = Kelvin temperature = t + 273.15

The two crystalline forms of boron nitride are a hexagonal ("graphitic") phase and a cubic ("tetragonal", or "diamond-like") phase. The stable phase at atmospheric pressure and temperatures above 500 K is the hexagonal phase. The situation with BN is analogous to that which exists with carbon (graphite/diamond). Cubic BN is produced by shock compression at high temperatures and pressures and, like diamond, is stable at a temperature of a few hundred Kelvin and below. The high-temperature limit of stability of cubic BN is uncertain but it appears likely to revert to the hex form below 1700 K. Fortunately, there exist single low-temperature (4-300 K) studies for both forms of BN [3,4].

The chemical purity of both BN samples was better than 99^+ (mass) percent. The heat capacity data derived from the experiment are given below.

<u>Hexagonal BN</u>:

$$C_p = (-0.2385988)\times10^{-4}t^2 + (0.4458208)\times10^{-1}t + (0.2511515)\times10^2 + (-0.2267366)\times10^4\times(273.15/T^2) \quad (3)$$

<u>Cubic BN</u>:

$$C_p = (-0.2509428)\times10^{-4}t^2 + (0.4557994)\times10^{-1}t + (0.2637653)\times10^2 + (-0.4000692)\times10^4\times(273.15/T^2) \quad (4)$$

where,

C_p = heat capacity/$J \cdot mol^{-1} \cdot K^{-1}$

t = Celsius temperature

T = Kelvin temperature = t + 273.15

The high-and low-temperature (below room temperature) heat capacity data are in good agreement.

Bibliography

[1] Touloukian, Y.S. and Buyco, E.H., Specific Heat: Non-Metallic Solids, in Thermophysical Properties of Matter, The TPRC Data Series, Touloukian, Y.S., and Ho, C.Y. (Eds.), IFI, Plenum, New York (1970).

[2] JANAF Thermochemical Tables 2nd edition, NSRDS-NBS 37, June 1971, for sale by Superintendent of Documents, Washington, DC.

[3] Westrum, E.F., Jr., priv. comm. (1960).

[4] Kiseleva, I.A., Mel'chakova, L.V., and Topor, N.D., Izvest. Akad. Nauk SSSR, Neorg. Mat. 9 (3), 494-495 (1973).

II. Heat Capacity of bcc Calcium; Enthalpy of fcc/bcc Transition

Introduction

The existence of an unusual rise (up to 50% or more) in the high-temperature heat capacity of several bcc refractory metals has resisted theoretical interpretation to data [1]. Attempts have been made by theoreticians to define more adequate models (choice of interatomic potential, radius of neighbor-neighbor interactions, etc.) and these have been tested on simple fcc metals for which there exists substantial experimental thermodynamic data base [2]. In the case of aluminum, the comparison [3] of theoretical results for $C_v(s)$ to the values for $C_v(s)$, derived from the literature, cast doubt upon the accuracy of the literature data. New, definitive measurements of $C_p(s)$ in the range 273 K - 929 K [4] indicated the literature data to be in error and yielded a highly satisfactory confirmation of the theoretical model [5]. In order to extend the fcc model to bcc metals, it is desirable to obtain accurate heat-capacity data on a metal exhibiting both fcc and bcc phases at high temperatures, without complicating magnetic transitions. Such behavior is found in the alkaline earths calcium and strontium. The thermodynamic functions for these highly-reactive metals are sparse and inaccurate due to experimental difficulties in achieving and maintaining adequately low sample-impurity levels.. We report new data on a pure calcium sample.

Samples

Triply-distilled calcium metal was obtained from Rare Earths Products, Ltd., Widnes, Cheshire, U.K. This sample ("REP") was analyzed by several techniques for the major impurities. It was then re-processed by a modified

distillation method at the Materials Preparation Center of the State University of Iowa. The re-processed sample is referred to as "REP/AMES". Table 1 presents the measured impurity levels or the two samples. A specimen of sample REP/AMES of mass 2.19665 g was encapsulated in a tantalum container in an argon atmosphere. The tantlalum container was sealed in a Pt/10Rh container in an inert atmosphere.

Table 1
Calcium Impurity Levels

	REP	REP/AMES		
	At %	Mole %	At %	Mole %
O	2.606		2.238	
H	0.737		0.477	
C	0.047		-	
N	0.021		-	
Ba	0.012		-	
CaO		2.676		0.239
CaH_2		2.676		0.240
Ca		96.953		99.521

Methods

The enthalpy, relative to 273.15 K, of the sample plus encapsulation was measured in a precise, isothermal, phase-change calorimeter over the temperature range 673 - 1112 K using previously documented methods [6,7]. Multiple measurements were made at several temperatures distributed equally throughout the temperature range as a check on the precision of measurement.

In addition, an earlier series of enthalpy measurements on an empty Pt/10Rh capsule nearly identical to the one used to encapsulate the calcium specimen was available [8]. The specimen enthalpy data were obtained by subtracting at each temperature, the measured specimen plus encapsulation enthalpy, from that of the encapsulation alone. The contribution of the tantalum to the gross measured heat was calculated using the tantalum enthalpy data of the JANAF tables [9]. Corrections were made to the gross measured sample heats for the small mass difference between the specimen and empty capsules and for the heat due to the major assumed impurities, CaO and CaH_2 (cf Table 1). In addition, a second calcium specimen was independently encapsulated in a tantalum vessel and the solid-solid transition temperature measured by thermal analysis.

The enthalpy data for the fcc phase were fitted with a linear model:

$$(H_T - H_{273.15}) = AT + B \qquad J \cdot mol^{-1} \tag{1}$$

where,

H = enthalpy

T = Kelvin temperature

The coefficients and the standard deviation (σ_f) of this fit are:

A = +28.0788

B = -7742.94

σ_f = 35.52

The enthalpy data for the bcc phase were fitted with a quadratic model:

$$(H_T - H_{273.15}) = CT^2 + DT + E \qquad J \cdot mol^{-1} \tag{2}$$

The coefficients and the standard deviation (σ_b) of this fit are:

C = +0.876302E-02

D = +0.154862E+02

E = -0.219619E+04

$\sigma_b = 15.00$

Extrapolation of these enthalpy functions to 715 K yields 238±4 $J \cdot mol^{-1}$ for the enthalpy of the fcc-bcc phase transition.

Results

An fcc-bcc transition temperature of 715 K was measured. The corrected net enthalpy data for the specimen are given in Table 2.

Table 2. Enthalpy Data for Ca(s) [1]

T/K	$(H_T - H_{273.15})$ / J mol^{-1}	
	fcc	bcc
683.244	11484.99	
683.038	11472.51	
673.019	11129.12	
672.961	11125.08	
703.030	11997.28	
702.900	11997.28	
702.900	11978.14	
773.292		15003.70
773.244		15018.01
822.55		16485.00
873.03		18019.52
872.89		17992.36
923.71		19590.94
974.37		21238.16
974.28		21174.28
1023.86		22848.29
1073.89		24498.26
1104.44		25630.67

[1] M.W. = 40.08

In Table 3, the present results have been compared to selected values obtained from the most widely used compilations of thermodynamic properties [9,10,11].

Table 3. Summary of Selected Thermodynamic Data for Calcium

	Ref. [10]	Ref. [11]	Ref. [9]	Present Work
$T_{fcc/bcc}$	720± 3	716	721± 2	715±10 /K
$\Delta H_{fcc/bcc}$	220±50	222	220±50	238± 4 /J·mol^{-1}
$\Delta C_{Pfcc/bcc}$	-9.4	-3.8	+5.3	-4.3 / %
$C_p(Tm)$	45.52	43.20	41.21	34.98 /J·mol^{-1}K^{-1}

Bibliography

[1] R.A. MacDonald and R.C. Shukla, Phys. Rev. B32 (in press) (1985).

[2] R.A. MacDonald and W.M. MacDonald, Phys. Rev. B24 (4), 1715 (1981).

[3] R.C. Shukla and C.A. Plint, Int. J. Thermophysics 1, 299 (1980).

[4] D.A. Ditmars, C.A. Plint and R.C. Shukla, Int. J. Thermophysics (in press) (1986).

[5] R.C. Shukla, C.A. Plint and D.A. Ditmars, Int. J. Thermophysics (in press) (1986).

[6] T.B. Douglas and E.G. King, Chap. 8 in Experimental Thermodynamics. Vol.I, Calorimetry of non-Reacting Systems, pp. 293-318, J.P. McCullough and D.W. Scott, Eds., (Butterworths, London, 1968).

[7] D.A. Ditmars, A. Cezairliyan, S. Ishihara and T.B. Douglas, NBS Special Publication 260-55 (1977).

[8] D.A. Ditmars and T.B. Douglas, J. Res. Nat. Bur. Stand. (U.S.) 75A (Phys. and Chem.) 5, 401-420 (1971).

[9] JANAF Thermochemical Tables 2nd edition, NSRDS-NBS 37, June 1971, for sale by Superintendent of Documents, Washington, DC.

[10] R. Hultgren, P.D. Desai, D.T. Hawkins, M. Gleiser, K.K. Kelley, and D.D. Wagman, Selected Values of the Thermodynamic Properties of the Elements, American Society for Metals, Metals Park, OH (1973).

[11] V.P. Glushko, L.V. Gurvich, et.al., Thermodynamic Properties of Individual Substances, Vol.III (1,2), Nauk Press, Moscow (1981). (In Russian).

Broad-Band Spectroscopy of Small Molecules in Intense Laser Fields

Principal Investigators: P. S. Julienne and F. H. Mies

Introduction

The general goal of this research is to provide calculations of radiative cross-sections, fragment state distributions, and intense laser saturation effects for broad-band, wavelength insensitive continuum spectral features of small gaseous molecules of possible interest in spacecraft survivability.

Theoretical input into this program is provided by extensive sets of computer codes available to the quantum chemistry group. State of the art calculations of necessary molecular potentials, couplings and radiative transition dipoles are assessible. Scattering codes provide cross-sections and branching ratios of photodissociation fragments. Programs for evaluation of adiabatic Franck-Condon matrix elements and non-adiabatic radiative scattering matrix elements allow for evaluation of attenuation coefficients for laser radiation propagating through gaseous vapors

In addition to numerical procedures, the program requires extensive analysis of many new theoretical features introduced by very intense laser fields.

Progress During FY 85

(1) A new CDC Cyber 205 central computer facility has been installed at NBS and a good deal of our effect has been devoted to recompiling our codes on this vastly improved, sixth generation computer. In addition to transferring existing programs, we are exploiting the unique capabilities of the 205, especially with regard to vectorizing the scattering codes. This upgrading of our programs has profoundly expanded our capabilites to treat the photodissociation of polyatomic systems with many coupled channels.

(2) Codes have been modified, and preliminary calculations have been performed to study the pressure broadening of atomic and molecular lineshapes in extremely strong laser fields. Although this represents the spectroscopic equivalent of a continuum-continuum transition, the half-collision aspects of the calculations are completely transferable to forthcoming calculations of bound-continuum photodissociation cross-sections. Manifestions of a.c. stark shifts and the laser-induced Mollow lineshape associated with the dressing of fragments by the radiation field are extracted from the numerical results. This suggests that normal perturbation theory as applied to radiative interactions must be carefully scrutinized when applied to laser attenuation mechanisms.

(3) The testing of various algorithms for calculation of photodissociation cross-sections introduced into the multichannel close-coupling codes is nearly complete. We are settling on a numerical procedure devised by Singer etal[1] which allows for proper description of both the total cross-sections and the branching into fragment states. This gives very stable procedures for evaluating bound-continuum transitions, including all possible subtleties associated with non-adiabatic effects in molecular dissociation. Most of the important features of non-linear response to intense laser fields can be simulated by these codes, although some well understood modifications might have to be introduced in future studies depending on the radiation parameters employed in spacecraft studies.

(4) We have applied our analytic treatment of molecular continuum states to the analysis of molecular photodissociation. This is based on a generalized version of quantum defect theory as applied to predissociation of energetically excited molecules. Given close coupled scattering

wavefunctions obtained form numerical solutions we can extract analytic parameters which can greatly enhance our ability to calculate photodissociation cross-sections over wide ranges of laser frequencies.

(5) During the course of our study of strong field effects on pressure-broadened lineshapes, we have developed a convergent analysis of radiative matrix elements which has many applications throughout lineshape theory.

(6) To complement our exact, fully non-adiabatic evaluation of photodissociation cross-sections for diatomic molecules, we are currently using Franck-Condon matrix elements for bound-continuum transitions, and theory previously developed for excimer transitions[2,3] to obtain estimates of total cross-sections. Although these simple calculations should give us reasonable estimates of laser attenuation coefficients for diatomic molecules, quantitative application to larger molecules remains to be tested.

Papers Completed in FY85

Two papers supported by this research proposal have been submitted for publication. Preprints are attached to this report.

(1) "Analytic Multichannel Theory of Molecular Dissociation", P.S. Julienne and F.H. Mies, to appear in Electronic and Atomic Collisions (Lorents, Meyerhof and Petersen, Eds., North-Holland, Amsterdam 1986).

(2) "A Convergent Analysis of Radiative Matrix Elements in Atomic Lineshape Theory", F.H. Mies, P.S. Julienne, Y.B. Band and S.J. Singer, submitted to J. Physics B. (1985).

Papers Presented in FY85

Two talks acknowledging support by AFOSR were presented.

(1) An invited paper was presented by P.S. Julienne at the 14th Conference on the Physics of Electronic and Atomic Collisions, Palo Alto, CA July 1985. Subject: Analytic Theory of Molecular Dissociation.

(2) A contributed paper was presented by F.H. Mies at the 1985 Conference on the Dynamics of Molecular Collisions, Snowbird, Utah July 1985. Subject: Collisional Redistribution of Resonant Radiation in Intense Fields.

REFERENCES:

1. S.J. Singer, K. Freed and Y.B. Band, J. Chem. Phys. 81, 3091 (1984).
2. F.H. Mies, Molec. Phys. 26, 1233 (1973).
3. M. Krauss and F.H. Mies, in "Excimer Lasers", Ed. C.K. Rhodes, Springer Topics in Applied Phys., Vol. 30, (2nd Ed., Berlin 1984) pp.5.

ANALYTIC MULTICHANNEL THEORY OF MOLECULAR DISSOCIATION

Paul S. Julienne and Frederick H. Mies

Molecular Spectroscopy Division, National Bureau of Standards, Gaithersburg, MD 20899*

A generalized multichannel quantum defect analysis of the close coupled molecular wavefunction for arbitrary potentials gives a unified description of the bound and scattering states of the diatomic molecule AB by defining a real symmetric matrix $Y(E)$ which can be analytically continued across a dissociation threshold. The theory also leads to a half collision analysis of weak predissociation and photodissociation whereby the transition amplitude matrix is separated into factors representing short range Franck-Condon transitions and long range final state interactions. For sufficiently high fragment separation velocity, the effects of final state interactions on product distributions are well approximated by small departures from the recoil limit as prescribed by pure frame transformations among Hund's coupled electronic-rotational states.

1. INTRODUCTION

The process with which we are concerned here is that of molecular dissociation, that is, the formation of an unstable state of the molecule AB which separates to fragments A and B. There are a variety of ways by which a dissociative continuum state can be excited: through initial preparation of a bound metastable state which predissociates, through direct photoexcitation, or perhaps through some collisional excitation process. Generally the items of interest for measurement or calculation are the total rate at which the process occurs and the branching ratios which describe the distribution of particular final states.

The dissociative states of the species AB are also the collisional or scattering states of the fragments A + B. Therefore there has been a considerable amount of interest and success recently in generalizing close coupling scattering algorithms for the numerical calculation of photodissociation transition amplitudes (1-7). The theory (8-13) which we will summarize here is complementary to these numerical approaches. It is based on an analysis of the structure of the close coupled, or multichannel, time independent scattering wavefunction. It will hopefully lead to useful insights concerning molecular dissociation and also lend itself to the development of quantum and semiclassical approximations. Although our development has concentrated on application to neutral atom scattering, that is, diatomic dissociation, many of the features of the theory are general and need not be restricted to this case.

We call our approach a generalized multichannel quantum defect analysis (MCQDA) (10), since it is strongly motivated by the concepts of standard multichannel quantum defect theory (MQDT) (14,15). The latter is designed to treat problems associated with bound Rydberg states, autoionizing resonances, and electron-ion scattering. It has not only been successfully applied to many

*This work was sponsored in part by the Air Force Office of Scientific Research.

atomic problems, but has also been extended to treat molecular bound and dissociative states in the vicinity of an ionization threshold (16,17). This standard MQDT makes heavy use of the properties of the Coulomb potential and its solutions. The generalized MCQDA has been developed by us (10,11) and others (17-19) to apply to systems described by arbitrary potentials, for example, the Born-Oppenheimer potentials for the interaction of A and B.

There are two features of the theory which we will emphasize in this paper. First, the theory enables us to define a real, symmetric matrix $\mathbf{Y}(E)$ that can be analytically continued across thresholds and thereby relate the properties of open channel scattering states above threshold and predissociating closed channel resonances below threshold (10,11). Second, we will explicitly consider the case of weak coupling between an initial state and a manifold of final states, and show how a half-collision factorization of transition amplitudes for predissociation and photodissociation can be developed (12). This analysis will be illustrated by interpreting photodissociation and radiative redistribution experiments in which an aligned ^1P atom is produced following molecular absorption of a polarized photon.

2. MCQDA FORMULATION

In general the wavefunction which describes the diatomic species AB at total energy E can be expanded as

$$\psi_{\alpha'}(E) = \sum_{\alpha} |\alpha\rangle F_{\alpha\alpha'}(E,R)/R \tag{1}$$

where the basis functions $|\alpha\rangle$ span all coordinates except the AB interfragment separation R. This may also be written in the following matrix notation, where $|\alpha\rangle$ is a row vector:

$$\boldsymbol{\psi} = |\boldsymbol{\alpha}\rangle\, \mathbf{F}(E,R)/R \tag{2}$$

Introduction of eq. 1 into the Schrodinger equation, $H\psi = E\psi$, generates the standard matrix Schrodinger equation, or equivalently, the set of close coupled equations,

$$\frac{d^2}{dR^2}\mathbf{F} + \frac{2\mu}{\hbar^2}[E\cdot\mathbf{1}^\circ - \mathbf{W}(R)]\,\mathbf{F} = \mathbf{0} \quad , \tag{3}$$

where $\mathbf{1}^\circ$ is the unit matrix [In this paper diagonal matrices are always indicated by a superscript zero]. The symmetric normally nondiagonal matrix $\mathbf{W}$, which describes the potentials and couplings among the various states α, is found by taking matrix elements of the total Hamiltonian over the basis function $|\alpha\rangle$.

Although it is possible to set up and solve such equations using a variety of choices of basis $|\alpha\rangle$, the scattering boundary conditions in the limit of large R must be applied using a particular basis set, namely, the channel state basis $|\gamma\rangle$. These basis states are eigenstates of total angular momentum, $\vec{J} = \vec{j} + \vec{\ell}$, where $\vec{j} = \vec{j}_A + \vec{j}_B$ is total fragment angular momentum and $\vec{\ell}$ is the relative angular momentum of A and B. For the case of atom-atom scattering this basis corresponds to Hund's case (e) of diatomic angular momentum coupling. The potential matrix $\mathbf{W}^\infty$ in the channel state representation is asymptotically diagonal, having elements

$$W^\infty_{\gamma\gamma}(R\to\infty) \sim E^\infty_\gamma + \frac{\hbar^2 \ell_\gamma(\ell_\gamma+1)}{2\mu R^2} \tag{4}$$

The channel energy E_γ^∞ is the total asymptotic fragment energy, not including kinetic energy.

The expansion basis must always be truncated with only a finite number of states, hopefully chosen to represent the physics adequately. The total number of channels N_T is divided into N_O open and N_C closed channels, depending on total energy. The channel wave vector

$$k_\gamma = [2\mu(E-E_\gamma^\infty)/\hbar^2]^{1/2} \tag{5}$$

is real for open channels, for which the fragments can separate asymptotically with kinetic energy $E-E_\gamma^\infty$. But k_γ is pure imaginary for closed channels, i.e., $E < E_\gamma^\infty$, so that the fragments can not separate in channel γ. If $E < E_\gamma^\infty$ for all γ, $N_T = N_C$ and the only possible states of AB are bound states. If $E > E_\gamma^\infty$ for all γ, $N_T = N_O$ and inelastic collisions can couple any two channels. If E is such that some channels are open, some closed, then it is possible to have metastable bound states, or resonances, which can decay by predissociation.

The MCQDA gives a unified way to describe open and closed channel properties and gives new insights into the decay of predissociating resonances. The basic idea of the analysis is to introduce a set of diagonal reference potentials $\mathbf{W}^\circ$ such that

$$\mathbf{W}(R) = \mathbf{W}^\circ(R) + \mathbf{V}(R) \ , \tag{6}$$

and $\mathbf{V}(R)$ vanishes asymptotically. Each reference potential $W_{\alpha\alpha}(R)$ gives rise to two linearly independent solutions of the Schrodinger equation, f_α and g_α. In matrix form the diagonal matrices $\mathbf{f}^\circ$ and $\mathbf{g}^\circ$ are each solutions of the diagonal (or uncoupled) set of equations

$$\frac{d^2}{dR^2}\mathbf{F}^\circ + \frac{2\mu}{\hbar^2}(E\cdot\mathbf{1}^\circ-\mathbf{W}^\circ)\,\mathbf{F}^\circ = 0 \ . \tag{7}$$

The general solution to the coupled equations 3 can be written as a linear combination of these reference solutions, with R-dependent coefficients A and B,

$$\mathbf{F}(E,R) = \hat{\mathbf{f}}^\circ(E,R)\,\mathbf{A}(E,R) + \hat{\mathbf{g}}^\circ(E,R)\,\mathbf{B}(E,R) \ . \tag{8}$$

If $\hat{\mathbf{f}}^\circ$ and $\hat{\mathbf{g}}^\circ$ are carefully chosen to be analytic in E, then the $N_T x N_T$ dimensional matrix defined by the asymptotic quantity

$$\mathbf{Y}(E) = \mathbf{B}(E,\infty)\,\mathbf{A}(E,\infty)^{-1} \tag{9}$$

can be analytically continued across dissociation thresholds (i.e., like a "quantum defect") and quantitatively relates the scattering and bound state properties of $\psi(E,R)$. In addition, the complex matrix

$$\mathbf{t}^{\pm}(E) = [\mathbf{A}(E,\infty) \pm i\mathbf{B}(E,\infty)]^{-1} \tag{10}$$

may be used to define "half collision" amplitudes which describe final state distributions in photodissociation and weak predissociation processes. Note that no approximations are involved in writing eq. 8. In fact, the original second order differential equations 3 can be rewritten as two coupled first order differential equations for $\mathbf{A}$ and $\mathbf{B}$, or equivalently, for R-dependent analogs of $\mathbf{Y}$ and $\mathbf{t}^-$ (9-12). Thus our analysis is related to amplitude density and phase amplitude methods in scattering theory (20,21). Our contribution is to emphasize the intrinsic analytic properties of the wavefunction that can be projected from such an analysis.

Although the MCQDA is a nonperturbative analysis, its usefulness will often depend on making a judicious choice of reference potentials $\mathbf{W}^\circ$. The reference basis $|\alpha\rangle$ is derived from the channel state basis $|\gamma\rangle$ by an orthorgonal transformation

$$|\alpha\rangle = |\gamma\rangle\, \bar{\mathbf{m}}(R) \tag{11}$$

$$\mathbf{W} = \mathbf{W}^\circ + \mathbf{V} = \bar{\mathbf{m}}\, \mathbf{W}^\circ\, \mathbf{m} \tag{12}$$

Normally the transformation $\mathbf{m}$ will be chosen for physical reasons to suggest reference potentials $\mathbf{W}^\circ$ which isolate particular effects by making $\mathbf{V}$ small or vanishing at some value of R. For example, if we want to be able to generate an energy insensitive $\mathbf{Y}(E)$ for extrapolating across thresholds, we would seek a transformation that gives a coupling $\mathbf{V}(R)$ that operates only in a short range zone of R, typically in the R_e region of Born-Oppenheimer potentials. On the other hand, for describing a photodissociation process, we would want to choose a $\mathbf{V}$ which is negligible in the zone of R near R_e which determines the Franck-Condon absorption, whereas there may be strong inelastic couplings due to $\mathbf{V}$ in an intermediate range of R that determine the distribution of atomic fragment states. Depending on the specific application, some choices of suitable reference functions for diatomic processes could be: a pure Hund's coupling case, such as the standard case (a) states; a set of intermediate coupled states; an adiabatic-electronic-rotational (AER) basis, which continuously diagonalizes the electronic-rotational Hamiltonain as a function of R and smoothly transforming from one Hund's case to another (8b,9).

Several types of reference solutions may be defined, depending on boundary conditions chosen (10,18). The solutions useful for extrapolating across thresholds are the functions $\hat{f}$ and $\hat{g}$, respectively regular and irregular as $R \to 0$. They are defined quantum mechanically but have the following semiclassical interpretation in a classical region of phase space:

$$\hat{f}_\alpha = \sin \beta_\alpha(R)/k_\alpha^{1/2}(R) \quad \text{and} \quad \hat{g}_\alpha = \cos \beta_\alpha(R)/k_\alpha^{1/2}(R) \quad , \tag{13}$$

where $\beta_\alpha(R)$ is the WKB phase angle (a is the classical turning point)

$$\beta_\alpha(R) = \int_a^R k_\alpha(R)\, dR - \frac{\pi}{4} \quad . \tag{14}$$

Each reference potential $W_{\alpha\alpha}(R)$ uniquely defines two energy-dependent phase angles $\xi_\alpha(E)$ and $\nu_\alpha(E)$. Above a channel threshold the open channel solutions define the reference phase shifts (we ignore subtle threshold effects discussed in detail in references 10 and 11)

$$\hat{f}_\alpha\ (R\to\infty) \sim k_\alpha^{-1/2} \sin(k_\alpha R - \frac{\pi}{2}\, \ell_\alpha + \xi_\alpha) \quad . \tag{15}$$

Below a channel threshold the regular solutions $\hat{f}_\alpha(E_\alpha R)$ are asymptotically divergent except at closed channel eigenvalues $E = E_n^\alpha$ defined by the modular π values of $\nu_\alpha(E)$

$$\tan \nu_\alpha(E) = 0 \quad \text{or} \quad \nu_\alpha(E_n^\alpha) = n\pi \quad . \tag{16}$$

The semiclassical approximation to ν

$$\nu_\alpha + \frac{\pi}{2} = \int_a^b k_\alpha(R)\, dR \tag{17}$$

gives the standard Bohr-Sommerfeld quantization rules.

The MCDWA analysis of Mies (10) shows how to define the symmetric real matrix $\mathbf{Y}(E)$ in eq. 9. If all channels are open, the $N_T x N_T$ scattering matrix S is simply related to Y as follows

$$S = e^{i\xi^\circ} (1^\circ + iY) (1^\circ - iY)^{-1} e^{i\xi^\circ} . \tag{18}$$

If we calculate S and the reference phase shift diagonal matrix ξ° above threshold, then we can calculate the $N_T x N_T$ Y matrix. If Y is sufficiently energy insensitive, then it may be extrapolated below thresholds to predict the resonance scattering and closed channel properties. For example, if we take the case $N_T=2$ with channel 1 closed and channel 0 open, then the elastic scattering phase shift of the open channel is modified due to predissociation originating from the bound states located at $\nu_1(E) = n\pi$ (11),

$$\eta_0(E) = \xi_0(E) + \tan^{-1} [Y_{00} - \frac{Y_{01}\, Y_{10}}{\tan \nu_1(E) - Y_{11}}] \tag{19}$$

If both channels are closed, the bound state eigenvalues are given by the expression

$$(\tan \gamma_0(E_n) + Y_{00}) (\tan \gamma_1(E_n) + Y_{11}) = Y_{01}^2 . \tag{20}$$

Eqs. 19 and 20 are valid for arbitrarily strong coupling and are only limited by our ability to obtain the reference phases and the matrix $\mathbf{Y}(E)$ = constant.

In the limit of weak coupling when $\mathbf{Y} \to \mathbf{0}$, eq. (19) transforms into the usual Lorentzian expression for an isolated resonance. The weak coupling width Γ_n and shift ΔE_n of the predissociating level at $E = E_n$ are

$$\Gamma_n^1 = \frac{2\Delta G_n}{\pi} Y_{01}^2 \quad \text{and} \quad \Delta E_n^1 = - \frac{\Delta G_n}{\pi} Y_{11} \quad , \tag{21}$$

where we have introduced the approximation

$$\left(\frac{\partial \nu_1}{\partial E}\right)_{E=E_n^1} = \frac{\pi}{\Delta G_n} \tag{22}$$

where ΔG_n is the vibrational spacing.

We have carried out a number of test calculations on 2 state models, i.e., 2 open or 1 open and 1 closed channels, and have demonstrated the success of the analysis over a wide range of conditions (11). These include an analysis of Cd_2 $^3\Sigma_u^+$ state predissociation to $Cd(^3P_o) + Cd(^1S_o)$ using AER reference states, and an analysis of the O_2 $^3\Sigma_u^-$ predissociation using diabatic reference states. Model strong coupling cases based on the latter were used to demonstrate the nonperturbative nature of the analysis. The Y(E) matrix was found to be most energy insensitive for short range inner potential wall curve crossings or near crossings where two reference potentials remain nearly parallel over a range of R. Its greatest energy sensitivity will occur for sharp outer crossings due to the more rapid energy variation of Franck-Condon overlaps.

3. WEAK COUPLING HALF COLLISION ANALYSIS

Let us now consider a special case which covers a wide variety of actual phenomena and for which the MCQDA allows us to develop a number of useful insights or approximations. Assume that we have a manifold of N_I channels

which may be strongly coupled among themselves and a similar manifold of N_F final channels, but that the coupling between the initial and final manifolds, described by the $N_F x N_I$ V_{FI} submatrix, is very weak. For simplicity we will consider the case here where $N_I = 1$, i.e., there is only a single nondegenerate initial channel. If the initial channel is open, as well as the final channels, the free-free transition amplitudes are given by the $N_F x N_I$ subblock of the S matrix, described to first order in V_{FI} by the Born distorted wave approximation,

$$S_{FI}(E) = -2\pi i \langle \psi_F^-(E)|V|\psi_I^+(E)\rangle , \tag{23}$$

when $\psi^\pm$ are energy normalized wavefunctions calculated in the absence of the weak coupling and the ± refer to incoming and outgoing scattering boundary conditions. Similarly, if the initial channel is closed, the bound-free predissociation transition amplitudes for decay of the closed channel resonance at $E=E_n$ are

$$\tau_{FI}(E_n) = -2\pi i \langle \psi_F^-(E_n)|V|E_n\rangle \tag{24}$$

where $|E_n\rangle$ is the unit normalized bound state wavefunction.

There are numerous examples of weak predissociations in molecular spectroscopy. One special case is predissociation induced by a radiation field, namely, photodissociation. If the initial state basis functions are molecule-radiation-field states $|\alpha_I\rangle\ |nq\omega\rangle$, with n photon of frequency ω and polarization q, and the final states have n-1 photons $|\alpha_F\rangle|n-1,q,\omega\rangle$, then the free-free process, eq. 23, describes line broadening and radiative redistribution phenomena and the bound-free process, eq. 24, describes photodissociation (22). For the case of radiative coupling the weak coupling matrix is just (22,23).

$$V_{FI}(\text{rad}) = \left(\frac{2\pi\hbar\omega\phi}{c}\right)^{1/2} \langle\alpha_F|\hat{e}_q\cdot\vec{\mu}|\alpha_I\rangle \tag{25}$$

where ϕ is the field intensity (photons $cm^{-2}sec^{-1}$), $\hat{e}_q$ the polarization vector of the light, and $\vec{\mu}$ the molecular dipole operator.

When we impose scattering boundary conditions on the asymptotic wavefunction in the channel state basis $|\Upsilon\rangle$, we find (using eq. 11) that the energy normalized wavefunctions for the respective initial and final manifolds are

$$\boldsymbol{\psi}^\pm = |\boldsymbol{\alpha}\rangle\ \kappa(\hat{\mathbf{f}}^\circ\mathbf{A} + \hat{\mathbf{g}}^\circ\mathbf{B})\mathbf{N}^\pm \quad , \tag{26}$$

where $\kappa = (2\mu/\hbar^2\pi)^{1/2}$ and the normalization matrix $\mathbf{N}^\pm$ is

$$N^\pm = [\mathbf{t}^\mp(\infty)]^{-1}\ e^{\pm i\xi^\circ} \quad , \tag{27}$$

with $\mathbf{t}$ given by eq. 10. (12) We now wish to make one more assumption. Assume that the weak coupling V_{FI} which couples the two manifolds is only significant in some short range zone of R near R_o and that the final state interactions V_{FF} which determine the final state distribution are important in a longer range zone of R. Since $\mathbf{B}$ must vanish at the origin and does not become large until $R > R_o$, the weak transition occurs in a zone of R where to a good approximation we may take $\mathbf{A}=1$, $\mathbf{B}=0$. We immediately see from eqs. 23, 24, 26 that the weak coupling amplitudes are

$$S_{FI} = -2\pi i\ \tilde{N}_F^+(E)\ \hat{S}_{FI}(E)\ N_I^+(E) \tag{28a}$$

$$\tau_{FI}(E_n) = -2\pi i\ \tilde{N}_F^+(E_n)\ \hat{T}_{FI}(E_n) \tag{28b}$$

where

$$\hat{S}_{FI}(E) = \kappa^2 \langle \hat{f}_F^o(E) | V_{FI} | f_I^o(E) \rangle \tag{29a}$$

$$\hat{T}_{FI}(E_n) = \kappa \langle f_F^o(E_n) | V_{FI} | E_n \rangle \ . \tag{29b}$$

and we have used the result $N_F^+ = N_F^{-*}$.

The results, eq. 28, show how a very useful factorization of the weak coupling transition amplitudes can be achieved. The $\hat{S}$ and $\hat{T}$ amplitudes are real Franck-Condon amplitudes which describe the excitation process. The $\mathbf{N}_F$ matrix is a "half collision" dynamical matrix which incorporates the effect of final state interactions and provides the correlation between the short range reference states excited by $\mathbf{V}_{FI}$ and the asymptotic distribution of fragments which could be measured experimentally. The initial state matrix $\mathbf{N}_I$ is a simple phase factor for a single initial channel, whereas for a manifold of initial channels, it would describe the formation of the reference states from the asymptotic states. We see that the physical picture implicit in the factorization, eq. 28b, is the time-independent analog of the time-dependent wavepacket viewpoint of photodissociation of Lee and Heller (24). According to this viewpoint, photodissociation is described as the initial creation of an excited state wavepacket through a "Franck-Condon" excitation from the initial bound state due to weak radiative coupling. The time evolution of this wavepacket leads to the distribution of final states.

We have shown two important properties of the $\mathbf{N}^+$ matrix (12). First, as long as no nonclassical regions are encountered by the fragments between the excition region, $R = R_o$, and the detection region, $R = \infty$, then $\mathbf{N}^+$ is unitary to a very good approximation. Second, the $\mathbf{N}^+$ matrix can be further factored as

$$\mathbf{N}^+ = \mathbf{O}^+ \mathbf{U}^+ \tag{30}$$

The factor $\mathbf{U}^+$, the so-called frame transformation matrix, depends only on the reference solutions and the orthogonal basis transformation matrix $\mathbf{m}$. If an AER reference basis is used, it takes on the form

$$\mathbf{U}^+ = L(R_s)\, e^{i\xi^o} \tag{31}$$

$$\text{with } L(R) = e^{i\beta^o}\, \mathbf{m}(R)\, e^{-i\beta^o} \tag{32}$$

where β^o is the matrix of WKB reference phases, eq. 14. The distance R_s is a characteristic switching distance at which the final state interactions begin to become important as the fragments separate. The matrix $\mathbf{O}^+$ in eq. 30 incorporates the effect of final state interactions in causing deviations from the pure frame transformation, eq. 31. It is possible to obtain a first order differential equation for $\mathbf{O}^+$ by which these deviations can be calculated (12).

A special limiting case which has been used to predict final state distributions in diatomic photodissociation is the recoil approximation, or more specifically, the J-independent recoil approximation (25). This amounts to ignoring any J dependence of final state Franck-Condon factors and phase development. This limit will always apply at sufficiently high fragment kinetic energy. In our formulation, this limit corresponds to setting $\mathbf{N}^+ = \mathbf{m}(R_o)$. If, however, we set $\mathbf{N}^+ = \mathbf{U}^+$, thereby ignoring the nonadiabatic corrections in $\mathbf{O}^+$ but incorporating the effect of adiabatic phase development, and continue to ignore any J-dependence in the Franck-Condon amplitudes, $\hat{S}$ or $\hat{T}$, we obtain an improved approximation which allows us to incorporate the effect of molecular axis rotation into orientation/alignment experiments. We thus see that the factorizations, eqs. 28 and 30, are very powerful tools which enable us to introduce a heirarchy of approximations for successively introducing various dynamical effects into the interpretation of photodissociation or predissociation product distributions.

In our earlier discussion we emphasized the $\mathbf{Y}$ matrix and its continuity across a dissociation threshold. For our present example of a single initial channel weakly coupled to a manifold of final channels, the $\mathbf{Y}_{FI}$ submatrix to first order in $\mathbf{V}_{FI}$ is

$$\mathbf{Y}_{FI}(E) = -\pi\, \mathbf{A}_F^{-1}(E,\infty)\, \hat{\mathbf{S}}_{FI}(E) \ . \tag{33}$$

The continuity of $\mathbf{Y}$ across the initial state threshold is thus reflected by the well known continuity of Franck-Condon amplitudes $\hat{\mathbf{S}}$. The connection between $\hat{\mathbf{S}}_{FI}$ and $\hat{\mathbf{T}}_{FI}$ in eq. 29 is readily seen when we write the unit normalized initial bound state function as

$$|E_n\rangle = (\Delta G_n)^{1/2}\, \kappa\, \hat{\mathbf{f}}_I(E_n) \tag{34}$$

where we have used eq. 22 and the results of references 8 and 10. Thus,

$$\hat{\mathbf{T}}_{FI}(E_n) = (\Delta G_n)^{1/2}\, \hat{\mathbf{S}}_{FI}\,(E_n) \tag{35}$$

shows the relation between the nonanalytic $\hat{\mathbf{T}}$ and the analytic $\hat{\mathbf{S}}$.

One important consequence of the unitarity of $\mathbf{N}^+$ is that the total predissociation decay rate, given by the following scalar dot product,

$$A_n = \tilde{\tau}_F^{\,*}\, \tau_F/h = (4\pi^2\, \tilde{\hat{\mathbf{S}}}_{FI}\, \hat{\mathbf{S}}_{FI})\, (\Delta G_n/h), \tag{36}$$

depends only on the excitation Franck-Condon factors $\hat{\mathbf{S}}$, and not on the half-collision dynamical matrix. This justifies the usual adiabatic approximation for continuum spectroscopy and weak predissociation, i.e., given our assumptions, it is only necessary to take into account the local interactions in the Franck-Condon region to calculate the total rate of decay. Since when the initial channel is open the first factor in parenthesis in eq. 36 is interpreted as the total inelastic transition probability from I to the F manifold, we see that the closed channel decay rate is simply interpreted as a single cycle transition probability times the oscillation frequency $\Delta G_n/h$. The continuity of $\hat{\mathbf{S}}$ across threshold and this interpretation of eq. 36 has recently been discussed by Tellinghuisen and Julienne (26) in relation to the inverse of the phenomena considered here, namely, for radiative association and bound state radiative decay.

We have carried out specific calculations for the case where polarized absorption from a $^1\Sigma^+$ state through either a $^1\Sigma$ or $^1\Pi$ molecular Born-Oppenheimer reference state leads to ^1P + ^1S fragment atoms (23,27). The ^1P atom may be aligned (q=0) or oriented (q=±1). This describes both Sr or Ba + rare gas radiative redistribution experiments (28) and the Ca_2 photodissociation experiment of Vigué, et. al. (29). Our full close coupled results for Sr + Ar are in good agreement with the radiative redistribution experiments. The half collision analysis leads to an especially simple and pleasing physical picture of the product alignment.

The same angular momentum transfer formalism applies to both radiative redistribution (23) and photodissociation (30). The transfer cross sections require a coherent sum of transition amplitudes resulting from P, Q, and R type radiative transitions, i.e, those having ΔJ = 1, 0, and +1 respectively. The transfer cross sections that result from applying the factored form of the $\mathbf{N}_F^+$ matrix can be expressed in terms of an angle

$$\theta_\Lambda = \alpha_\Lambda/2 - \Delta_s/2 \ .$$

The angle $\alpha_\Lambda/2$ originates from the frame transformation matrix U^+ in eq. 30 and represents the effect of adiabatic motion on the Born-Oppenheimer potential Λ. Semiclassically, it is the angle through which the molecular axis rotates in a complete half collision in the final state, that is, $(\pi-\theta_c)/2$, where θ_c is the final state classical deflection function. The classical deflection function enters since it is $2\partial\xi_\Lambda/\partial J$ and the adiabatic phases ξ_Λ vary slightly with J_F for adiabatic evolution following P, Q, and R excitation. The angle $\Delta_s/2$ originates from the effect of nonadiabatic Coriolis coupling between Σ and Π states in the nonadiabatic correction matrtix O^+. It represents the decoupling of electronic angular momentum from the rotating axis beyond a switching distance R_s.

This model leads to the same polarization ratio as found by Lewis, et al. (31) on the basis of an ad hoc geometric model. This model corresponds to the picture that angular momentum projection Λ rotates with the internuclear axis inside of some characteristic internuclear separation R_s but is decoupled and fixed in space for $R > R_s$. If molecular axis rotation is neglected, our half collision analysis predicts the J-independent recoil limit results (25,29), namely, respective $q = 0$ polarization ratios of 1/2 and 7/9 for Σ and Π excitation. The usefulness of the complete half collision analysis is that corrections to this simple J-independent recoil approximation are possible by introducing additional effects into $\mathbf{N}_F^+$. In the present case it happens to be simple to isolate the separate effects of adiabatic and nonadiabatic dynamics.

We have also used the half collision analysis to interpret Na + rare gas radiative redistribution experiments (31) in which the Na $^2P(j=1/2)/^2P(j=3/2)$ ratio was measured following wing absorption to the $^2\Sigma$ and $^2\Pi$ states (32). The recoil limit result is approached for fragment kinetic energy of about 2000 cm^{-1} for an argon collision partner, but at a much lower kinetic energy for the lighter He collision partner. The large departures of the fine structure branching ratio from the recoil limit for low (thermal) separation energies reflects the influence of the adiabatic potentials and their curve crossings.

REFERENCES

1) M.S. Shapiro, J. Chem. Phys. 56 (1972) 2582.
2) E. Segev and M.S. Shapiro, J. Chem. Phys. 73 (1980) 2001.
3) K.C. Kulander and J.C. Light, J. Chem. Phys. 73 (1980) 4337.
4) R.W. Heather and J.C. Light, J. Chem. Phys. 78 (1983) 5513.
5) S. Singer, K.F. Freed, and Y. B. Band, J. Chem. Phys. 77 (1982) 1942.
6) S. Singer, K.F. Freed, and Y. B. Band, J. Chem. Phys. 81 (1984) 3091.
7) J.A. Beswick, Quantum mechanical time-independent treatment of photodissociation dynamics, this volume.
8) F.H. Mies, Mol. Phys. 41 (1980) 953; Mol. Phys. 41 (1980) 973.
9) P.S. Julienne and F.H. Mies, J. Phys. B14, (1981) 4335.
10) F.H. Mies, J. Chem. Phys. 80 (1984) 2514.
11) F.H. Mies and P.S. Julienne, J. Chem. Phys. 80 (1984) 2526.
12) F.H. Mies and P.S. Julienne, A molecular half collision analysis of atomic lineshapes, in Spectral Lineshapes, Vol. 3, ed. F. Rostas (de Gruyter, Berlin, 1985) pp. 393-420.
13) P.S. Julienne and F.H. Mies, Half collision analysis of ^1P polarization redistribution, in Spectral Lineshapes, Vol. 3, ed. F. Rostas (de Gruyter, Berlin, 1985) pp. 525-526.
14) M.J. Seaton, Rept. Prog. Phys. 46 (1983) 167.
15) U. Fano, Comm. At. Mol. Phys. 10 (1981) 223; J. Opt. Soc. Am. 65 (1975) 979.
16) Ch. Jungen and O. Atabek, J. Chem. Phys. 66 (1977) 5584.
17) A. Guisti, J. Phys. B13 (1980) 3867; A. Guisti-Suzor and U. Fano, J. Phys. B17 (1984) 4267.

18) C.H. Greene, A.R.P. Rau, and U. Fano, Phys. Rev. A26 (1982) 2441; C.H. Greene, U. Fano, and G. Strinati, Phys. Rev. A19, (1978) 1485
19) R.Colle, J. Chem. Phys. 74 (1981) 2910.
20) F.Calogero, Variable Phase Approach to Potential Scattering (Academic Press, NY, 1967).
21) R.D. Levine, Mol. Phys. 22 (1971) 497.
22) F.H. Mies, Quantum theory of atomic collisions in intense laser fields, in Theoretical Chemistry: Advances and Perspectives,Vol. 6B, ed. D. Henderson (Academic Press, NY, 1981) pp. 127-198.
23) P.S. Julienne and F.H. Mies, Phys. Rev. A30 (1984) 831.
24) S.Y. Lee and E.J. Heller, J. Chem. Phys. 76 (1982) 3035.
25) S.J. Singer, K.F. Freed, and Y.B. Band, J. Chem. Phys. 79 (1983) 6060; J. Chem. Phys. 81 (1984) 3064.
26) J. Tellinghuisen and P.S. Julienne, J. Chem. Phys. 81 (1984) 5779.
27) P.S. Julienne, Nonadiabatic theory of line broadening, in Spectral Line Shapes, Vol. 2, ed. K. Burnett (de Gruyter, Berlin, 1983) pp. 769-786.
28) P. Thomann, K. Burnett, and J. Cooper, Phys. Rev. Lett. 45 (1980) 1325; W.J. Alford, K. Burnett, and J. Cooper, Phys. Rev. A27 (1983) 1310; W.J. Alford, N. Anderson, M. Belsley, J. Cooper, D. M. Warrington, and K. Burnett, Phys. Rev. A31 (1985) 2096.
29) J. Vigué, P. Grangier, G. Roger, and A. Aspect, J. de Physique Lett. 42 (1981) L532; J. Vigué, J. A. Beswick, and M. Broyer, J. Physique 44 (1983) 1225.
30) C.H. Greene and R.N. Zare, Ann. Rev. Phys. Chem. 33 (1982) 119.
31) M.D. Havey, G.E. Copeland, and W.J. Wang, Phys. Rev. Lett. 50 (1983) 1767.
32) L. Vahala, P. S. Julienne, and M.D. Havey, to be submitted (1985).

A Convergent Analysis of Radiative Matrix Elements in Atomic Lineshape Theory

Frederick H. Mies and Paul S. Julienne

Molecular Spectroscopy Division, National Bureau of Standards, Gaithersburg, MD 20899, U.S.A.

Yehuda B. Band

Ben-Gurion University of the Negev, Beer Sheva, Israel

Sherwin J. Singer

Department of Chemistry, University of Pennsylvania, Philadelphia, PA 19104, U.S.A.

ABSTRACT

For dipole allowed atomic transitions the radiative matrix element which defines the pressure-broadened atomic lineshape is only conditionally convergent. Using a commutator technique to redefine the integral, we isolate, and ultimately reject, the contribution of an indeterminant asymptotic surface integral that is associated with the energy normalization of the continuum wavefunctions which describe the binary collision of the atom and its perturber. The remaining contributions which are absolutely convergent, give the multichannel atomic lineshape which includes effects of non-adiabatic and inelastic scattering. Further we show the relationship of the commutator integral to the exact requirements of close-coupled scattering theory for radiatively-induced collisions. This scattering analysis suggests the interpretation of the convergent lineshape as an expression of multichannel inelastic collisions between field-dressed atomic states. This same interpretation applies both in the impact and the static limit. In this paper we make explicit comparisons which demonstrate the equivalence between the commutator integral and the numerical close-coupled results in the weak-field limit. Here we emphasize the static limit, well in the wings of the atomic line, where the Jablonski stationary phase WKB analysis is often applied with good effect.

1. Introduction

The calculation of the pressure-broadened lineshape for the dipole allowed atomic transition $A_i + h\omega \rightarrow A_f^*$ requires the evaluation of the following continuum-continuum matrix element (Mies 1981; Julienne and Mies 1984, Van Regemorter and Feautrier 1985)

$$S_{fi}^{rad} = -2\pi i \langle \Psi_f^-(E^-) | \vec{E}(\omega) \cdot \vec{\mu} | \Psi_i^+(E^+) \rangle \ . \qquad (1)$$

where the field-free multichannel wavefunctions $\Psi^{\pm}$ will be defined in section 2 below. This expression applies in the weak-field limit, when the electric field strength $\vec{E}(\omega)$ associated with the photon $h\omega$ is very small and the radiative scattering matrix element S_{fi}^{rad} can be evaluated in perturbation theory. The precise details of the lineshape analysis depends on the extent to which the incident photon is detuned from the exact atomic resonance energy $h\omega_{fi}^{o} = (E_f^* - E_i)$, where the detuning parameter Δ_{fi} is,

$$\Delta_{fi} = (h\omega - h\omega_{fi}^{o}) = (h\omega - E_f^* + E_i) \ . \qquad (2)$$

In the wings of the line, where Δ_{fi} is very large compared to the homogeneous width of the atomic transition, the absorption coefficient is directly proportional to the radiative scattering cross section determined by the transition matrix elements in Eq. (1) (Julienne and Mies 1984). The Lorentzian linewidth given by the impact approximation in the vicinity of the line center can also be expressed in terms of S_{fi}^{rad} (Mies and Julienne 1985, Van Regemortor and Feantrier 1985).

The expression of the lineshape in terms of Eq. (1) is a generalization of the standard time-independent molecular Franck-Condon factor approach to the line profile. A good recent review of line broadening theory which discusses the interrelationships and historical development of the various techniques has been given by Allard and Kielfopf (1982). The numerical evaluation of the integral (1) for dipole allowed transitions requires some care since the transition dipole operator $\vec{\mu}$ is non-vanishing even when the absorbing atom A and the perturber B are infinitely separated. Thus the resultant oscillatory integrand in Eq. (1) persists forever and does not give an absolutely convergent integral, and suitable techniques must be used to extract the physically meaningful, absolutely convergent components in this matrix element.

The standard way around this problem is to use Jablonski's method (1948). By invoking the stationary phase approximation with JWKB wave-functions, the offending terms are eliminated by a random phase argument, and simple semiclassical approximations to Eq. (1) result. These provide the basis for the unified Franck-Condon theory of the profile (Szudy and Bayliss 1975) and also provide justification for the standard quasistatic expressions for the wing profile (Hedges et al 1972; see also Herman and Sando 1978).

Convergent numerical techniques have been devised for the direct numerical evaluation of the full quantum integral (1). This has been done in two independent ways for neutral broadening by Herman and Sando (1978) and by Bieniek (1981). However, their formulae have been restricted to the

adiabatic approximation, that is, to using single channel wavefunctions in (1). Actually convergent ways to evaluate (1) for multichannel wavefunctions have already been derived for application to electron-atom (Feautrier et al 1976) and electron-ion (Seaton 1984) broadening problems.

In this paper we show how the commutator method of Herman and Sando (1978) can be generalized to yield an absolutely convergent integral using multichannel wavefunctions. The discussion is given in terms of the simple case of broadening of an atomic transition by collilsion with an atomic perturber. We emphasize that our procedure is applicable to more complicated systems. For example, our formalism can be generalized by a reinterpretation of channel labels to treat broadening of molecular adsorption lines by perturbers with internal structure. Our general expression reduces to those of Herman and Sando (1978) and Bieniek (1981) as special cases for single channel wavefunctions. We also show how a distorted wave analysis of the radiative scattering matrix for dressed atoms (Cohen-Tannoudji and Reynaud 1977, Courtens and Szöke 1977, Mies and Ben Aryeh 1981, Mies 1984) lead to the same formula. Thus, either close-coupled scattering calculations in which the radiation field couples asymptotically well-defined dressed states, or numerical evaluation of the perturbative expression (1) can be used to calculate the nonadiabatic version of the molecular Franck-Condon integrals.

The next section introduces the notation and, together with Appendix A, defines the multichannel wavefunctions. The third and fourth sections respectively describe the commutator and dressed atom scattering derivations of convergent integral formulae which replace (1). The final

section gives some illustrative numerical calculations and a brief discussion of lineshape theory in the wings of pressure broadened lines. The core profile, with special emphasis on the impact limit, together with some consideration of strong-field effects will be addressed in an accompanying paper (Mies and Julienne 1985).

2. Single perturber Theory

We consider broadening of the A→A* atomic transition line by a perturber B in the binary collision limit. In the so called optical collision process (Mies 1981) of interest here, the A→A* transition is asymptotically allowed. The two collision partners are treated as one absorbing diatomic species,

$$[A{+}{\cdot}{\cdot}B)_i + \varepsilon_i]^+ + \hbar\omega \longrightarrow [A^*{+}{\cdot}{\cdot}B)_f + \varepsilon_f]^- \qquad (3)$$

$$E^+ \qquad + \hbar\omega \qquad E^- \qquad (4)$$

The labels "i" and "f" denote the internal state of the quasidiatomic pair (with asymptotic internal energy E_i and E_f) before and after the binary absorption event, respectively. The superscript "+" refers to the system of incoming collision partners with total energy E^+, while "−" indicates outgoing particles after absorption of a photon during a collision. The multichannel wavefunctions $\Psi_i^+(E^+)$ and $\Psi_f^-(E^-)$ that appear in the matrix element (1) describe field-free continuum motion of A and A*, respectively, with respect to B. The wave function $\Psi_i^+(E^+)$ contains incoming particle flux in state i and outgoing particle flux in all channels. $\Psi_f^-(E^-)$ has incoming particle flux in all channels, but outgoing

flux in state f only. [The properties of multichannel continuum wave functions have been extensively discussed by Mies (1980, 1981, 1984) and Singer et. al. (1982, 1984, 1985).]

For simplicity of presentation we consider the collision partner B to be structureless. In this case, $E_i(E_f)$ is the internal energy of the A(A*) fragment. Generalization to more complicated cases in which the internal state of either atom may change during an optical collision is accomplished by making the labels i and f composite labels that indicate the asymptotic energy levels of both fragments. The same is true for optical collisions involving molecular species, in which the channel labels differentiate rovibronic levels. In order not to obscure the presentation of our method, we treat a very simple physical system in our derivations.

As the interatomic radial coordinate R becomes infinite, the fragments are further characterized by an incoming ε_i^+ and outgoing ε_f^- asymptotic relative kinetic energy which defines the total energies associated with the incoming

$$E^+ = E_i + \varepsilon_i^+ \tag{5a}$$

and outgoing

$$E^- = E_f^* + \varepsilon_f^- = E^+ + \hbar\omega \quad , \tag{5b}$$

molecular wavefunctions respectively.

The conservation of energy dictated by Eqs. (4) and (5b) indicates that an appropriate change in kinetic energy compensates for any detuning of the absorbed photon,

$$\varepsilon_f^- - \varepsilon_i^+ = \Delta_{fi} \tag{6}$$

The internal energy levles of the A···B or A^*···B quasimolecular pair can be described by a variety of equally acceptable R-dependent electronic-rotational basis functions. However, to describe proper scattering boundary conditions it is important to choose basis functions which asymptotically correlate with well-defined atomic levels of the non-interacting fragments. Such basis functions are referred to as channel states.

In general, the $A \rightarrow A^*$ transition in Eq. (3) will involve a set of $i=1,N^+$ initial ϕ_i and a separate set of $f=1,N^-$ final ϕ_f molecular channel states which correlate with the product of atomic states associated with the A···B and A^*··B collision complex respectively. We group these sets into two row vectors

$$\boldsymbol{\phi}^+ = [\phi_1^+, \cdots, \phi_i^+, \cdots, \phi_{N^+}^+] \tag{7a}$$

$$\boldsymbol{\phi}^- = [\phi_1^-, \cdots, \phi_f^-, \cdots, \phi_{N^-}^-] \tag{7b}$$

These channel states are but finite sub-sets of functions which span the entire space of the molecular Hamiltonian H_{AB} defined by the collision complex, with the single exception of the radial coordinate R. They are constructed with R-dependent molecular electronic-rotational wavefunctions which are combined to insure that, asymptotically, $\boldsymbol{\phi}^+$ (R=∞) and $\boldsymbol{\phi}^-$ (R=∞) become <u>exact</u> eigenfunctions of the atomic Hamiltonians ($H_A + H_B$), including any pertinent relativistic operators. Furher, each initial and final asymptotic channel state is an exact eigenfunction of the

relativistic angular momentum operator $\mathbf{l}_i$ and $\mathbf{l}_f$ respectively. In the absence of radiation, the total angular momenta of the collision complex are conserved and define exact quantum numbers J^+, M^+ and J^-,M^- at all interatomic distances. In the notation of molecular spectroscopy (Mies 1968, 1980, 1984) such asymptotic channel states correspond to Hund's case (e) electronic-rotational states. They have also been designated as the space-fixed atomic basis in the half-collision analysis of photodissociation of Singer, Freed and Band (1983, 1985).

Close coupled scattering theory is predicated on the assumption that a finite set of such channels can be preselected which are sufficient to describe any inelastic scatterings involved in the collision. Two such sets are presumed to have been chosen in Eq. (7), each sufficient to describe the inelastic scatterings of atom A and A^* respectively. We use the first row vector to expand the complete molecular wavefunction at total energy E^+

$$\Psi^+ (E^+) = \phi^+ \mathbf{F}^+ (E^+,R)/R \tag{8a}$$

and obtain a comparable row vector of orthogonal, energy-normalized continuum wavefunctions $\Psi^+(E^+)$ whose total degeneracy N^+ mimics the number of open (energetically accessible) atomic states which are contained in ϕ^+. Quite independently, we obtain a second set of continuum wavefunctions which we associate with the final state vector ϕ^-

$$\Psi^-(E^-) = \phi^- \mathbf{F}^-(E^-,R)^*/R \ . \tag{8b}$$

However the total energy E^- is prescribed by the incident molecular energy E^+ and the incident photon $\hbar\omega$ in Eq. (5b). Please observe that the notation + and - is chosen here to identify the separate sets of <u>incoming</u>

and outgoing continuum states involved in the photon absorption process, as well as to label the mutually orthogonal initial and final sets of channel states which are used to expand these multichannel wavefunctions. Actually both $\mathbf{F}^+$ and $\mathbf{F}^-$ are chosen to represent matrices of incoming radial solution vectors. The final state Ψ_f^- in Eq. (1) is required to exhibit outgoing boundary conditions and is simply given by the complex conjugate $\mathbf{F}^-(E^-,R)^*$ in Eq. (8b). These features are discussed in the Appendix. The relation of Ψ_f^- to outgoing particle flux and final state distributions in photodissociation has been discussed by Band et al (1981). Some of the confusing, and conflicting, aspects of the notations used in scattering theory are clarified by Roman (1965).

For use in Eq. (1), we are required to impose the following normalization condition, independently, on each of the square arrays of radial solution vectors in Eq. (8)

$$\int_0^\infty dR\ \mathbf{F}^\pm(E,R)^* \cdot \mathbf{F}^\pm(E^\pm,R) = \delta(E-E^\pm)\ \mathbf{1}^\pm \tag{9}$$

where $\mathbf{1}^\pm$ denotes a $N^\pm x N^\pm$ dimensional unit matrix. Each vertical vector in the matrix $\mathbf{F}^\pm$ represents a particular incoming solution to the appropriate set of coupled radial equations,

$$[\mathbf{T}^\pm + \mathbf{V}^\pm(R) - \epsilon^\pm]\ \mathbf{F}^\pm\ (E^\pm,R) = 0 \tag{10}$$

with asymptotic, multichannel, scattering boundary conditions as prescribed in the Appendix A. Both the radial kinetic energy operators

$$\mathbf{T}^\pm = -\frac{h^2}{2\mu_{AB}}\ \frac{\partial^2}{\partial R^2}\ \mathbf{1}^\pm \tag{11}$$

and the matrices of asymptotic relative kinetic energies $\epsilon^+=\{\epsilon_i^+\delta_{i,i'}\}$ and $\epsilon^- = \{\epsilon_\rho^-\delta_{\rho,\rho'}\}$ associated with the channel vectors ϕ^+ and ϕ^- in Eq. (7) are perfectly diagonal. Only the R-dependent, real, symmetric, interaction matrices $\mathbf{V}^\pm(R)$ are non-diagonal, and, to satisfy our channel state requirements, even these must be constrained to vanish identically at infinite interatomic separation,

$$\mathbf{V}^\pm(R) = \tilde{\mathbf{V}}^\pm(R) = \mathbf{V}^\pm(R)^* \underset{R\to\infty}{\sim} 0 \tag{12}$$

If radial couplings due to the implicit R-dependence of $\phi^\pm(R)$ are significant, as for instance when channels are constructed with adiabatic electronic-rotational states (Mies 1980), then antisymmetric radial operator $\partial/\partial R$ terms must be included in $\mathbf{V}^\pm(R)$, but the asymptotic constraint still persists.

In general there will be large off-diagonal elements in the interaction matrix $\mathbf{V}^+$ which can be expected to introduce strong inelastic couplings among the set of N^+ incoming channels ϕ^+. Similarly, the $\mathbf{V}^-$ matrix can cause significant non-adiabatic mixings among the N^- outgoing channel states ϕ^-. These inelastic scattering effects are summarized by the pair of unitary, symmetric scattering matrices $\mathbf{S}^+(E^+)$ and $\mathbf{S}^-(E^-)$ which we obtain by independently solving the two sets of coupled equations in Eq. (10) with the boundary conditions in Appendix A yielding the following constraints

$$\int_0^\infty dR\ \tilde{\mathbf{F}}^+(E,R)\cdot\mathbf{F}^+(E^+,R) = \delta(E-E^+)\ \mathbf{S}^+(E^+)$$

$$\int_0^\infty dR\ \tilde{\mathbf{F}}^-(E,R)^*\cdot\mathbf{F}^-(E^-,R)^* = \delta(E-E^-)\ \mathbf{S}^-(E^-)^* \tag{13}$$

For optical collisions the two sets of channel states selected in Eq. (7) must be of opposite total parity, and, thus, can never be coupled by any terms in the isolated molecular Hamiltonian $H_{AB}(R)$,

$$\langle\tilde{\phi}^+|H_{AB}|\phi^-\rangle = 0 \tag{14}$$

Rather, coupling is induced by the radiation field associated with the dipole operator in Eq. (1),

$$d_{fi}(R) = \langle\phi_f^+|\ \vec{\mathbf{E}}(\omega)\cdot\vec{\mu}|\phi_i^-\rangle \tag{15}$$

In the weak-field limit, when the electric field strength $|\vec{\mathbf{E}}|$ is very small, we can safely neglect any higher-order perturbations on the field-free molecular wavefunctions $\Psi^\pm$ and simply represent the radiative coupling in the following matrix form,

$$\mathbf{S}^{rad}(d) = -2\pi i \int_0^\infty \mathbf{F}^-(E^-,R)\cdot\mathbf{d}(R)\cdot\mathbf{F}^+(E^+,R)\ dR \tag{16}$$

Obviously this off-diagonal, radiatively-induced, scattering matrix $\mathbf{S}^{rad}(d)$ has the same (N^-xN^+) dimensionality as the dipole matrix $\mathbf{d}(R)$.

Because of the distortions of the atomic wavefunctions during the formation of the quasi-molecule in Eq. (3) there is, in general, an implicit R-dependence introduced into the matrix elements evaluated in Eq. (15),

$$d(R) \equiv a + b(R) \underset{R\to\infty}{\sim} a \tag{17}$$

and Eq. (16) can be evaluated in terms of two separate integrals,

$$S^{rad}(d) = S^{rad}(a) + S^{rad}(b) \tag{18}$$

The contribution from the asymptotically vanishing portion $b(R)=d(R)-d(\infty)$ of Eq. (17) will always yield a convergent integral for the S^{rad} (b) component in Eq. (18). In fact this quantity is the source of the oscillator strength in collision-induced absorption phenomena (Julienne 1982) where the asymptotic $A+ h\omega\to A^*$ transition is forbidden, and the asymptotic transition matrix $a=d(\infty)$ vanishes. Our concern is with allowed transitions, where $a\neq 0$, and we encounter undamped oscillations in the numerical evaluation of the continuum-continuum matrix elements which makes S^{rad} (a) only conditionally convergent.

3. Commutator Techniques for Evaluating $S^{rad}(a)$

Let us divide the asymptotic elements in Eq. (17) by the detuning in Eq. (6) and obtain the following dimensionless transition matrix elements which bear a direct correlation with the asymptotically allowed atomic transition dipole,

$$\alpha_{fi} = a_{fi}/\Delta_{fi} \tag{19}$$

This, in turn, is introduced into the definition of the following, Wronskian-like matrix of continuum wavefunctions for evaluation at some prescribed interatomic distance R,

$$W(\alpha,R) = \frac{\hbar^2}{2\mu_{AB}} \left[\frac{d\bar{F}^-}{dR}\alpha F^+ - \bar{F}^-\alpha \frac{dF^+}{dR} \right] \tag{20}$$

As we shall see, it is the asymptotic contribution of $W(\alpha,\infty)$ to the integral S^{rad} (a) in Eq. (18) and (16) which causes the conditional convergence of the continuum-continuum matrix element in Eq. (1).

Utilizing the following identity based on Eq. (10),

$$\tilde{F}^{-}a(T^{+} + V^{+} - \varepsilon^{+})F^{+} = (T^{-} + V^{-} - \varepsilon^{-})F^{-}\, aF^{+} \tag{21}$$

and noting that this must be satisfied for arbitrary values of the transition matrix **a**, we derive the following equivalence for the **a** contribution to the integrand in Eq. (16)

$$\tilde{F}^{-}aF^{+} = \tilde{F}^{-}(V^{-}\alpha - \alpha V^{+})F^{+} + dW(\alpha,R)/dR \tag{22}$$

Any numerical integration over the first RHS term is absolutely convergent because of the asymptotic decay of the interaction matrices $V^{\pm}(R)$ in Eq. (12). The complete differential dW/dR merely gives rise to surface-type terms which must be evaluated at the extremes of the integration, and, for $S^{rad}(a)$ we obtain,

$$\frac{S^{rad}(a)}{-2\pi i} = \int_{0}^{R_A} dR\ \tilde{F}^{-}aF^{+} + \int_{R_A}^{\infty} dR\ \tilde{F}^{-}(V^{-}\alpha - \alpha V^{+})F^{+} + [W(\alpha,\infty) - W(\alpha,R_A)] \tag{23}$$

We have chosen to separate the integration into two portions and only apply the equality in Eq. (23) beyond some arbitrarily assigned interatomic distance $R=R_A$. Use of this division is made in the by Mies & Julienne (1985) in the impact limit as $\Delta_{if} \to 0$. For purposes of this study, in the static wings of the atomic lineshape, it is sufficient to take $R_A=0$, and express (23) as follows,

$$S^{rad}(a) = -2\pi\, i \int_{0}^{\infty} dR\ \tilde{F}^{-}(V^{-}\alpha - \alpha V^{+})F^{+} \quad -2\pi i W(\alpha,\infty) \tag{24}$$

Here we have utilized the fact that both F^- and F^+ are well-behaved radial wavefunctions at $R \to 0$, such that

$$W(\alpha,0) = 0. \tag{25}$$

Using the asymptotic forms of $F^\pm$ in Eqs. (A1) and (A7) we obtain the following structure for $W_{fi}(\alpha,R)$ at large R,

$$2W_{fi}(\alpha,R) \sim \sum_{i'} [a_{fi'} w^{(+)}_{fi'}(R)] S^+_{i'i} + \sum_{f'} S^-_{ff'} [a_{f'i} w^{(-)}_{f'i}(R)] \tag{26}$$

where the reduced Wronskian matrices $w^{(\pm)}(R)$ are defined in (A8). Carried out to infinity we find,

$$2W_{fi}(\alpha,\infty) \sim \sum_{i'} [a_{fi'} \delta(\varepsilon^-_f - \varepsilon^+_{i'})] S^+_{i'i} + \sum_{f'} S^-_{ff'} [a_{f'i} \delta(\varepsilon^-_{f'} - \varepsilon^+_i)] . \tag{27}$$

As long as the photon frequency is not in perfect resonance with any of the asymptotic atomic transitions, the $W(\alpha,\infty)$ terms in Eq. (23) and (24) will vanish due to the delta functions in Eq. (27). Thus we can mathematically, and physically, justify the neglect of such non-convergent contributions to $S^{rad}(a)$ under all conceivable circumstances in lineshape theory.

If we use only single channel wavefunctions in Eq. (23) and make the choice $R_A=0$ then Eq. (24) reduces to the expression of Herman and Sando (1978). If, instead, we make the choice that R_A is large, but finite, beyond some range of the $V^\pm$ potentials such that the second integral in Eq. (23) is negligible, then we obtain the adiabatic expression of Bieniek (1981). Either choice of R_A leads to a convergent expression for both the single channel and the multichannel integral, since the fluctuating terms have been segregated into $W(\alpha,\infty)$, identified with delta functions, and promptly discarded. We prefer the choice $R_A=0$, since this leads to an

expression which is naturally damped by the vanishing asymptotic potentials. Thus, the complete atomic lineshape can be associated with the following, absolutely convergent integral,

$$S^{rad}(d) = -2\pi i \int_0^\infty dR\ \mathbf{F}^-(E^-,R)\cdot[\mathbf{b}(R)+(\mathbf{V}^- \mathbf{a} \mathbf{V}^+)]\cdot\mathbf{F}^+(E^+,R) \qquad (28)$$

In deriving Eq. (27) we have utilized the fact that the nuclear angular momentum quantum numbers ℓ_f and ℓ_i in Eq. (A8) must be equal. This is a consequence of the asymptotic selection rules for pure case (e) molecular channel states that are inherent in Eqs. (15) and (17),

$$a_{fi} = \delta_{\ell_f,\ell_i}\ a_{fi} \qquad (29)$$

This constraint does not apply to the collision-induced $\mathbf{b}(R)$ portions of the dipole matrix $\mathbf{d}(R)$ and can in fact lead to significant qualitative differences between allowed and forbidden lineshape behavior.

Exactly the same commutator analysis can be used to confirm the validity of the normalization implied in Eq. (9). If we replace $\mathbf{F}^-(E^-)$ with $\mathbf{F}^+(E)^*$ and $\mathbf{a}$ with 1^+ in Eq. (22), we derive the following

$$\begin{aligned}\int_0^R dR'\mathbf{F}^+(E,R')^*\cdot\mathbf{F}^+(E^+,R') &\underset{R\to\infty}{\sim} \frac{\hbar^2}{2\mu_{AB}(E^+-E)}\left[\frac{d\mathbf{F}^+(E,R)^*}{dR}\mathbf{F}^+(E^+,R)-\mathbf{F}^+(E,R)^*\frac{d\mathbf{F}^+(E^+,R)}{dR}\right] \\ &\sim \delta(E-E^+)\ \mathbf{S}^+(E)^*\ \left[\frac{\mathbf{S}^+(E)+\mathbf{S}^+(E^+)}{2}\right] \\ &\sim \delta(E-E^+)\ 1^+ \qquad (30)\end{aligned}$$

The same procedure confirms the proper normalization of the outgoing radial wavefunctions $\mathbf{F}^-(E^-)$ in Eq. (9).

4. Analysis of Lineshape Using Close-Coupled Theory and Dressed Channel States

Associated with each incident channel ϕ_i^+ is a radiative number state $|n\rangle$ which defines the properties of the incident radiation field. A corresponding number state $|n-1\rangle$ is associated with each final channel state ϕ_f^- and indicates the absorption of a single photon as portrayed in Eq. (3). In particular, the electric field strength in Eq. (15) is related to the number of photons n contained in the source free volume V with the prescribed energy $h\omega$ (and other qualities of interest) as follows,

$$|\mathbf{E}(\omega)|^2 = 2\pi\hbar\omega(n/V) \tag{31}$$

In deriving Eq. (1) we have relied on this quantity being sufficiently small to permit the neglect of any radiative perturbation of the field-free molecular continuum states Ψ_i^+ and Ψ_f^- which we associate with the bare channels ϕ_i^+ and ϕ_f^- respectively. However, for optical collisions, these are really not the proper scattering channels that should be used to define the absorption. By considering the proper dressed atomic states, and employing the resultant dressed channel states that are generated by the asymptotic radiative coupling, we can gain a good deal of insight, and actually obtain a more general perturbative expression for S^{rad}. To first order in $\mathbf{E}(\omega)$ we will retrieve the convergent perturbative result in Eq. (28).

We have previously developed the proper close-coupled equations for the full molecule-field scattering wavefunctions (Mies 1981)

$$\Omega_i^+(n,E) = \sum_{i'} \{\phi_i^+ \otimes |n\rangle\} F_{i'i}(n,E,R) + \sum_f \{\phi_f^- \otimes |n-1\rangle\} F_{fi}(n,E,R) \qquad (32)$$

$$= \sum_j \xi_j(n) F_{ji}(n,E,R)$$

where $\xi_j(n)$ designates an element on the $N=(N^+ + N^-)$ dimensional row vector of molecule-field channel states composed of products $\psi_i^+ \otimes |n\rangle$ and $\phi_f^- \otimes |n-1\rangle$ generated from Eq. (7)

$$\xi(n) = [\cdots, \phi_i^+ \otimes |n\rangle, \cdots, \phi_f^- \otimes |n-1\rangle, \cdots] \qquad (33)$$

The (NxN) matrix of radial wavefunctions $\mathbf{F}(n,E,R)$ is evaluated at the combined molecule-field energy E

$$E = E^+ + n\hbar\omega = E^- + (n-1)\hbar\omega \qquad (34)$$

and denotes proper incoming scattering solution vectors originating from the following set of coupled equations,

$$\left[\begin{array}{c|c} \mathbf{T}^+ + \mathbf{V}^+ - \boldsymbol{\varepsilon}^+ & \mathbf{d}(n,R) \\ \hline \mathbf{d}(n,R) & \mathbf{T}^- + \mathbf{V}^- - \boldsymbol{\varepsilon}^- \end{array}\right] \mathbf{F}(n,E,R) = 0. \qquad (35)$$

In the limit, when $n \to 0$ and the intensity-dependent radiative coupling matrix $\mathbf{d}(n,R)$ in Eq. (15) vanishes, we retrieve the field-free solution vectors that are defined by Eq. (10) and used in Eq. (1),

$$\mathbf{F}(n,E,R) \underset{n\to 0}{\sim} \left[\begin{array}{c|c} \mathbf{F}^+(E^+,R) & 0 \\ \hline 0 & \mathbf{F}^-(E^-,R) \end{array}\right] \qquad (36)$$

Note that unlike the molecular interaction matrices $\mathbf{V}^{\pm}(R)$ which are constructed to vanish identically as $R \to \infty$, the asymptotic radiative coupling $\mathbf{d}(n,\infty) \to \mathbf{a}(n)$ in Eq. (17) never vanishes in the presence of a

field. Since a scattering matrix element, such as S_{fi}^{rad} (d), is meant to describe the transition probability between pairs of <u>asymptotically uncoupled</u> states which can be independently prepared before collision, and asymptotically observed after the collision event, it should be apparent that our molecule-field channel states $\xi(n)$ are improper scattering states.

Let us define an asymptotic, orthogonal transformation of our channel states

$$\xi^D = \xi U^D \tag{37}$$

such that $\tilde{U}^D U^D = 1$ and the asymptotic interaction vanishes,

$$\tilde{U}^D \left[\begin{array}{c|c} T^+ - \varepsilon^+ & \tilde{a}(n) \\ \hline a(n) & T^- - \varepsilon^- \end{array}\right] U^D = \left[\begin{array}{c|c} T^+ - w^{\pm}(a) & 0 \\ \hline 0 & T^- - w^-(a) \end{array}\right] . \tag{38}$$

The new set of diagonalized kinetic energies $w^{\pm}(a)$ (Not to be confused with the reduced Wronskian matrices $\mathbf{w}^{(\pm)}(R)$ of the previous section and Appendix A) obtained from the secular equation,

$$\left| \left[\begin{array}{c|c} w^+ - \varepsilon^+ & \tilde{a}(n) \\ \hline a(n) & w^- - \varepsilon^- \end{array}\right] \right| = 0, \tag{39}$$

reflect the <u>dressing</u> of the asymptotic atomic states associated with the transition $A_i + \hbar\omega \to A_f^*$. We are, of course, concerned with the weak-field limit where the radiative interaction matrix $\mathbf{a}$, and the corresponding reduced matrix $\boldsymbol{\alpha}$ in Eq. (19) are very small. To second-order we obtain the following estimates for the field-shifted asymptotic kinetic energies of the incident, and final molecule-field channel states ξ^D

$$w_i^+(a) \simeq \varepsilon_i^+ - (\tilde{\mathbf{a}}\boldsymbol{\alpha})_{ii} = \varepsilon_i^+ - \sum_f a_{fi}^2/(\varepsilon_f^- - \varepsilon_i^+) \tag{40a}$$

$$w_f^-(a) \simeq \varepsilon_f^- - (a\bar{a})_{ff} = \varepsilon_f^- - \sum_i a_{fi}^2/(\varepsilon_f^- - \varepsilon_i^+) \tag{40b}$$

If we recognize that a_{fi} is related to the Rabi frequency Ω_{fi} for the asymptotic atomic transition $\Omega_{fi} \equiv 2a_{fi}/h$ and note that the atomic detuning frequency $(\delta\omega)_{fi}$ is related to the asymptotic kinetic energy difference in Eq. (6), $(\delta\omega)_{fi} = \Delta_{fi}/h$, we find that the shifts in Eq. (41) are identical to the usual expressions for dressed atomic states in weak-field limit (Mies and Ben Aryeh 1981, Mies 1983).

$$w_f^- - w_i^+ = \Delta_{fi} \left[1 + \sum_{f'} \frac{a_{f'i}^2}{\Delta_{f'i}\Delta_{f'i}} + \sum_{i'} \frac{a_{fi'}^2}{\Delta_{fi}\Delta_{fi'}} \right]. \tag{41a}$$

$$\equiv \Delta_{fi}\,[1 + r_{fi}] \tag{41b}$$

Let us define a field-shifted reduced matrix x_{fi} comparable to α_{fi} in Eq. (19),

$$x_{fi} = \frac{a_{fi}}{w_f^- - w_i^+} = \alpha_{fi}(1 - r_{fi}) \ . \tag{42}$$

To second-order in $\mathbf{x}$ the orthogonal matrix $\mathbf{U}^D$ may be expressed as follows,

$$\mathbf{U}^D = \left[\begin{array}{c|c} 1^+ - \tilde{\mathbf{x}}\,\mathbf{x}/2 & -\tilde{\mathbf{x}} \\ \hline \mathbf{x} & 1^- - \mathbf{x}\,\tilde{\mathbf{x}}/2 \end{array} \right] \tag{43}$$

Transforming the expansion in Eq. (32) to the dressed-channel basis

$$\Omega^+ = \xi\mathbf{F}(n,E,R) = (\xi\mathbf{U}^D)\ (\mathbf{U}^D\mathbf{F}(n,E,R)) = \xi^D\mathbf{F}^D(n,E,R) \tag{44}$$

we obtain the following set of coupled equations for the radial wavefunctions $\mathbf{F}^D$

$$\left[\begin{array}{c|c} \mathbf{T}^+ + \mathbf{V}^+ - \mathbf{w}^+(a) + \mathbf{Y}^+ & \mathbf{b} - (\mathbf{V}^+\tilde{\mathbf{x}} - \tilde{\mathbf{x}}\mathbf{V}^-) \\ \hline \mathbf{b} + (\mathbf{V}^-\mathbf{x} - \mathbf{x}\mathbf{V}^+) & \mathbf{T}^- + \mathbf{V}^- - \mathbf{w}^-(a) + \mathbf{Y}^- \end{array} \right] \mathbf{F}^D(n,E,R) = 0 \tag{45}$$

where the $\mathbf{Y}^{\pm}(R)$ matrices vanish as $R\to\infty$ and only contain second-order terms

$$\mathbf{Y}^{+}(R) = \tilde{\mathbf{x}}\,\mathbf{V}^{-}\mathbf{x} - (\tilde{\mathbf{x}}\mathbf{x}\mathbf{V}^{+} + \mathbf{V}^{+}\tilde{\mathbf{x}}\mathbf{x})/2 + (\tilde{\mathbf{b}}\mathbf{x} + \tilde{\mathbf{x}}\mathbf{b}) \tag{46a}$$

$$\mathbf{Y}^{-}(R) = \mathbf{x}\,\mathbf{V}^{+}\tilde{\mathbf{x}} - (\mathbf{x}\tilde{\mathbf{x}}\mathbf{V}^{-} + \mathbf{V}^{-}\mathbf{x}\tilde{\mathbf{x}})/2 - (\mathbf{x}\tilde{\mathbf{b}} + \mathbf{b}\tilde{\mathbf{x}}) \tag{46b}$$

In the first-order limit we can see that the perturbative solution to Eq. (45) yields the same diagonal blocks of field-free solutions as Eq. (36), with an off-diagonal radiative coupling $\mathbf{b}+(\mathbf{V}^{-}\alpha-\alpha\mathbf{V}^{+})$ matrix which yields the approximation (Taylor 1972, Mies 1981)

$$\mathbf{S}^{rad}(d) \simeq -2\pi i\ \langle \mathbf{F}^{-}(E^{-})^{*}|\mathbf{b} + \mathbf{V}^{-}\alpha-\alpha\mathbf{V}^{+}|\ \mathbf{F}^{+}(E^{+})\rangle \tag{47}$$

in complete agreement with our commutator analysis in Eq. (28).

Obviously by referring our radiative scattering matrix elements S_{fi}^{rad} to the proper dressed channels ξ_f^D and ξ_i^D rather than ξ_f and ξ_i we have performed the equivalent of ignoring the indeterminant surface integral $\mathbf{W}(\alpha,\infty)$ in Eq. (24). In deriving Eq. (47) we have neglected the shift parameter r_{fi} in Eqs. (41) and (42) and taken $\mathbf{x} = \mathbf{a}$. However, the close-coupling analysis is not committed to small perturbation, and we can progress to second-order by solving Eq. (45), or to arbitrary order in the radiative coupling if we solve the coupled equations (35) directly, subject to the dressed state boundary conditions implied by Eq. (44). For example, the dressing of an isolated atomic transition always insures that $r_{fi} \leq 0$ and $x_{fi} \leq \alpha_{fi}$. This effect introduces a saturation of the pressure-broadened half-width in intense laser fields (Mies and Julienne 1985).

5. Discussion

The numerical solution of the close-coupled equations (45) between dressed levels never causes any difficulties associated with conditional convergence. There is an absolute convergence of the radiative scattering matrix element S_{fi}^{rad} obtained from imposing the following asymptotic structure on $F^D(n,E,R)$

$$F_{fi}^{D}(n,E,R) \underset{R\to\infty}{\sim} (i/2)[\delta_{fi}\, f_i^{(-)}(w_i^{+}(a),R) - g_f^{(+)}(w_f^{-}(a),R)\, S_{fi}^{rad}] \qquad (48)$$

where the appropriate incoming $f_i^{(-)}$ and outgoing $g_f^{(+)}$ Bessel functions are defined in Appendix A. However, care must be taken to use the correctly shifted asymptotic kinetic energies defined by the secular Eq. (39) rather than the field-free values ϵ_i^{+} and ϵ_f^{-}. Essentially what we are defining in Eq. (48) are the particular set of degenerate continuum wavefunctions needed to describe the collision-induced absorption between the stationary field-dressed states of the asymptotic atom A in the radiative field associated with the Rabi frequency in Eq. (42).

This close-coupled procedure avoids any commitment to weak fields and perturbative estimates of S_{fi}^{rad}. However, to first order in the asymptotic radiative coupling a_{fi} the dressed-state eigenvalues in Eq. (41) are unshifted, and S_{fi}^{rad} (d) is given by the first-order distorted wave approximation in Eq (47). By referencing our close-coupled wavefunctions to the dressed channels ξ_f^D and ξ_i^D rather than ξ_f and ξ_i in Eq. (58) we are essentially performing the equivalent of ignoring the indeterminant surface integral $W_{fi}(\alpha,\infty)$ in Eq. (24).

We have performed multichannel close-coupled calculations of the $Sr(^1S) \rightarrow Sr(^1P)$ transition broadened by collision with Ar (Julienne, 1983, 1985). One component of the absorption rigorously reduces to a simple radiative transition between a single channel, elastically scattered, ground state continuum $\Psi_i^+ (E^+) = \phi_i^+ F_{ii}^+(E_i^+,R)$ with a field-free radial function described by scattering from the isolated molecular potential $V_{ii}^+(R)$ with a resultant phase shift $\eta_i(E_i^+)$

$$F_{ii}^+ (E^+,R) \underset{R\to\infty}{\sim} e^{i\eta_i}\left(\frac{2\mu_{AB}}{\hbar^2\pi k_i}\right)^{1/2} \sin (k_iR-\pi\ell_i/2+\eta_i) \qquad (49)$$

and a single channel, elastically scattered, excited state continuum $\Psi_f^-(E^-) = \phi_f^- F_{ff}^-(E^-)^*$ with a phase shift $\eta_f(\varepsilon_f^-)$ determined by scattering off the molecular potential $V_{ff}^-(R)$

$$F_{ff}^- (E^-,R)^* \sim e^{-i\eta_f}\left(\frac{2\mu_{AB}}{\hbar^2\pi k_f}\right)^{1/2} \sin(k_fR -\pi\ell_f/2 + \eta_f). \qquad (50)$$

In the spectroscopic terminology one would associate with Eq. (3), we are considering the Q-branch continuum-continuum absorption of the $^1\Sigma(X)\rightarrow{}^1\Pi(A)$ transition of the (SrAr) quasimolecule.

A comparison of the exact two state close-coupling matrix elements obtained from Eq. (48) and the numerically evaluated matrix elements in Eq. (47) confirms the weak-field result

$$S_{fi}^{rad}(a) \underset{a\to 0}{\sim} -2\pi i \; a_{fi} \; \langle F_{ff}^-(E^-)^* \left| \frac{V_{ff}^- - V_{ii}^+}{\varepsilon_f^- - \varepsilon_i^+} \right| F_{ii}^+(E^+)\rangle \qquad (51)$$

This is demonstrated in Table 1 for a range of detunings. Herman and Sando (1978) have already derived and made use of this limited two-state version of Eq. (47) for calculating the wings of resonant Li and Na lines.

This expression allows for a convergent, fully quantal evaluation of optical collision cross-sections without recourse to the usual, although generally quite satisfactory (Mies 1968, Jablonski 1945) expressions based on the JWKB and stationary phase approximations (see Allard and Kielkopf 1982). Although we have made a more explicit analysis of the indeterminant character of the matrix element S_{fi}^{rad} (a), which requires the isolation of the asymptotic surface term in Eq. (24), we conclude that this can legitimately be ignored from further consideration. Thus we have used a more rigorous and general procedure to justify the specialized Herman and Sando result in Eq. (51).

Our more general expression in Eq. (47) does include multichannel couplings and allows for the possibility of inelastic, and non-adiabatic contributions to atomic lineshapes. Again, a comparable version of this multichannel, first-order expression has appeared in the lineshape literature, although it has been specialized to the Stark-broadening of the hydrogen atom (Feautrier et al 1976). A more general multichannel expression for Stark-broadening can be extracted from Seaton's (1981) analysis of free-free transitions in electron-atom collisions, although we have made a more explicit outline of the proper boundary conditions, and a less restrictive application of the theory.

We would claim that our major contribution is to recognize that the convergent first-order matrix element in Eq. (47) corresponds to the scattering among asymptotic dressed states of the absorbing atom. Since the dressed field-atom states in Eq. (37) are defined as stationary

eigenfunctions of the complete molecule-field Hamiltonian at infinite interatomic separation we have removed the troublesome coupling in the asympototic regions of the molecular continuum states.

This finding means that we can now confidently equate S_{fi}^{rad} in Eq. (1) with the numerically derived elements obtained from solution of the close-coupled equations (35) transformed to the appropriate boundary conditions in Eq. (48). In fact, since stable close-coupling codes are required to generate the multichannel wavefunctions in Eqs. (8) and (10), it is often a simple matter to merely expand the set of coupled equations, as in Eq. (35) or (45), to directly include the radiative coupling between channel states as required by the boundary conditions in (48) and completely avoid explicit numerical quadrature of the multichannel matrix elements in Eq. (47). Obviously, this convenience is accomplished by sacrificing computer time to solve for larger sets of coupled radical equations.

When performing the close-coupled calculations among dressed levels to extract $S_{fi}^{rad}(d)$ we must choose a representative field strength $|\vec{E}(\omega)|$ in Eq. (15) sufficiently small to insure that $S_{fi}^{rad}(d)$ in Eq. (48) remains linearly proportional to the radiative coupling strength $\mathbf{d}(R)$ in Eq. (35) and yet sufficiently large to insure the numerical accuracy the resultant scattering matrix elements. As long as the magnitude of $S_{fi}^{rad}(d)$ remains below about 10^{-3} it seems to remain quite linear in $\mathbf{d}$, and there is a one-to-one correspondence between Eq. (28) and the values extracted from (48). This is substantiated by the results in Table 2. Of course true deviations from linearity must ultimately prevail as the actual field

strength in Eq. (31) increases, reflecting the onset of saturation of the continuum-continuum transition in Eq. (3). This is most prominent near line-center, and is given greater attention in the forthcoming paper on the impact limit (Mies and Julienne 1985).

Acknowledgements

F.H.M. and P.S.J. acknowledge that this work was sponsored in part by the U.S. Air Force Office of Scientific Research. Y.B.B. acknowledges support from a grant by the U.S.-Israel Binational Science Foundation.

Appendix A: Asymptotic Properties of Multichannel Continuum Wavefunctions

In contrast to conventional scattering notation we have used + and − to label two separate, mutually orthogonal, sets of initial ϕ^+ and final ϕ^- channel states each with its own matrix of close-coupled radial solution vectors $\mathbf{F}^+$ and $\mathbf{F}^-$ respectively. These field-free scattering wavefunctions are expected to adequately, and independently, describe any inelastic couplings among the set of initial, and the set of final atomic states involved in the absorption. Both $\mathbf{F}^+$ and $\mathbf{F}^-$ are assigned the usual incoming boundary conditions appropriate to defining the inelastic cross-sections induced by collisions with the perturbing atom. Once radiative coupling is introduced between the two sets of channels we associate ϕ^+ with the subset of incoming channel states defined by the absorption, while ϕ^- becomes identified with the subset of excited outgoing channel states. The conventional boundary conditions in F^+ are adequate to define the incoming continuum state Ψ_i^+ required in Eq. (1). The specific normalization of $\mathbf{F}^+$ and $\mathbf{F}^-$ that we introduce in this appendix is carefully chosen to insure that $(\mathbf{F}^-)^*$ also defines the proper outgoing scattering state Ψ_f^- in Eq. (8b) and (1).

The radial wavefunctions in Eq. (8a) have the following asymptotic structure

$$\mathbf{F}^+(E^+,R) \sim i/2\,[\mathbf{f}^{(-)}(\varepsilon^+,R) - \mathbf{f}^{(+)}(\varepsilon^+,R)\,\mathbf{S}^+(E^+)] \qquad \text{(A1)}$$

where $\mathbf{f}^{(\pm)}(\varepsilon^+,R)$ are diagonal ($N^+ \times N^+$) matrices of energy-normalized incoming (−) and outgoing (+) spherical waves [see Roman (1965) for the distinction between incoming Ψ^+ and outgoing $(\Psi^+)^*$ scattering states and these spherical Bessel functions],

$$f_i^{(\pm)}(\varepsilon_i^+,R) \underset{R\to\infty}{\sim} \left(\frac{2\mu_{AB}}{\hbar^2\pi k_i}\right)^{1/2} \exp[\pm i(k_i R-\ell_i/2)] \tag{A2}$$

Each incoming channel state ϕ_i^+ has a well-defined asymptotic kinetic energy ε_i^+ which is prescribed by the total energy E^+, which, in turn, determines the magnitude of the asymptotic radial wavevector k_i

$$k_i^2(E^+) = 2\mu_{AB}\varepsilon_i^+/\hbar^2 = 2\mu_{AB}(E^+-E_i)/\hbar^2 \tag{A3}$$

The asymptotic constraint imposed on the interaction matrix $\mathbf{V}^+(R)$ in Eq. (12) insures that each of the resultant case (e) channel states ϕ_i^+ correlate with a specific nuclear angular momentum quantum number, or partial wave ℓ_i. These running waves only occur for open channels where $k_i(E^+)$ is real and positive, such that

$$f_i^{(\pm)'} \equiv df_i^{(\pm)}/dR \underset{R\to\infty}{\sim} \pm ik_i f_i^{(\pm)} \tag{A4}$$

The particular normalization in Eq. (A2) insures the following asymptotic property

$$\left(\frac{\hbar^2}{4\mu_{AB}}\right)\frac{[f_i^{(\pm)} f_j^{(\mp)'} - f_i^{(\pm)'} f_j^{(\mp)}]}{(\varepsilon_i^+ - \varepsilon_j^+)} \underset{R\to\infty}{\sim} e^{\pm i\pi(\ell_j-\ell_i)/2}\delta(\varepsilon_i^+ - \varepsilon_j^+). \tag{A5}$$

This is rationalized in delta function theory by appealing to the subsequent effect of averaging of Eq. (A6) over small increments of energy about $(\varepsilon_i^+ - \varepsilon_j^+)$. This procedure is physically justified because scattering eigenstates, which are not normalizable, are ultimately used to expand states for which the square integrable normalization does exist. (See Messiah (1958) where this procedure is discussed in detail and its

equivalence to other methods of generalizing orthonormality relations to the continuum is demonstrated). The same limiting procedure is used to show that we may properly write,

$$f_i^{(\pm)}(\varepsilon_i^+,R)\ f_j^{(\pm)}(\varepsilon_j^+,R) \underset{R\to\infty}{\sim} 0 \qquad \text{(A6)}$$

A structure comparable to $F^+(E^+,R)$ is defined for incoming radial solution vectors $F^-(E^-,R)$ associated with the set of outgoing channels ϕ_f^- in Eq. (10),

$$F^-(E^-,R) \underset{R\to\infty}{\sim} i/2[g^{(-)}(\varepsilon^-,R) - g^{(+)}(\varepsilon^-,R)\ S^-(E^-)] \qquad \text{(A7)}$$

In place of $f^{(\pm)}(\varepsilon^+,R)$ we introduce diagonal (N^- x N^-) matrices of spherical Bessel functions $g^{(\pm)}(\varepsilon^-,R)$ as defined by the asymptotic kinetic energy ε_f^-, wavevector k_f and partial wave quantum number ℓ_f associated with channel state ϕ_f^-. Actually these running waves exhibit the same structure and properties given for $f^{(\pm)}$ in Eqs. (A2)-(A6). In fact the cross-terms between these sets will also conform to Eqs. (A5) and (A6)

$$w_{fi}^{(\pm)}(R) = \frac{[g_f^{(\mp)} f_i^{(\pm)\prime} - g_f^{(\mp)\prime} f_i^{(\pm)}]}{(\varepsilon_f^- - \varepsilon_i^+)} \frac{\hbar^2}{4\mu_{AB}} \underset{R\to\infty}{\sim} e^{+i(\ell_f-\ell_i)/2}\ \delta(\varepsilon_f^- - \varepsilon_i^+) \qquad \text{(A8)}$$

$$g_f^{(\pm)}\ f_i^{(\pm)} \underset{R\to\infty}{\sim} 0 \qquad \text{(A9)}$$

However, we have introduced the distinct notation $g^{(\pm)}$ to emphasis that these matrices as compared to $f^{(\pm)}$ are of different dimension, are associated with a separate sub-set of channel states, and are evaluated at a different total energy E^- as prescribed by Eq. (5).

Solving the two sets of coupled Eqs. (10) separately at total energies E^+ and E^- we obtain an independent pair of symmetric, unitary scattering matrices $S^+(E^+)$ and $S^-(E^-)$ which separately embody all the inelastic, non-adiabatic couplings among the incoming ϕ^+ and outgoing ϕ^- channel states respectively,

$$S^{\pm}(S^{\pm})^* = S^{\pm}(S^{\pm})^* = 1^{\pm} \tag{A10}$$

The boundary conditions imposed on Eqs. (A1) and (A7) have been devised to insure that

$$F^{\pm}(E^{\pm},R) = F^{\pm}(E^{\pm},R)^* \, S^{\pm}(E^{\pm}) \tag{A11}$$

which is necessary to satisfy Eq. (13). Further, given that both F^+ and F^- satisfy proper boundary conditions for the usual, physically significant, incoming states of scattering theory, the result in Eq. (A11) confirms that the complex conjugate function $F^-(E^-,R)^*$ we have used in Eq. (8b) does, in fact, represent the proper outgoing state that we require in Eq. (1).

References

Band Y B Freed K F and Kouri D J 1981 J. Chem. Phys. 74 4380.

Bieniek R J 1981 Phys. Rev. A 23 2826.

Cohen-Tannoudji C and Reynaud S 1977 J. Phys. A10 345, 365.

Courtens E and Szöke A 1977 Phys. Rev. A 15 1588.

Feautrier N Tran Minh N and Van Regemorter H 1976 J. Phys. B9 1871.

Hedges R E M Drummond D L and Gallagher A 1972 Phys. Rev. A 6 1519.

Herman P S and Sando K M 1978 J. Chem. Phys. 68 1153.

Jablonski A 1945 Phys. Rev. 68 78.

Julienne P S 1982 Phys. Rev. A 26 3299.

_____ 1983 Spectral Line Shapes Vol. 2 (Ed. K. Burnett, deGruyter, Berlin), 769.

_____ 1985 Spectral Lines Shapes Vol. 3 (Ed. F. Rostas, deGruyter, Berlin).

Julienne P S and Mies F H 1984 Phys. Rev. A 30 831.

Messiah A 1958 Quantum Mechanics Vol. I (Wiley, NY) pp. 110-112, 179-194.

Mies F H 1968 J. Chem. Phys. 48 482.

_____ 1980 Molec. Phys. 41 953, 973.

_____ 1981 Theoretical Chemistry: Advances and Perspectives, Vol. 6B (Ed. D. Henderson, Academic Press, NY) 127-198.

_____ 1983 J. Quant. Spectrosc. Radiat. Transfer 29 237.

_____ 1984 J. Chem. Phys. 80 2514.

Mies F H and Ben Aryeh Y 1981 J. Chem. Phys. 74 53.

Mies F H and Julienne P. S. 1985 manuscript in preparation.

Roman P 1965 Advanced Quantum Theory (Addison-Wesley, Reading Mass) p. 294.

Seaton M J 1981 J. Phys. B14 3827.

Singer S J Freed K F and Band Y B 1983 J. Chem. Phys. 79 6060.

_____ 1984 J. Chem. Phys. 81 3064.

_____ 1985 Adv. Chem. Phys.

Szudy J and Baylis W E 1975 J. Quant. Spectrosc. Radiat. Transfer 15 641.

Taylor J R 1972 Scattering Thoery (Wiley, NY)

VanRegemorter H and Feautrier N 1985 J. Phys. B18 2673.

Table I. Comparison of close-coupled and perturbative radiative scattering matrix elements evaluated for radiative coupling strength $a=1.674\times10^{-4}$ cm.$^{-1}$ corresponding to a radiative flux $F_w = 10^{-2}$ watts/cm^2 in Sr + Ar system.

	J=0[a]		J=40		J=150	
Δ_{12}/cm^{-1}	$\lvert S_{12}^{rad}\rvert$	$\arg(S_{12}^{rad})$[b]	$\lvert S_{12}^{rad}\rvert$	$\arg(S_{12}^{rad})$	$\lvert S_{12}^{rad}\rvert$	$\arg(S_{12}^{rad})$
-50.0	1.1979(-5)[c]	2.1979	1.4086(-5)	-0.1151	2.4218(-5)	1.8389
	1.1979(-5)[d]	2.1976	1.4086(-5)	-0.1153	2.4217(-5)	1.8371
-20.0	4.3643(-6)	2.7461	1.3909(-5)	0.6519	3.3967(-6)	-0.8593
	4.3588(-6)	2.7457	1.3911(-5)	0.6518	3.3959(-6)	-0.8611
- 1.0	3.4027(-4)	1.1641	2.8557(-4)	-0.8012	3.3916(-4)	-0.6293
	3.4027(-4)	1.1637	2.8558(-4)	-0.8013	3.3914(-4)	-0.6311
+ 0.1	3.2451(-3)	-2.0678	2.5898(-3)	2.2575	3.1094(-3)	-0.6171
	3.2451(-3)	-2.0681	2.5399(-3)	2.2573	3.1097(-3)	-0.6190
+ 1.0	3.1020(-4)	-2.1416	2.3674(-4)	2.1896	2.8671(-4)	-0.6074
	3.1019(-4)	-2.1418	2.3678(-4)	2.1895	2.8675(-4)	-0.6092
+20.0	1.2597(-6)	-0.5339	5.3994(-6)	-2.3647	2.9928(-6)	-0.4199
	1.2576(-6)	-0.5343	5.3982(-6)	-2.3649	2.9930(-6)	-0.4218
+50.0	1.2986(-6)	-2.8747	5.9208(-7)	1.7570	3.7391(-8)	-0.1986
	1.2985(-6)	-2.8750	5.9233(-7)	1.7568	3.7342(-8)	-0.2006
+100.0	1.2478(-7)	2.8492	3.5848(-8)	1.4673	6.5553(-9)	-0.0158
	1.2459(-7)	2.8489	3.5828(-8)	1.4671	6.5774(-9)	-0.0177

(a) J is the total angular momentum of the initial and final molecular continuum states in the quasimolecular Sr+Ar Q-branch transition.

(b) Argument of the complex S_{12}^{rad} matrix element in radians.

(c) Upper element in each pair is obtained from solution of coupled equations.

(d) Lower element in each pair of entries is evaluated by numerical quadrature of convergent continuum-continuum matrix element in Eq. (51).

Table II. Variation of close-coupled radiative scattering matrix element with coupling strength.

		$\Delta_{12} = 1.0\ cm^{-1}$			$\Delta_{12} = -50.0\ cm^{-1}$		
F_w(a)	a_{12}/cm^{-1}	$\lvert S_{12}^{rad}\rvert$	$\arg(S_{12}^{rad})$	$\frac{S_{12}^{rad}\Delta}{2\pi a_{12}}$	$\lvert S_{12}^{rad}\rvert$	$\arg(S_{12}^{rad})$	$\frac{S_{12}^{rad}\Delta}{2\pi a_{12}}$
1.0(-6)	1.67(-6)	3.4027(-6)	1.1641	0.32352	1.1979(-7)	2.1979	0.56947
1.0(-4)	1.67(-5)	3.4027(-5)	1.1641	0.32352	1.1979(-6)	2.1979	0.56947
1.0(-2)	1.67(-4)	3.4027(-4)	1.1641	0.32352	1.1979(-5)	2.1979	0.56947
1.0(+0)	1.67(-3)	3.4027(-3)	1.1641	0.32351	1.1979(-4)	2.1979	0.56947
1.0(+2)	1.67(-2)	3.4008(-2)	1.1641	0.32334	1.1979(-3)	2.1978	0.56466
1.0(+4)	1.67(-1)	3.2267(-1)	1.1643	0.30677	1.1978(-2)	2.1979	0.56941
1.0(+6)	1.67(+0)	9.7009(-1)	1.1646	0.09223	1.1928(-1)	2.1983	0.56704
1.0(+8)	1.67(+1)	7.8969(-1)	1.2013	0.00748	8.2868(-1)	2.2385	0.39441
1.0(+9)	5.29(+1)	2.1799(-1)	1.2487	0.00066	4.3899(-1)	2.6036	0.06599
1.0(+10)	1.67(+2)	1.1895(-3)	1.2410	0.00000	1.9301(-3)	0.1502	0.00009

(a) radiation flux in units of watts/cm^2. Using predicted transition dipoles for Sr+Ar this flux yields the listed radiative coupling coefficient a_{12}

Growth and Decomposition of Graphitic Structures

Principal Investigators: R. L. Brown and S. E. Stein

Introduction

Graphitic materials are the most commonly discussed laser-armor protective materials for spacecraft. Upon laser heating, the molecular structures in these materials decompose and reform, probably in both the vapor and condensed phases. At present there exists no molecular understanding of these chemical processes. This program intends to develop this understanding in order to assist both the rational analysis of laser-induced ablation processes as well as the development of improved protective materials.

The nature and reactivity of the chemical structures formed in these processes can control the effectiveness of laser protective materials in several ways. (1) The formation rate and nature of the volatiles produced may depend on both the nature and concentrations of precursor sites in the solid as well as on the reaction mechanism. (2) The chemical structure and reactivity of the materials remaining after ablation by the initial laser pulse will be determined largely by chemical factors. (3) The condensation of carbon vapors to form refractory particles may not be controlled by diffusion, but by chemical reaction, since reformed structures must form strong chemical links to resist re-evaporation.

The development of realistic working models for the above reactions requires a substantial increase in our understanding of the structure and reactivity of graphitic species. Our combined theoretical/experimental program focuses on the fundamental chemical properties of very large

polyaromatic structures. Graphite and nearly all carbonized organic materials are composed primarily of these structures.

Early in this program we discovered that the atomic orientation at the edges of these structures and their overall size were critically important factors in determining their reactivity. Our theoretical work has therefore been focused on separating and examining individually these two variables. Our experimental program is devoted to examining well defined carbon deposition reactions which can be connected with our theoretical work.

Progress During FY85

Theory

During this period we used the Pople self-consistent-field (SCF) molecular orbital theory to calculate orbital energy levels and pi-electron distributions of large hexagonal polyaromatic hydrocarbons. As in our previous work, four series of molecules, each with a different edge structure was considered. For molecules having an anthracene-like edge structure, SCF calculations predict that the pi-electrons in the highest occupied orbital (HOMO) will be concentrated at the perimeter of the molecule. These high level electrons are the ones most likely to become involved in reactions. This concentration of electron probability at the edges of the molecule is not limited to the highest level. It is evident in orbitals whose energies lie as much as 0.8 eV below the highest level. In contrast to these molecules are those with phenanthrene-like edges. For them, the electrons in these high orbitals are uniformly distributed over the whole molecule. Because of the large number of orbitals in these big molecules it was not feasible to examine the pi-electron distribution

in each orbital. Instead we calculated the average position of an electron in a particular orbital. From this, those orbitals having unusual electron distributions could easily be identified.

We next applied the simpler Huckel molecular orbital (HMO) theory in a systematic way to the molecules in our different homologous series. Like SCF calculations, HMO calculations yield orbital energies and wave functions for pi-electrons. From these, a number of molecular properties may be calculated. So far we have examined energy level densities, bond orders, electron distributions, free valence (a reactivity index) and resonance energies. Over thirty years ago, Coulson and Taylor [1] applied HMO theory to graphite considered as an infinite planar polybenzenoid molecule. They calculated the pi-electron energy per carbon, the density of states in the pi-electron bond, and pi-bond order. We have been able to compare our calculations of the properties for large finite-sized molecules with their limiting values for graphite.

The density of pi-state levels as a function of energy is shown in Figure 1 for a very large molecule having 2814 carbons and a phenanthrene type edge. The smooth curve shows the graphite limit calculated by Coulson and Taylor. The density fluctuations about the graphite limit observed at the lower energies are expected to damp out in larger molecules.

For a smaller molecule (1014 carbons) with this same edge type, Figure 2 shows how the pi-bond order varies as one moves from the center to the perimeter. Only the bond orders for bonds near the edges of the molecule differ appreciably from the graphite limit shown by the dotted line.

The orders of the bonds in the centers of our molecules are given in Figure 3 as a function of molecular size (Nc = number of carbons). They clearly extrapolate to the graphite limit in each of the different series.

Hess and Schaad [2] have proposed a resonance energy calculated as the difference between the Huckel pi-electron energy and that of a particular reference structure which they define. Figure 4 shows the resonance energies per carbon for each of these series as a function of molecular size. They all extrapolate to the graphite limit although the series containing anthracene type edges (series) experiences a deep minimum in resonance energy at about 400 carbons.

In graphite, the energy of the highest occupied molecular orbital is at the energy zero. For all of the series, the energies of the HOMO's extrapolate to zero. However, as shown in Figure 5, the rate of approach to this limit varies widely. Molecules with phananthrene type edges (series 3) have HOMO levels which are particularly slow to approach zero. Since the pi-electrons in these top levels are the ones most likely to be involved in chemical reactions, this suggests that molecules having edges of the phananthrene type would relatively non-reactive until they reached a very large size. A similar prediction regarding reactivity is shown in Figure 6 where the maximum free valence is plotted as a function of molecular size.

As in the SCF results, these variations between the HOMO's of the different series are also quite evident in the pi-electron distributions. In the more reactive anthracene edge series, electrons in this top level are concentrated around the molecular perimeter, while in the pharanthrene edge series these electrons are distributed uniformly over the whole molecule. This is shown in Figures 7 and 8 for molecules of comparable

size having these edge types. In the anthracene edge type, this concentration of electron density at the edge is not restricted to the top level only but extends downward some seven or so levels.

Of all the theoretical methods that we have examined, HMO provides the most satisfactory all-around approach to the calculation of a number of properties of large polyaromatic molecules. It has been quite successful in predicting electronic properties of small benzenoid molecules. With an appropriate choice of adjustable parameters, Hess and Schaad have shown that it can yield very accurate predictions of aromaticity [2] and heats of formation [3] for a variety of compounds. These workers did not include graphite or steric interactions in their parameterization scheme. Preliminary work by us has indicated that their inclusion will improve the accuracy of the HMO method. Because HMO predictions extrapolate to the correct graphite limits, we feel that this theory will also accurately predict properties of intermediate sized polybenzenoid molecules. Consequently, it promises to be a significant aid in devising models for reactions of carbonaceous substances.

Experimental

We have examined the kinetics of phenyl radical ( ) deposition on pyrolytic graphite surfaces. These radicals were generated by the thermal decomposition of nitrosobenzene, C_6H_5-NO, in a very low pressure flow reactor. The pyrolytic graphite was formed by the deposition reaction itself on the fused silica reactor surface. The key result of these experiments is that the probability of deposition per molecule depends on the square root of the concentration of radicals. This is interpreted as resulting from an increase in surface active sites with

increasing deposition rate. Specifically, assuming that the probability for deposition per collision with a reactive site is constant, the density of reactive sites is proportional to the square root of phenyl radical concentration.

The probability of deposition per collision was of the order of 1/100 to 1/1000 per collision in our experiments. This suggests that the exposed pyrolytic graphite surface is quite reactive and probably disordered: this is in sharp contrast to the known crystallographic regularity of bulk pyrolytic graphite.

Several potentially reactive hydrocarbon molecules have been examined for their surface reactivity in our reactor. Unfortunately, we have not found one that underwent significant deposition over our currently accessible temperature range (<1300K). It is now clear that to examine deposition kinetics in detail, we will have to modify our apparatus to enable operation at significantly higher temperatures (i.e., above the melting point of fused silica). Modifications are in progress.

References

1. C. A. Coulson and R. Taylor, Proc. Roy. Soc. A., 65, 815 (1952).

2. B. A. Hess, Jr. and L. J. Schaad, J. Amer. Chem. Soc., 93, 2413 (1971).

3. L. J. Schaad and B. A. Hess, Jr., J. Amer. Chem. Soc., 94, 3068 (1972).

Figure Captions

Figure 1. Density of HMO orbital energy levels as a function of energy for molecule with 2814 carbons and a phenanthrene edge type. The smooth curve shows the graphite limit.

Figure 2. Variation of pi-bond order throughout a molecule with 1014 carbons and phenanthrene type edge. Dotted line shows graphite value.

Figure 3. Bond orders of bonds in centers of molecules in different homologous series as a function of molecular size. Dotted line shows graphite limit.

Figure 4. Resonance energies per carbon as a function of molecular size. Dotted line shows graphite limit.

Figure 5. Energy of highest occupied molecular orbital as a function of molecular size.

Figure 6. Maximum free valence as a function of molecular size.

Figure 7. Electron probability distribution of highest occupied molecular orbital in a molecule with anthracene edge type.

Figure 8. Electron probability distribution of highest occupied molecular obital in a molecule with phenanthrene edge type.

Publications and Presentations

1. S. E. Stein, L. L. Griffith, M. Manka and R. L. Brown, "Chemical Fundamentals of Coal Char Formation", ACS Fuel, Div. Preprints, 29 (2), 42 (1984).

2. S. E. Stein, R. L. Brown and A. Greenberg, "Relative Thermochemical Stabilities and Reactivities of Benso(a)pyrene and Related Isomers", Chemistry of the Total Environment, 40, 219 (1984).

3. S. E. Stein and R. L. Brown, Carbon, 23 (1), 105 (1985).

4. S. E. Stein and R. L. Brown, "Pathways to Graphite: Properties of Very Large Polynuclear Aromatic Hydrocarbons", in Molecular Structures and Energetics, Liebman and Greenberg, eds. Pergamon Press (in press).

5. R. L. Brown, "Application of SCF Theory to Very Large Polyaromatic Molecules", NBS Internal Report (in press).

6. "A Chemical Theory of Graphite", presented at West Virginia University, Morgantown, West Virginia, April 1985.

7. "A Chemical Theory of Graphite", presented at Catholic University of America, Washington, D.C., April 1985.

8. "A Chemical Theory of Graphite", presented at the "17th International Carbon Conference", Lexington, Kentucky, June 1985.

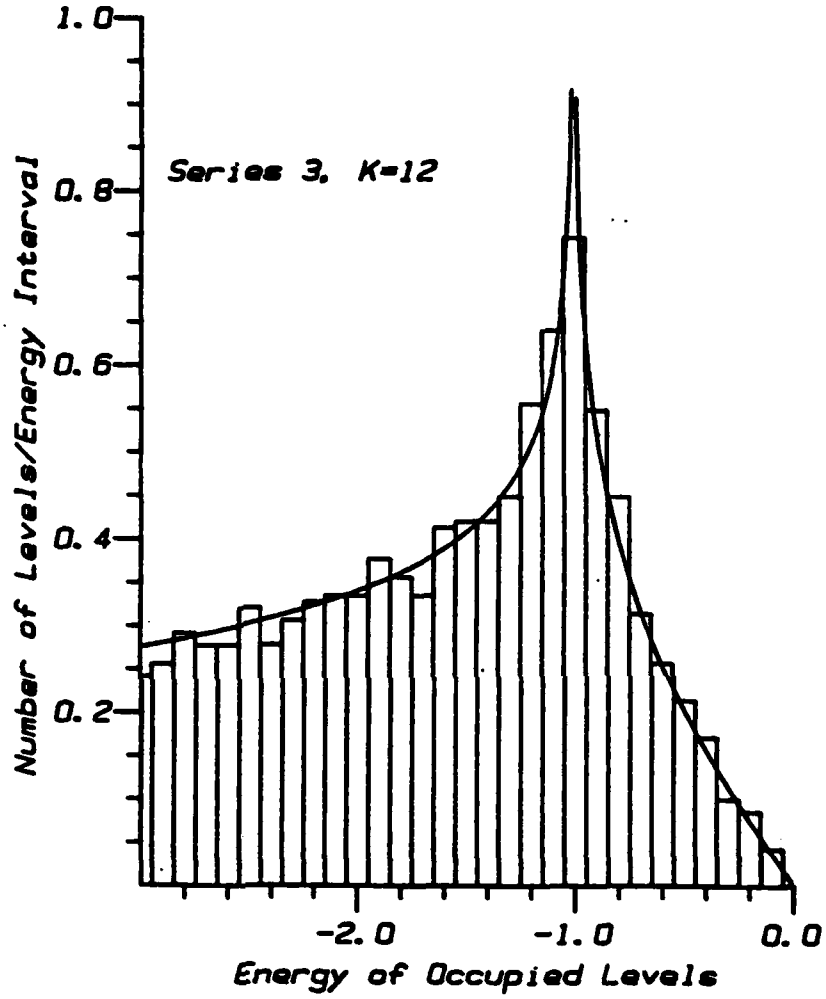

Figure 1. Density of HMO orbital energy levels as a function of energy for molecule with 2814 carbons and a phenanthrene edge type. The smooth curve shows the graphite limit.

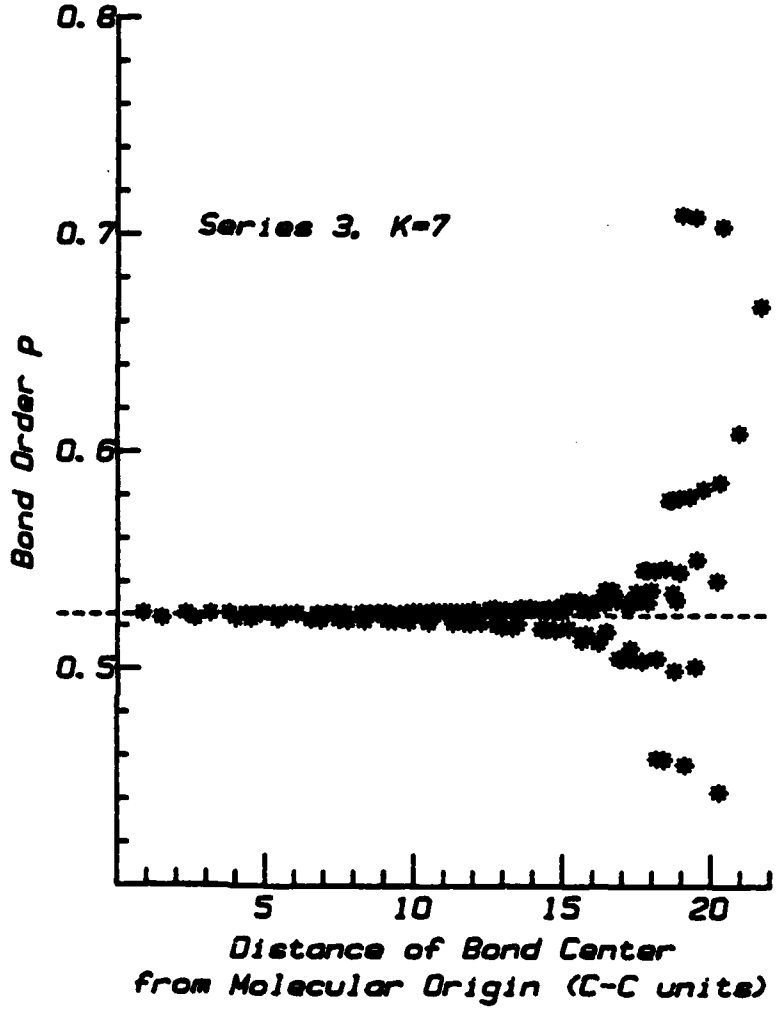

Figure 2. Variation of pi-bond order throughout a molecule with 1014 carbons and phenanthrene type edge. Dotted line shows graphite value.

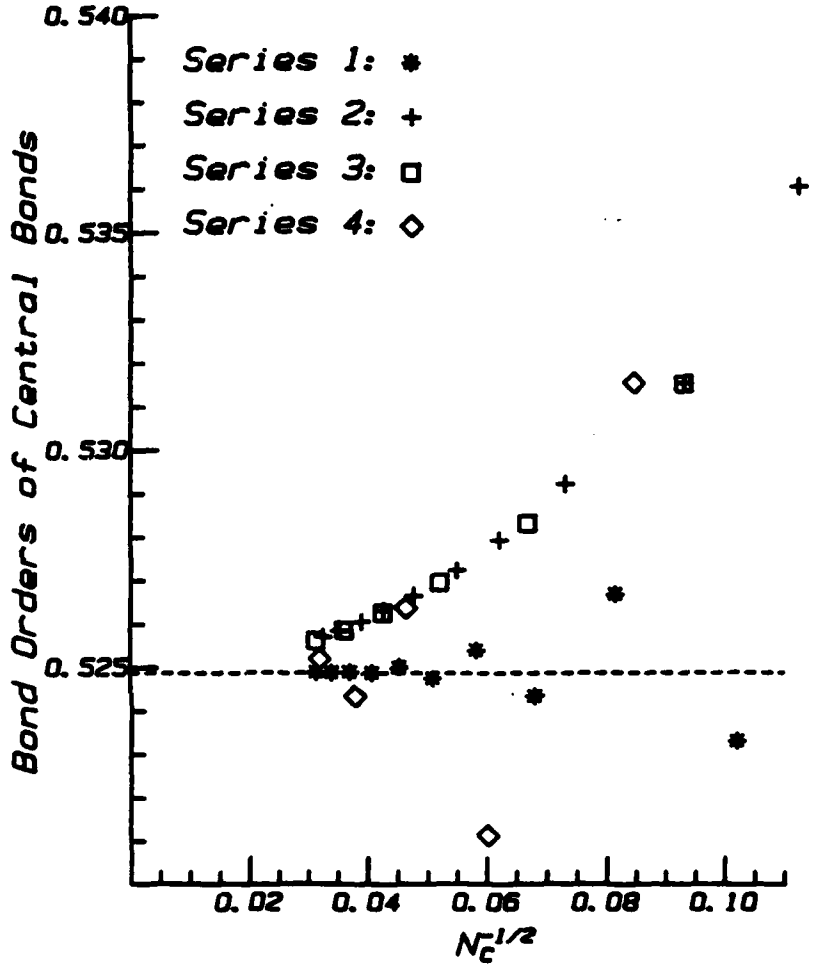

Figure 3. Bond orders of bonds in centers of molecules in different homologous series as a function of molecular size. Dotted line shows graphite limit.

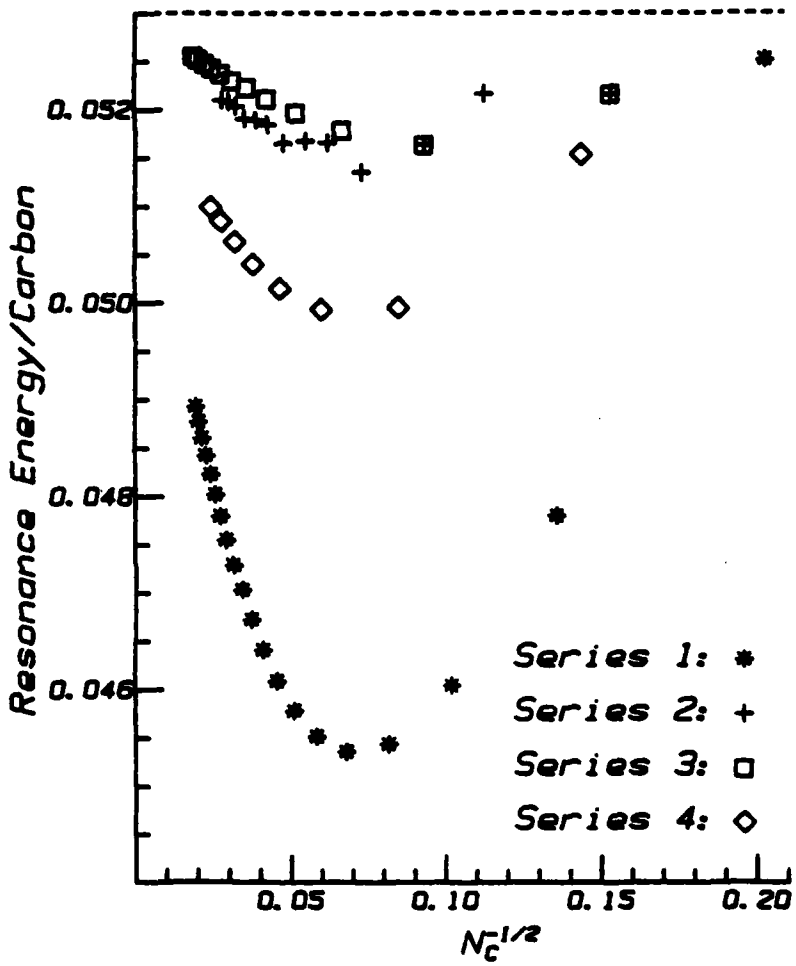

Figure 4. Resonance energies per carbon as a function of molecular size. Dotted line shows graphite limit.

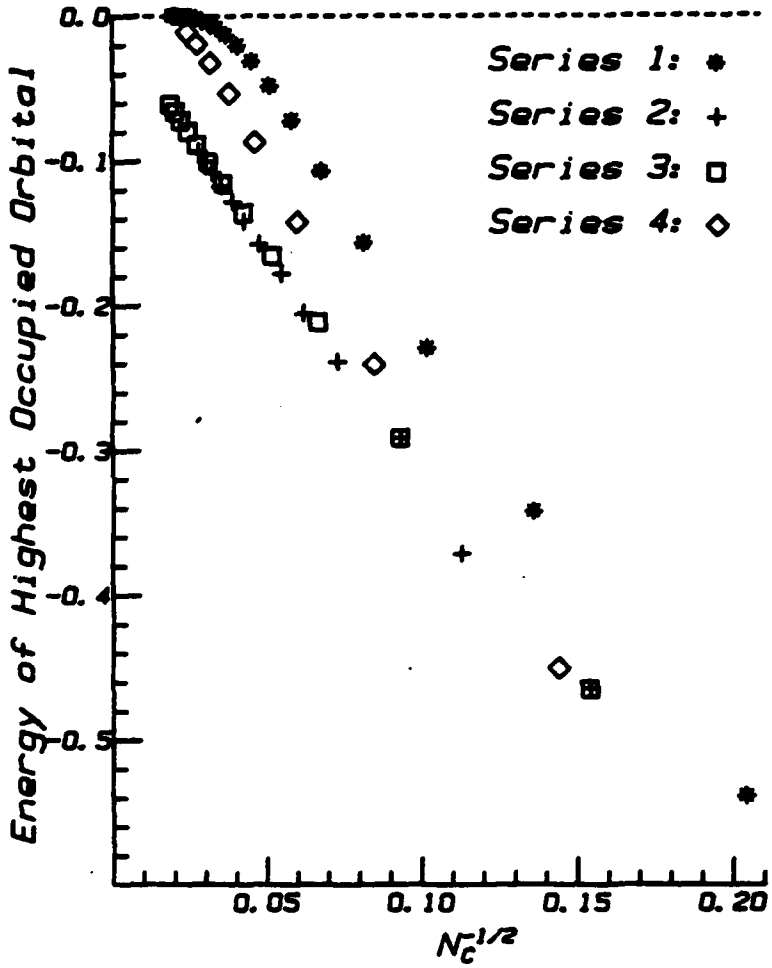

Figure 5. Energy of highest occupied molecular orbital as a function of molecular size.

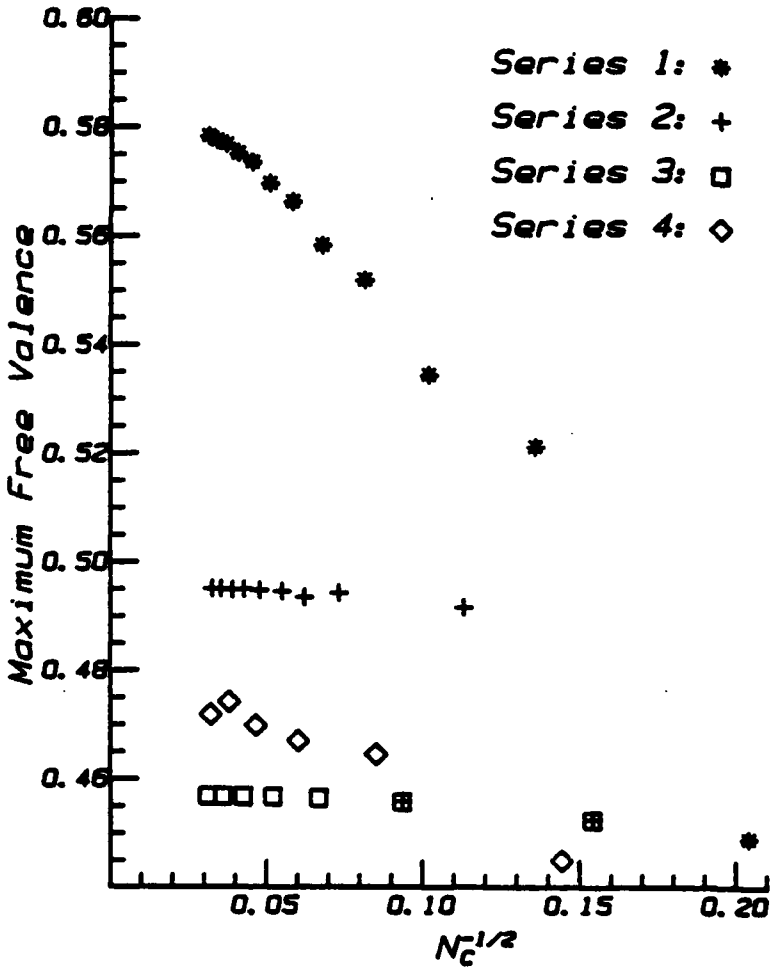

Figure 6. Maximum free valence as a function of molecular size.

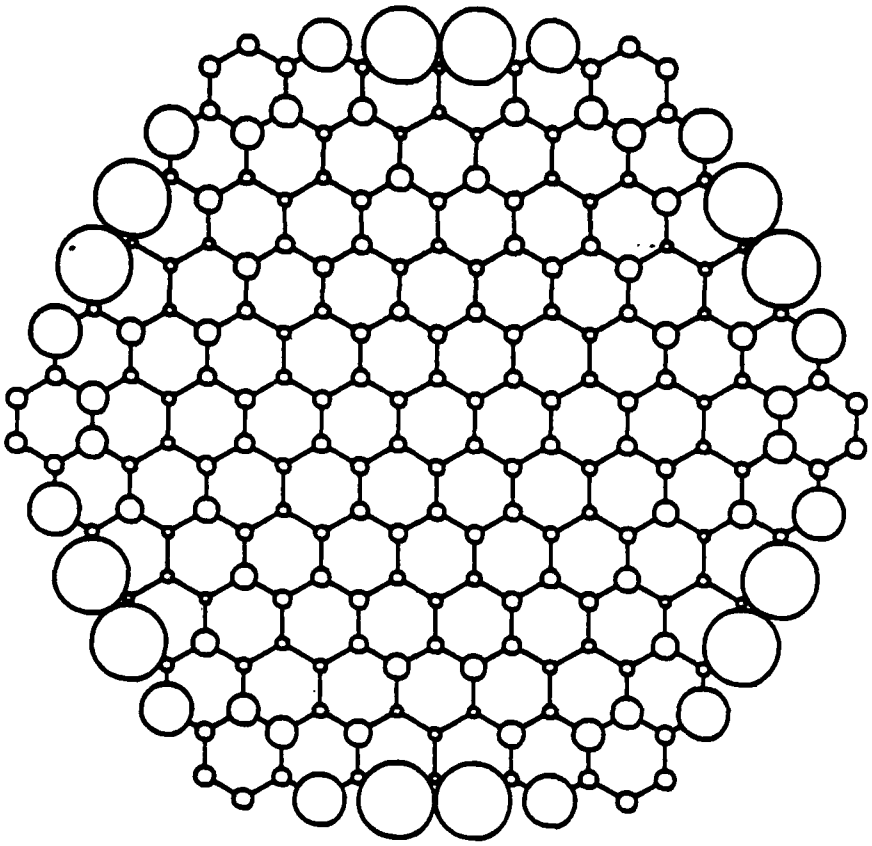

Figure 7. Electron probability distribution of highest occupied molecular orbital in a molecule with anthracene edge type.

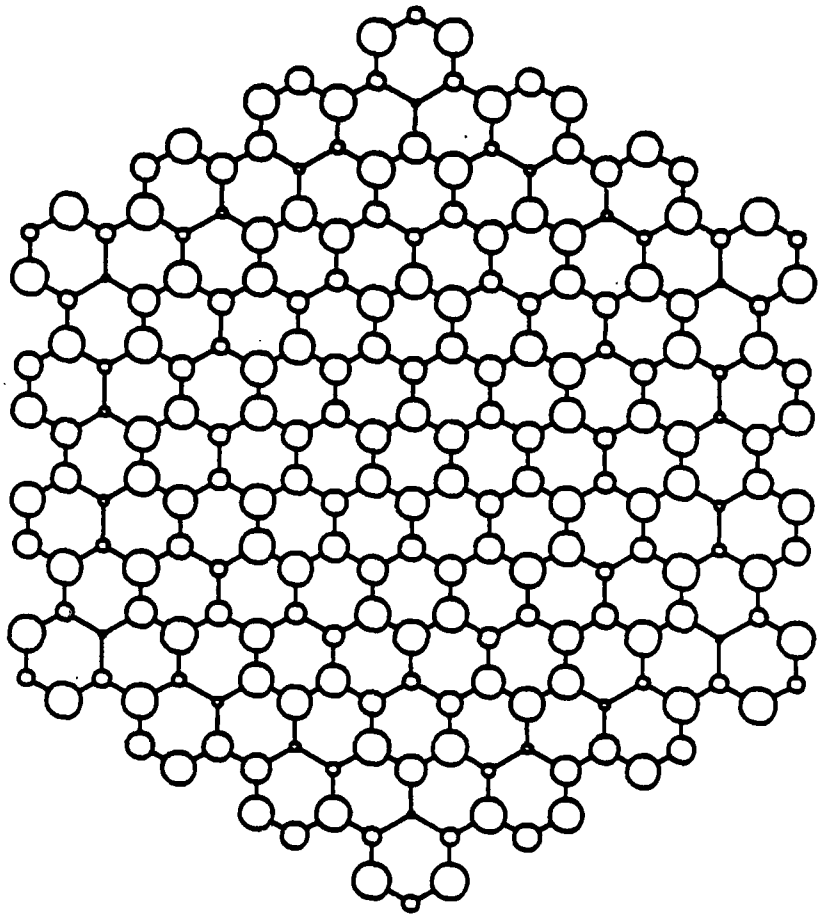

Figure 8. Electron probability distribution of highest occupied molecular obital in a molecule with phenanthrene edge type.

BUILD-UP AND IRRADIATION OF OBSCURING CLOUDS UNDER NEAR-VACUUM CONDITIONS: APPLICATION TO SPACECRAFT SURVIVABILITY

Principal Investigators: Thomas J. Buckley
Sharon G. Lias

Annual Report
FY 1985

This project concentrates on the elucidation of the rates and mechanisms of ionic polymerization mechanisms in highly unsaturated organic compounds, the structures and thermochemistry of relevant ions, the photodissociation of the polymeric ions, and the repair mechanisms which regenerated the polymeric ions after photodissociation. Positive ions generated in a pulsed ion cyclotron resonance spectrometer undergo rapid polymerization with surrounding neutral molecules (which can be identified with molecules vaporized from a graphitic material at the surface of a spacecraft). In the kinetic mass spectrometers available for this project it is possible to reproduce some of the conditions which would prevail near the surface of a spacecraft both in terms of gas pressure and composition, and in terms of impinging natural electromagnetic and laser radiation.

In investigations of the generation and dispersal of smokes and obscuring materials in space, the kinetics of evaporation of refractory materials under laser irradiation, and condensation processes leading to the formation of microscopic particles, graphitic materials and polyarylacetylenic polymers are of particular interest. Therefore, the work completed during FY85 focussed primarily on the elucidation of the gas phase polymerization and reaction mechanisms following laser-irradiation induced breakdown in aromatic hydrocarbons, particularly those with acetylenic and olefinic side chains such as phenylacetylene and phenylethylene (styrene). In addition, the kinetics and mechanisms of the reactions of phenyl ions were examined, and

structures of $C_6H_5^+$ ions generated from a number of organic molecules have been elucidated.

Phenylacetylene

The ion-molecule chemistry in the phenylacetylene system has never before been investigated. Our experiments showed that the predominant reactions of the parent ion with the phenylacetylene molecule are:

	k_{Rn} cm^3/molecule-sec $x10^{10}$
$C_8H_6^+ + C_6H_5C{\equiv}CH \rightarrow$ Products	9.1 $\pm$0.5
$\rightarrow C_{16}H_{12}^+$	
$\rightarrow C_{16}H_{11}^+ + H$	
$\rightarrow C_{16}H_{10}^+ + H_2$	
$\rightarrow C_{14}H_{10}^+ + C_2H_2$	

Irradiation of these product ions with 514.5 nm (2 eV) photons results in the following photodissociation processes:

$$C_6H_{12}^+ + h\nu \rightarrow C_8H_6^+ + C_8H_6$$
$$\rightarrow C_{16}H_{10}^+ + H_2$$

$$C_{16}H_{10}^+ + h\nu \rightarrow C_{16}H_8^+ + H_2$$

$$C_{16}H_{11}^+ + h\nu \rightarrow C_{16}H_{10}^+ + H$$

The dimer ion, $C_{16}H_{12}^+$, and the photogragment, $C_{16}H_{10}^+$, react with phenylacetylene with rate constants of 3.2×10^{-11} and 3.1×10^{-11} cm^3/molecule-s, respectively, to form "trimeric" ions, $C_{24}H_{18}^+$ and $C_{24}H_{16}^+$.

The fragment ions formed by dissociation of excited parent ions also react with phenylacetylene. The following rate constants were determined:

	k_{Rn} cm^3/molecule-sec $x10^{10}$
$C_6H_4^+ + C_6H_5C{\equiv}CH \rightarrow C_{12}H_8^+ + C_2H_2$	12.4 $\pm$1.4
$C_6H_3^+ + C_6H_5C{\equiv}CH \rightarrow$ Products	12.2 $\pm$1.2
$C_6H_2^+ + C_6H_5C{\equiv}CH \rightarrow$ Products	21.1 $\pm$2.3

$C_4H_4^+ + C_6H_5C{\equiv}CH \rightarrow$ Products	11.4 $\pm$1.8
$C_4H_3^+ + C_6H_5C{\equiv}CH \rightarrow$ Products	13.9 $\pm$0.8
$C_4H_2^+ + C_6H_5C{\equiv}CH \rightarrow$ Products	22.9 $\pm$4.3

That is, many of the types of reaction observed in our earlier study of ionic reactions in diacetylene are observed, namely that the highly unsaturated ions (i.e. $C_6H_2^+$ and $C_4H_2^+$) react at every collision with the precursor acetylenic molecule, and that efficient condensation reactions occur followed by elimination of a molecule of acetylene.

Because the details of such ion-molecule polymerization and polymerization/dissociation mechanisms are largely controlled by thermodynamic parameters, experiments are also carried out to elucidate the thermodynamics of the ionic mechanisms in these systems. Proton transfer reactions are ubiquitous in such systems, and therefore determinations of the proton affinities of the parent molecules are useful in understanding the overall reaction mechanisms. The proton affinity of phenylacetylene was determined through "bracketing" experiments in which a series of bases, for which the thermodynamic parameters associated with proton donation are well established:

$$BH^+ + C_6H_5C{=}CH \rightarrow C_8H_7^+ + B$$

The results were as follows:

M	B	Proton affinity(B) kcal/mol	Proton Transfer Observed?
$C_6H_5C{\equiv}CH$	$i\text{-}C_3H_7COOCH_3$	201.6	No
	$(C_2H_5)_2CO$	201.4	No
	$(C_2H_5)_2O$	200.2	Yes
	$C_2H_5COOCH_3$	200.2	Yes

The bracketing experiments lead to a value for the proton affinity of phenylacetylene of 200.7$\pm$0.5 kcal/mol.

AD-A164 253 THERMODYNAMICS OF HIGH TEMPERATURE MATERIALS(U) 2/2
NATIONAL BUREAU OF STANDARDS GAITHERSBURG MD
S ABRAMOWITZ 24 DEC 85 AFOSR-TR-86-0008
UNCLASSIFIED AFOSR-85-ISSA-00029 F/G 11/2 NL

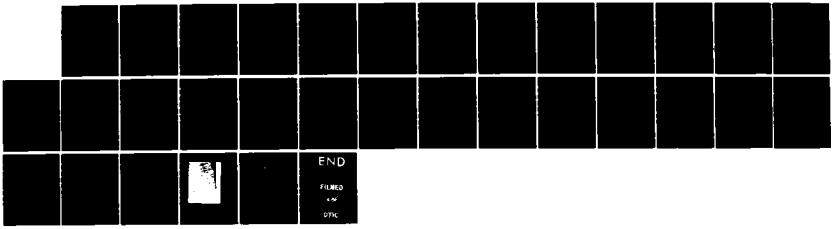

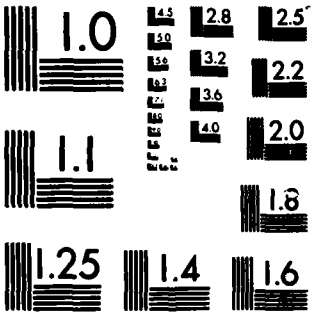

MICROCOPY RESOLUTION TEST CHART

NATIONAL BUREAU OF STANDARDS-1963-A

Phenylethylene (Styrene)

Previous studies of ionic processes in styrene reported the occurrence of the processes:

$$C_8H_8^+ + C_8H_8 \rightarrow C_{16}H_{16}^+$$
$$\rightarrow C_{10}H_{10}^+ + C_6H_6$$

but no kinetic data were reported. In the reinvestigation of the system, we determined the rate constants and reaction mechanisms for the reactions of $C_8H_8^+$ and the fragment ions in order to infer information about the structures and thermochemistry of these fragment ions and their condensation products. The following reactions were observed:

		k_{Rn} cm^3/molecule-sec $\times 10^{10}$
$C_8H_8^+ + C_6H_5CH{=}CH_2$	-> Products -> $C_{16}H_{16}^+$ -> $C_{10}H_{10}^+ + C_6H_6$ -> $C_9H_9^+ + C_7H_7$	0.65 ± 0.02
$C_8H_7^+ + C_6H_5CH{=}CH_2$	-> Products	1.7 ± 0.2
$C_6H_6^+ + C_6H_5CH{=}CH_2$	-> Products	15.0 ± 0.8
$C_6H_5^+ + C_6H_5CH{=}CH_2$	-> Products	9.1 ± 1.0
$C_5H_3^+ + C_6H_5CH{=}CH_2$	-> Products	3.8 ± 1.1
$C_4H_3^+ + C_6H_5CH{=}CH_2$	-> Products	13.9 ± 1.2

Irradiation of the system with the 514.8 nm laser line led to the dissociation of the two major product ions:

$$C_{16}H_{16}^+ + h\nu \rightarrow C_8H_8^+ + C_8H_8$$
$$C_{10}H_{10}^+ + h\nu \rightarrow C_{10}H_8^+ + H_2$$

Experiments designed to elucidate the structures of the $C_{10}H_{10}^+$ and $C_{10}H_8^+$ ions were carried out. It was reported in a 1971 study of the dimerization process in styrene that the $C_{16}H_{16}^+$ ion had the structure:

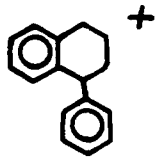

Thus, dissociation of this ion by loss of a benzene molecule might be expected to lead to the formation of a $C_{10}H_{10}^+$ species with a structure such as:

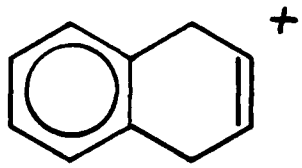

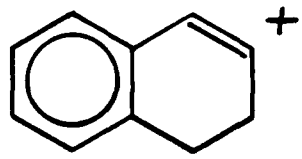

In order to test this possibility, the kinetics and photodissociation mechanisms of the parent ions formed in 1,2- and 1,4-dihydronaphthalene were examined; it was concluded that these ions do behave like the $C_{10}H_{10}^+$ ion generated in styrene, thus providing evidence that the structures given above do correspond to the species formed in phenylacetylene.

The proton affinity of styrene was also determined through "bracketing" experiments like those described above for phenylacetylene.

$$BH^+ + C_6H_5CH{=}CH_2 \rightarrow C_8H_9^+ + B$$

The results, summarized below, indicate that the proton affinity of styrene is 202.1±0.5 kcal/mol.

	B	Proton Affinity kcal/mol	Proton transfer observed?
$C_6H_5CH{=}CH_2$	$(n\text{-}C_3H_7)_2O$	202.3	No
	$i\text{-}C_3H_7COOCH_3$	201.6	Yes
	$(C_2H_5)_2CO$	201.4	Yes
	$(C_2H_5)_2O$	200.2	Yes
	$C_2H_5COOCH_3$	200.2	Yes

Structure and Reactivity of $C_6H_5^+$ Ions

Although collision-induced dissociation (CID) studies have examined the structures of $C_6H_5^+$ ions formed as fragments in the electron impact ionization of organic molecules and as products of ion-molecule reactions, there is still conflicting evidence about the identities of these ions, which are generated in the dissociation of the parent ions of aromatic molecules:

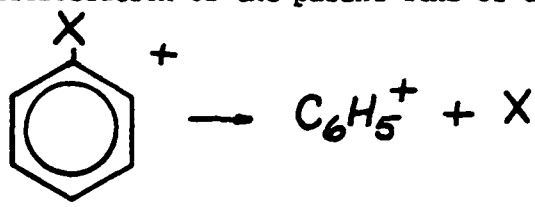

Also, to date no comprehensive examination of the kinetics of the reactions of these ions has been made.

A study was made of the structures and reactivities of $C_6H_5^+$ ions using the ion cyclotron resonance spectrometer. In many systems (fragment ions formed in the halobenzenes, or the $C_6H_5^+$ formed as a result of consecutive ionic condensation reactions in acetylene, for example) at least two populations of $C_6H_5^+$ can be discerned, one which is highly reactive and one which is relatively unreactive with the precursor molecules. The identities of these populations were sorted out by generating $C_6H_5^+$ ions under energy conditions such that only the phenyl ion could be present, i.e. photodissociation of $C_6H_5Cl^+$ via a two-photon process at 514.5 nm must lead exclusively to the formation of $C_6H_5^+$ ions having the phenyl ion structure, since there is insufficient energy for ring opening to occur. In this way it was demonstrated that the more reactive isomer is the phenyl ion, contrary to assumptions made in previous studies. It can be concluded that the $C_6H_5^+$ ions formed as products in chemical reactions:

$$C_4H_3^+ + C_2H_2 \rightarrow C_6H_5^+$$

or

$$C_3H_3^+ + C_3H_3Br \rightarrow C_6H_5^+ + HBr$$

exhibit more acyclic character the higher the energy content of the $C_6H_5^+$ ion produced in the reaction.

The phenyl ions react with saturated hydrocarbons to form a complex which may dissociate to form benzene and/or protonated benzene. Even through these processes are generally highly exothermic, the reaction rate constants are approximately a factor of ten lower than the corresponding ion-molecule collision rate constants. Factors controlling the rate constants and reaction channels of $C_6H_5^+$ ions interacting with organic and inorganic molecules are being explored further. In experiments utilizing partial deuterium labelling, it has been seen that the phenyl ion exhibits no selectivity in the hydride transfer reaction:

$$C_6H_5^+ + (CH_3)_3CD \rightarrow C_6H_5(H,D) + C_4(H,D)_9^+$$

References

Work Supported by AFOSR Which Appeared in 1985:

T. J. Buckley, L. W. Sieck, R. Metz, S. G. Lias, J. F. Liebman, "Consecutive Ion-Molecule Condensation Reactions and Photodissociation Mechanisms of Condensation Ions in Polyacetylenic Compounds," Int. J. Mass Spectrom. Ion Proc. 65, 181 (1985).

S. G. Lias and P. Ausloos, "Structures of $C_6H_7^+$ Ions Formed in Unimolecular and Bimolecular Reactions," J. Chem. Phys. 82, 3613 (1985).

Submitted for Publication:

C. A. Deakyne, M. Meot-Ner (Mautner), T. J. Buckley, and R. Metz, "Proton Affinities of HCCCCH, HCCCN, and NCCN: Experimental and Ab Initio Studies," J. Chem. Phys.

In Preparation:

S. G. Lias, P. Ausloos, and T. J. Buckley, "On the Structure and Reactivity of $C_6H_5^+$ Ions"

T. J. Buckley, Z. Karpas, and S. G. Lias, "Ion-Molecule Reactions and Photodissociation Mechanisms in Styrene and Phenylacetylene"

MOLECULAR BASIS FOR LASER-INDUCED VAPORIZATION OF REFRACTORY MATERIALS

J.W. Hastie, D.W. Bonnell, and P.K. Schenck
High Temperature Chemistry Group
Ceramics Division
Institute for Materials Science and Engineering
National Bureau of Standards

I. INTRODUCTION

The objective of this project is to develop a molecular-level understanding of the vaporization and related ionization and aggregation processes which occur when high-power laser energy is dissipated in carbon-containing materials. These highly complex processes can be expected to include the thermodynamically controlled production of C_n ($n \approx 1 - 10$) molecular species, and the non-equilibrium production of higher cluster species ($n \sim 10 - 1000$), in adition to the formation of electrons, and positive and negative ions. Inorganic carbon-based materials, such as graphite, metal carbides, and carbon-carbon composites, have intrinsically high resistance to thermal degradation. This behavior results from an inherently high sublimation energy, high melting point, and high thermal conductivity. The development of effective laser-resistant materials and obscurants is expected to rely mainly upon such carbon-based materials [Baker and Hager, 1984; Stickley, 1985].

Despite considerable research over the past several decades, the basic thermodynamic, kinetic, and mechanistic description of the thermal decomposition of graphite and related materials is still in considerable doubt. In fact, two widely used but discrepant sets of thermodynamic tables exist for the carbon vapor species, the JANAF [1971-82] thermochemical tables and the so-called Livermore tables [cf. Baker, et al, 1983]. Even the melting point of graphite is a subject of considerable controversy. Experiments have been conducted on the effect of moderate power CO_2 and

Nd-YAG lasers on the vaporization of various forms of graphite [Covington, et al, 1977; Kirillin, et al, 1984; Lincoln and Covington, 1975; Lundell and Dickey, 1977; Lundell, 1982; Meyer, et al,1973; Milne, et al, 1972; Scheindlin, 1984; Zavitsanos, 1968]. Most of these studies have concentrated on the macroscopic, non-molecular processes such as crater formation, material removal rate, plume dynamics, and phase equilibria. We have reviewed the recent literature [Hastie, et al, 1984] and find that there is considerable disparity, particularly concerning relative and absolute partial pressures of the various carbon polymer species.

The work reported here has utilized a very high pumping speed mass spectrometer system, with a Nd/YAG laser providing the vaporizing heat source. Special emphasis has been given to the relationship of the C_n species partial pressures to laser parameters such as fluence, irradiation angle, and impact repetition.

II. EXPERIMENTAL APPARATUS AND PROCEDURE

Installation of a new 20 Hz Nd-YAG laser system, and its coupling to the high pressure sampling Mass Spectrometer (MS), was recently completed. The experimental setup is otherwise similar to that reported previously [Hastie, et al, 1984], and is shown schematically in figure 1. The salient feature of the sample mount region is the very high pumping speed, exceeding 2000 l/sec at pressure up to 10^{-5} atm (1 atm = 101325 Pa).

The laser system operates at wavelengths of 355, 532, or 1064 nm with energies up to 200 mJ per pulse at 1064 nm. The present studies utilized 532 nm as this wavelength provided the best match of energy and vaporization conditions (10-40 mJ into a 250 um spot). For physical access, the beam is periscoped to the level of the sample and then piped to a motor-driven 500 mm focusing lens via dielectric mirrors which are housed in a nitrogen-purged

9 x 12 cm conduit (not shown in figure 1). A radiometer was used to directly measure the laser fluence, characterize the transmission losses of the beam through the conduit system, and calibrate lamp power to delivered laser power. Radiometric measurements were made periodically during experimental runs to confirm constant laser power conditions.

Alignment of the laser impact point with the mass spectrometer beam-acceptance axis was monitored using a photodiode located just above the mass filter ion source. Optimum alignment was obtained by adjusting the final laser mirror to maximize the intensity of the reflected laser light from the sample surface. This technique was shown, using a He/Ne laser and mirror, to provide accurate positioning of the laser impact point at the center of the molecular beam acceptance cone of the MS system. Because of the extreme forward-peaking of the emitted molecular beam, the acceptance angle of the beam system was set at about 13°, with a usable targeting point radius about the nominal beam center origin of ~0.3 cm. From an inspection of the deposit patterns on the beam wall directly above the sample point, the beam distribution appeared to be much more collimated than COS^2 (typical of effusion) due to the beam self-focusing. The beam centerline emission angle was observed to be within ~± 2° of normal to the surface with the sample angle at 15° from the horizontal laser beam. Both forward-peaking and normal beam emission were independent of laser-sample angle and of whether individual laser shots always struck a fresh surface, or up to 18,000 shots were allowed to impact the same spot.

Most of the recent experiments used high density/high purity graphite of similar overall purity to the spectroscopic grade graphite used previously. The primary reason for changing the specimen source was to obtain a larger sample cross section (~5.6 cm). Specimens 0.24 cm thick were parted from a

large bar with a carefully cleaned steel cutting tool. The polishing step was omitted to eliminate possible contamination by silicon carbide, even though this did not appear to be a problem in our earlier studies. The surface roughness of the present samples was only slightly greater than that of the lightly polished spectroscopic grade material used earlier. A mass spectral survey indicated no contaminant peaks other than those noted for the spectroscopic rod source (i.e., only minor hydrocarbon content).

The experimental data acquisition process consisted of the following steps:

1. Position sample to the limit position of the translator, adjust beam position and focus.
2. Position sample to location of interest.
3. Tune mass filter to mass of interest.
4. Open laser shutter, letting pulses strike surface.
5. Collect ion signal during the ~ 5ms time period which follows each pulse using a signal averager with 1024 data sampling points. Between 100 and 1000 shots were generally averaged to obtain good signal-to-noise.
6. (a) For the static mode, successive laser shots impact the same location.

   (b) For the dynamic mode, the sample is moved after every shot. The maximum movement was about 10μm between shots.
7. Repeat steps 2-6 for each mass position of interest.

This procedure produces mass selected profiles of ion intensity versus time, as shown by the C_1^+ example given in figure 1. The time scale includes the laser on/off pulse (10 ns), together with the much longer (millisecond) times for sample cooling and beam transit to the mass spectrometer. Earlier work

[Hastie et al, 1984] indicated that these profiles contain data on neutral species flight times and hence post-expansion vapor temperature, in addition to the surface thermal history. However, the earlier use of multiple laser shots at each location produced species intensities which apparently corresponded to unit accomodation coefficient due to the formation of a crater which could behave as a crude Knudsen cell. With successive laser shots at a fixed location, signal intensities decreased roughly in proportion to the logarithm of the number of shots. We interpreted this effect as being due to crater formation causing an enhanced forward-beam peaking, with a consequent loss of signal off the beam centerline.

During this reporting period, we have devised and installed a two axis translation system. Operating under real-time control with in-house developed code, this system allows samples to be positioned or rastered, as desired, between laser shots. The system permits positioning over a square area 2.5 cm on a side. Raster rates up to 200 μm/sec are possible, corresponding to somewhat over 90 percent shot-to-shot overlap with a ~250μ beam spot dimension. With this new raster system, it is now possible to monitor the vaporization process continuously, from the pristine surface condition to the cratered condition of our earlier work.

III. RESULTS AND DISCUSSION

Experiments were carried out during this reporting period to examine in greater detail the special features noted earlier for the vaporization of graphite. In particular, the observation of thermodynamic equilibrium at nearly unit accomodation coefficient from cratered surfaces was tested by operating in the raster mode, where each shot was directed at a fresh surface. The earlier observation of anomalously high C_1/C_3 ratios, attributed to non-thermal sources, was also reexamined.

III.1 Scanning Versus Static Laser-Surface Interaction

Our initial mass spectral observations showed a decreasing vaporization rate with increasing number of laser shots at a fixed surface location. The effect of laser-induced vaporization from a fresh, non-cratered surface was examined by scanning the laser beam across the sample surface. Thus each sample location received only a small (~20-25) number of laser shots. Figure 2 shows the effect of systematically varying the number of laser shots on the mass spectral ion intensities for C_n^+ (n = 1 - 5). Note that the rate of decrease in signal (normalized with respect to the number of laser shots) with number of laser pulses is considerably more pronounced for C_1^+ and C_2^+ than for C_4^+ and C_5^+. The higher mass species intensites are essentially constant, within error limits, particularly after only a few thousand shots. These observations suggest that during the early stages of vaporization, under continuous laser irradiation, the lower mass C_n species may indeed predominate. This effect could account for the disparate literature results on the relative abundance of the various C_n species (e.g., see Clarke and Fox, [1969]; Wachi and Gilmartin [1970]). Wachi and Gilmartin [1970] reported a similar effect, with C_3 increasing strongly relative to C_1 and C_2 over time, which they attributed to changes in surface morphology and/or the possible formation of a carbon allotrope. Section III.5 discusses our surface analysis results.

Table 1 shows a comparison of the present laser-scanned results with the earlier [Hastie, et al, 1984] static data. Note that the species ratios are in reasonable agreement between the two cases, except for C_1 and the reason for this is currently under investigation (see section III.5). The slightly lower value for C_5 is unexpected and may result from an instrumental effect

on peak widths. This peak width reproducibility problem is under investigation, but is probably caused by insufficient bandwidth in the data collection process (see section III.3). The direct observation of C_6 - C_9 reflects the improvement in sensitivity we have accomplished with the new experimental arrangement. C_9 currently represents our detection limits, with signal/noise ratios of about 1. A significant improvement in signal-to-noise can be expected when we convert to signal counting detection techniques (see section III.3 below).

III.2 Evidence for Local Thermodynamic Equilibrium

In the previous static experiments [Hastie, et al, 1984], it was noted that the various carbon polymer species appeared to be generated with a common source (sample surface) temperature, T. Regardless of the exact model for the vaporization and beam-forming process, if a collection of gas molecules are in thermal equilibrium, their velocity function is proportional to $(T_o/M)^{1/2}$, where M is the individual species molecular weight and T_o is the gas temperature. Hence a plot of time-of-arrival, Δt (which is inversely proportional to velocity) versus $(M)^{1/2}$ should show a linear correlation for thermal equilibrium conditions. Figure 3 shows the peak (most probable) arrival time of carbon polymer species up to C_5 for three ranges of accumulated laser shot conditions. Within repeatability, the expected linear relation is found. The outlier of C_4 at 14,000 shots in this particular data set also showed an anomalously wide intensity-time profile which was not reproduced in other experimental series.

III.3 Relative Temperatures and Instrumental Response

In order to obtain good time resolution, the signal averaging has been performed by collecting the amplified multiplier output current (analog) of the MS. The analog signal is then digitized by a fast 8 bit digitizer in the

multichannel analyzer (MCA) and accumulated in individual channels. This process results in imposing the final DC amplifier risetime function (with a time-constant of the order of a few kHz) on the intensity profiles, as well as subjecting low level signals to "noise" caused by digitizer granularity. A more desirable method would be to use the electron multiplier in the saturated mode, and count individual ion events. The currently available MCA has unacceptable dead time requirements in its multichannel scaler mode at minimum channel dwell time (~5 μs/channel). It should be noted that the channel time is already a compromise and should be faster, by about an order of magnitude, for optimum resolution of the temperature information.

To improve the signal detection time constant, we decreased the DC gain by a factor of 100, by changing the amplifier load resistor from 10^7 Ω to 10^5 Ω, which increased the system bandwidth to ~10^5 Hz. Preliminary results indicated that with normal amplification of the DC signal, risetime electronic delay effects are very significant. The reduction in integrated signal intensity was nearly equal to the factor of 100 reduction in system gain. However, peak widths were broadened, possibly causing excessive integrated signal reproducibility problems. For example, the width of the 12 amu signal, inherently the most narrow ion intensity-time profile, was almost a factor of two narrower at the lower gain setting. In addition, the most probable arrival time for C_1 was 100 μs less. Both these results indicate at least a 100 μs characteristic (instrumental) delay for the higher gain setting. Operation at the lower gain reduces system sensitivity such that the C_5 species data are nearly lost in the noise. Thus, before absolute time-of-arrival data can be collected, and detailed modeling of the time-resolved intensity profile data can be performed, pulse-counting using multichannel scaling will have to be implemented to preserve system

sensitivity and eliminate the system response delay. Consequently, although relative temperatures derived by various models from the low bandwidth data are valid, absolute temperatures are not easily extracted from the present results.

III.4 Effect of Laser Irradiation Energy (Fluence)

A series of experiments were conducted to quantitatively determine the effect of laser fluence on the mass spectrum of carbon polymer species. It was noted earlier [Hastie, et al, 1984] that different experimental series, with only approximately equal laser irradiation energy, all yielded the same thermodynamic temperature, 4200 ± 300 K. This effect could be due to a physicochemical constraint, such as a solid-liquid phase change. Graphite melting temperatures are believed, from literature studies, to fall in the range 4000-4500 K.

The effect of a three-fold variation of laser fluence on the arrival time to molecular weight dependence is given in figure 4. From the curve slopes in figure 4, the temperature is calculated to be essentially constant (see section IV). Since peak widths also did not vary with laser power, the total cooling time also did not apparently change signficantly. A simple T^4 energy loss argument shows that if only the same area were heated, the temperature should have varied by a factor of 1.3, e.g. from 4200 to 5500 K, if 4200 K represents the minimum temperature. Note that the laser beam focus was carefully maintained throughout the series, and the surface was scanned to eliminate possible cratering. Thus we infer that the heated area changes directly with laser fluence at a temperature fixed by the system constraint. Considering the short time scale, the thermal transport probably occurs in a

very narrow surface zone. Otherwise we would expect to see a dependence of time-of-arrival on laser fluence. The observation that the C_2 - C_5 species intensities vary directly with fluence also supports this argument.

The C_1 intensity showed an unexpected square law dependence on the laser fluence, an indication that C_1 is also produced by a photodissociation or similar non-thermal mechanism. This result is particularly surprising in view of our special efforts to minimize laser interaction with the plume--the laser impacts at a shallow angle (15°), the laser pulse time is very short (~10 nsec), and the laser is relatively tightly focused (~250 μ diameter at impact). Hence the photodissociation process must be occuring very early in the vaporization process, or be a laser/surface interaction phenomenon. From simple gas velocity arguments, the known maximum surface temperature of 4200 K [Hastie, et al 1984], and the 10 nsec laser on-time, the entire laser/gas interaction must occur at a distance within 30 μm of the surface. The observation that peak width is also insensitive to laser fluence implies either that the laser heated spot cools at a rate nearly as fast as it heats, or that the photoproduction mechanism is a result of the laser/surface interaction and persists throughout the cooling time. This process undoubtably is responsible for some of the earlier mentioned discrepencies in the literature concerning species ratios. Also, the practical requirement of an enhanced monomer production, to maximize energy dissipation in laser-resistant shielding, may be met naturally as a consequence of the extremely high fluence levels likely to be present.

III.5 Surface Characterization

The apparent change in the vaporization kinetics and beam formation process, as a function of the number of laser pulses, prompted a study of the surface morphology. Both scanning electron microscopy (SEM) and surface profilometry were employed to study the laser irradiated samples.

In typical laser-scanning-mode experimental runs, the samples were translated at ~200 μm/sec, which yields about 95 percent overlap of each successive shot. A portion of the sample was irradiated under these conditions in a single pass. Preliminary SEM observation of the surface indicated that the lack of fiducial marks made it difficult to even identify the path of the laser. Figure 5 is an SEM photograph of a portion of the laser path identified by two fiducial marks manually scribed approximately perpendicular to the laser path, which was readily visible to the naked eye by an interference produced color change on the sample surface. The 15° angle of irradiation should produce an ~400-500 μm "footprint" on the sample. With the aid of the manually scribed fiducial marks, such a "footprint" is barely observable in the SEM micrograph. The graphite grain size can be seen to be on the order of 100 μm in the sample. This small surface change is quite different from the craters generated in the earlier static experiments. Such craters were typically sharp-edged pits of considerable depth relative to the spot size.

The combination of surface roughness and low contrast in the SEM micrograph of figure 5 makes it impossible to estimate the rate of sample removal for the mass spectrometer experiments. In an attempt to provide such data, an automated profilometer study was made of the surface morphology of a portion of the single pass laser path on the sample. The profilometer made repeated scans of the sample across the laser path at 10 μm intervals

for a distance of 4 mm. The result of 100 scans is shown in figure 6. This 3-D isometric plot of the resultant data covers a 1 by 4 mm portion of the surface. The vertical scale is about 75 μm from the bottom of the slice to the average of the surface peaks. From this plot, the surface roughness can be seen to be on the scale of 100 μm across the surface and 25-50 μm into the surface. The laser path is not discernable.

IV. MODELING OF THE THERMAL VAPORIZATION PROCESS.

The original velocity analysis used to establish the equilibrium nature of the vaporization process of the vaporized neutral species is an extremely simplified model. As we noted earlier [Hastie, et al, 1984], the slope of Δt versus $(M)^{1/2}$ provides a measure of temperature, but is unreasonably low.

Previous analysis of the data equated a maximum beam temperature with the fastest arriving C_n species. A more reasonable method to model the gasdynamically expanded beam temperature is to deduce the temperature from the time-of-flight data by assuming that the beam species obey a Maxwellian velocity distribution. The characteristic velocity of a Maxwellian velocity distribution is the most probable velocity as given by:

$$v_{mp} = (2kT/M)^{1/2}$$

where k is Boltzman constant, T is temperature, and M is mass. Converting the velocity distribution to an arrival time distribution, by assuming instantaneous source and response functions, gives a most probable arrival time of :

$$t_{mp} = L\sqrt{m}/2\sqrt{kT}$$

where L is the path length from the sample to the mass analyzer. As in the previous analysis, the assumption of thermal equilibrium requires that t_{mp} vs. $\sqrt{m}$ is linear. The beam temperature can be deduced from the slope of a line drawn through the points of graphs in figures 3 and 4 and is proportional to the slope squared. Only the high bandwidth data (10^5 Ω)

reasonably approximate the instantaneous response assumption. Analysis of the data of figure 4 results in a temperature, averaged over all the data, of 290 ± 50 K. This beam temperature is equivalent to a supersonic expansion cooling factor of about 14 (based on our surface temperature of 4200 K). This degree of cooling indicates an essentially complete gasdynamic cooling from an extremely small region. Such a conclusion is in accord with the small focus zone (~250 μm) and high total graphite vapor pressure (~1 atm).

The time-resolved intensity profiles actually contain the entire thermal history of the laser vaporization process. A better basis for recovering that information is possible by deconvolution of the entire time-of-flight signal, which is an integral of a vapor generation function, a velocity distribution function, and the mass analyser detector function:

$$I(t) = K \underbrace{\int_0^t g(t-\beta)}_{\substack{\text{instrument} \\ \text{reponse} \\ \text{function}}} \cdot \underbrace{\int_0^\beta f(\tau)}_{\substack{\text{arrival} \\ \text{time} \\ \text{function}}} \cdot \underbrace{C[T(\tau)]}_{\substack{\text{partial} \\ \text{pressure \&} \\ \text{temperature}}} \, d\tau \, d\beta$$

The functions in this convolution are:

g(t) is the instrument detector and electronics response function;

f(t) is the arrival time distribution function e.g. for a Maxwellian velocity distribution;

C(T) is the species creation function, dependent on temperature,(T) and time (t);

K is the calibration factor for the number density detector;

I(t) is the observed time dependent ion current signal.

Such a deconvolution has been treated by W.S. Young [1975] for the simple case of a mechanically chopped isothermal beam. He showed that the above convolution accurately models the observed mass spectrometer signals. Current efforts are directed to the development of a parametric computer code to solve the deconvolution by numerical integration for the more complex case of a time-varying (exponential decay) beam source temperature, and a Clausius-Clapeyron type species generation function in place of the simple on-off modulation function of Young [1975]. As a parametric model, it can allow for eventual inclusion of explicit functions for macroscopically important effects such as substrate thermal conductivity, radiation balance, and thermal transport by material loss. However, the surprisingly large influence of the analog MS detector response function (see III.3) will have to be drastically reduced before the model can be implemented. The strong effects of the current response function act as a large noise background to the convolution, making the model's sensitivity to important experimental variables, such as cooling rate, too poor to yield reliable results at present. Methods to minimize the instrument response function using counting techniques are being investigated.

V. SUMMARY AND PLANS

V.1 Summary

A new laser system has been installed and tested. In addition, a two-axis sample stage, which allows for single and multiple shot measurements of selected areas of the sample's surface, has been installed and demonstrated. The laser to sample to mass spectrometer geometry is similar to that of our previous work, where the laser impacts the surface at a shallow angle (~15°) to minimize laser/plume interactions. Emission of vapor

species, however, was noted to occur perpendicular to the surface, was highly forward-peaked, with a much narrower collimation than a COS^2 distribution. These effects were noted even from an uncratered surface.

The observation of thermal equilibrium, reported by us previously for laser-pitted surfaces, was also shown to be characteristic of a surface with "natural" roughness (~25 μm). Abnormally high concentrations of C_1 and, to a lesser extent, C_2, relative to the other C_n species, were found with fresh surfaces. This result is perhaps one cause of the disparate literature results for the relative partial pressures of carbon species. Another contributing factor in this regard is the square-law dependence of C_1 intensity on laser fluence. This behavior is tentatively attributed to a photodissociation process occuring on the surface. It is difficult to distinguish between a laser-vapor interaction and a persistent surface effect until we measure the characteristic cooling time of the surface. The role of surface roughness is clearly a significant factor which needs further investigation.

The temperature reached by the graphite surface, of 4200 ± 300 K, is relatively independent of laser fluence over at least a three-fold power range at 532 nm. It appears that the temperature could be constrained by a physicochemical process, e.g. the thermal halt due to a solid-liquid phase change. This result also indicates that the kinetics of the beam expansion and the internal temperature of the plume are independent of laser energy. Experiments testing the contribution of the mass spectrometer detector response function to the shape of the time-of-arrival spectra show that, at instrument gains necessary to good sensitivity, the bandwidth limitations are

of the same order as the temperature effects. Thus the time-of-arrival data currently provide relative temperatures, with the prospect of extracting absolute temperatures yet to be resolved.

V.2 Plans

In FY-86, we intend to continue studies on the laser energy dependence of the time and mass resolved molecular species from graphites. In order to decouple the instrument response function from the time-of-arrival data, the MS detector system will be adapted to pulse counting, using an appropriate multichannel scaler. This will allow for model analysis of time-of-arrival data to identify and extract, if possible, the source temperature from the expansion Maxwellian velocity distribution.

Preparation will begin for adapting the vacuum system for ion detection. This will involve designing the ion optics to allow passage of thermally ionized species through the differentially pumped apertures.

The surface characterization results indicate that the sample preparation procedure (see section II) is clearly not adequate for these studies if crater formation and material removal rate information is to be obtained. For this reason, diamond polished planchets of high-purity graphite have been obtained. The mirror finish on these samples will be characterized by both SEM and profilometry prior to laser irradiation. Preliminary SEM observations indicate no structural features above submicron size. By eliminating the surface roughness effects in the vaporization process, it will be possible to measure accurate mass removal rates, and provide the gravimetric calibration necessary to obtain accurate partial pressures from scanned surfaces. It should also be informative to follow the carbon species distributions as vaporization proceeds from a clearly surface dominated region to the cratered condition of the static experiment samples.

As surface roughness appears to play a significant role in species distributions, particularly the low mass species of importance in practical applications, graphites with submicron surface smoothness will be studied. In order to investigate the role of surface finish, specimens will be examined after laser irradiation to determine where the vaporization occurs (perhaps at grain boundaries).

The slight off-axis sampling geometry used (see section II) may favor beam segregation with an apparent loss of the heavier species. For this reason, we are modifying the MS system to allow for true perpendicular (on-axis) molecular beam sampling. We intend to test geometries where the laser beam is also perpendicular to the sample surface, and hence co-axial with the molecular beam, in addition to conditions where the beam strikes at low angles to a surface perpendicular to the MS beam axis. We will also examine the possibility of folding the laser path within the vacuum system for perpendicular beam extraction and low angle laser irradiation.

Because of the difficulty of real-time pyrometry on a submicrosecond time scale, we intend to investigate the persistance time of the residual hot spot on the surface after the laser pulse terminates. Filtered high speed photodiodes will be used to used to observe the hot spot and the plume, with simultaneous recording of photodiode output and MS signal to allow correlation of the vaporization process with the laser pulse and subsequent history.

Because metal carbides are a attractive potential protective material, initial survey studies of TaC, as an example, will also be undertaken.

VI. ACKNOWLEDGEMENTS

We would like to thank A.C. Van Orden and E. Whitenton of the NBS Metallurgy Division for their aid in SEM and surface profilometry measurements. A.B. Sessoms and M. Wilke have provided valuable technical assistance in the construction and maintenance of the laser-induced vaporization mass spectrometric facility.

VII. REFERENCES

R.L. Baker and J.W. Hager, AFOSR Report No. TOR-0084A(5651-01)-1, (The Aerospace Corp. El Segundo, CA, 1 Oct 1984).

C.M. Stickley, "Laser Countermeasures Development (LCMMD) Program Review," The BMD Corp., May 15-16, 1985.

JANAF Thermochemical Tables, 2nd Ed., NSRDS-NBS 37 (Washington, DC, 1971) and supplements (e.g. J. Phys. and Chem. Ref. Data, 1974, pp. 311-480; 1975, pp. 1-175; 1978, pp. 793-940; 1982, pp. 695-940).

R.L. Baker, M.A. Covington, and G.M. Rosenblatt, High Temperature Materials Chemistry-II, 83-7, ed. Munir and Cubicciotti, (Electrochem. Soc., Pennington, NJ, 1983) pp. 143-154.

M.A. Covington, G.N. Liu, and K.A. Lincoln, AIAA J. 15, 1174 (1977).

K.A. Lincoln and M.A. Covington, Int. J. Mass Spec. Ion Phys. 16, 191 (1975).

J.H. Lundell and R.A. Dickey, Progr. Astron. and Aeron. 56, 405 (1977).

J.H. Lundell, Progr. Astron. and Aeron., 83, 472 (1982).

R.T. Meyer, A.W. Lynch, and J.M. Freese, J. Phys Chem. 77, 1083 (1973).

T.A. Milne, J.E. Beachey, and F.T. Greene, J. Chem. Phys., 57, 2221-2222 (1972).

M.A. Scheindlin, Institute of High Temperatures, USSR Academy of Sciences, unpublished (1984).

P.D. Zavitsanos, Carbon 6, (1968).

J.W. Hastie, D.W. Bonnell, and P.K. Schenck, AFOSR Annual Report, NBSIR84-2983 (1984).

J.J. Clarke and B.R. Fox, J. Chem. Phys., 51, 3231 (1969).

F.M. Wachi and D.E. Gilmartin, Carbon 8, 141 (1970).

W.S. Young, J appl. Phys., 46 (1975).

Table 1. Comparison of Ion Intensity Data for Scanned and Fixed Sample Positioning

C_n	Mass (amu)	Average[a]	σ_M[a]	C_n/C_3 (Scanned)	C_n/C_3 (Static)[b]
1	12	143000	32000	0.6300 ± 0.100	0.320
2	24	32000	13000	0.1400 ± 0.060	0.110
3	36	227000	4400	1.0000 ± 0.020	1.000
4	48	2470	510	0.0110 ± 0.002	0.013
5	60	2450	610	0.0110 ± 0.003	0.027
6	72	557	250	0.0025 ± 0.001	
7	84	1730	1500	0.0076 ± 0.007	
8	96	1900[c]	1600	<0.008 ± 0.007	
9	108	600[c]	2000[d]	<0.003 ± 0.009	

Footnotes:

a) Units are approximately total ion events/laser shot, using an estimated factor to convert from the digitized analog signal. Data taken at ~26 eV using 10^7 Ω input impedence with 37 mJ pulses (see text). σ_M is the standard deviation of the mean for three sets of data.

b) From the 26 eV data in [Hastie, et al, 1984].

c) Values represent upper limits due to difficulty in making the base line correction (≤ 40% overestimate).

d) Error estimate based on similarity to C_7 and C_8 uncertainty.

Figure Captions:

(1) Schematic of laser-induced vaporization mass spectrometric facility (side view), showing laser-sample-molecular beam geometries. The microcomputer system shown controls the signal averager and the instantaneous position of the sample mount/translator. Completed scans are recorded and then replotted by a minicomputer. A typical recent time-resolved intensity profile for mass 12 amu is shown, indicating good signal/noise.

(2) Dependence of integrated signal intensity (per laser shot) versus accumulated number of laser shots for a "static" (see text) graphite sample position. Data were recorded for C_n^+ (n=1 to 5) for 1000 shots each, then repeated to monitor the fall-off in signal intensity with accumulated number of laser shots. The laser fluence was held constant at 37 mJ/shot during the runs.

(3) Dependence of the most probable time-of-arrival (signal peak) versus the square root of mass for C_n^+ (n=1 to 5) ions. The linear correlation suggests local thermodynamic equilibrium of the beam species. This equilibrium is essentially unchanged with accumulated number of laser shots on a static graphite sample. A high-gain (10^7 Ω) input impedance was used.

(4) Dependence of the most probable time-of-arrival (signal peak) versus the square root of mass for C_n^+ (n=1 to 5) ions for varying laser fluence on a scanned graphite sample. The input gain impedance was 10^5 Ω. Note that the variation of arrival time with laser fluence is less than the repeatability demonstrated by the replicate set of 37 mJ data.

(5) SEM micrograph of laser track across a scanned graphite target. The laser path (see arrow) is approximately perpendicular to the two deep manually scribed fiducial marks which are the most prominant features in the micrograph. The two arrows mark the direction and apparent edges of the laser track. The scale marker is 100 μm.

(6) Isometric plot of data obtained from an automated profilometer study of the laser path on the scanned graphite target of figure 5. The base of the plot is 1 by 4 mm and the average vertical height is 75 μm. The laser path is parallel to the 1 mm side, as shown by the arrow. However the path cannot be discerned in this figure. See text for discussion.

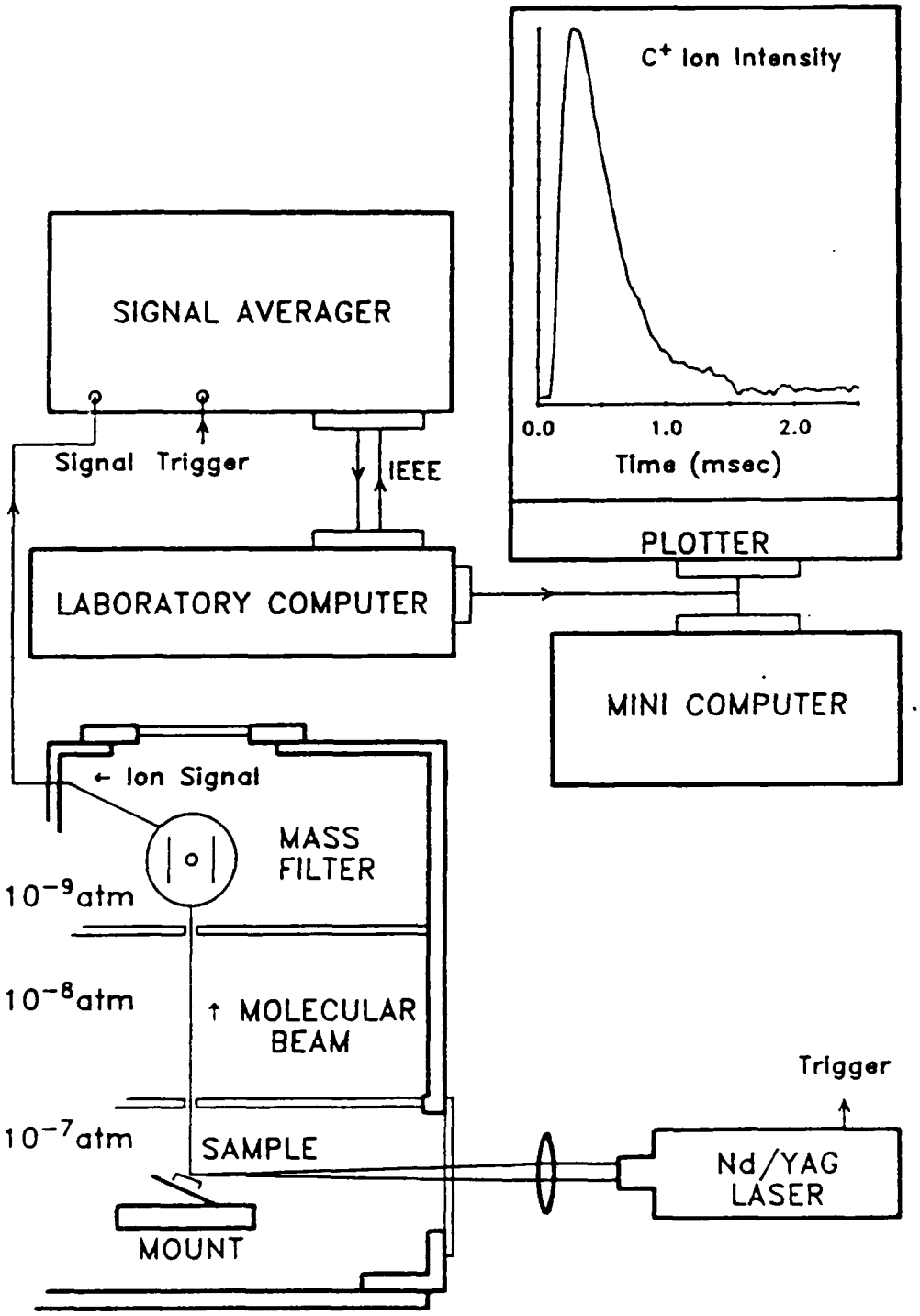
C+ Ion Intensity
0.0
1.0
2.0
Time (msec)
SIGNAL AVERAGER
Signal
Trigger
IEEE
PLOTTER
LABORATORY COMPUTER
MINI COMPUTER
← Ion Signal
MASS FILTER
10−9atm
10−8atm
↑ MOLECULAR BEAM
Trigger
10−7atm
SAMPLE
Nd/YAG LASER
MOUNT

FIGURE 1.

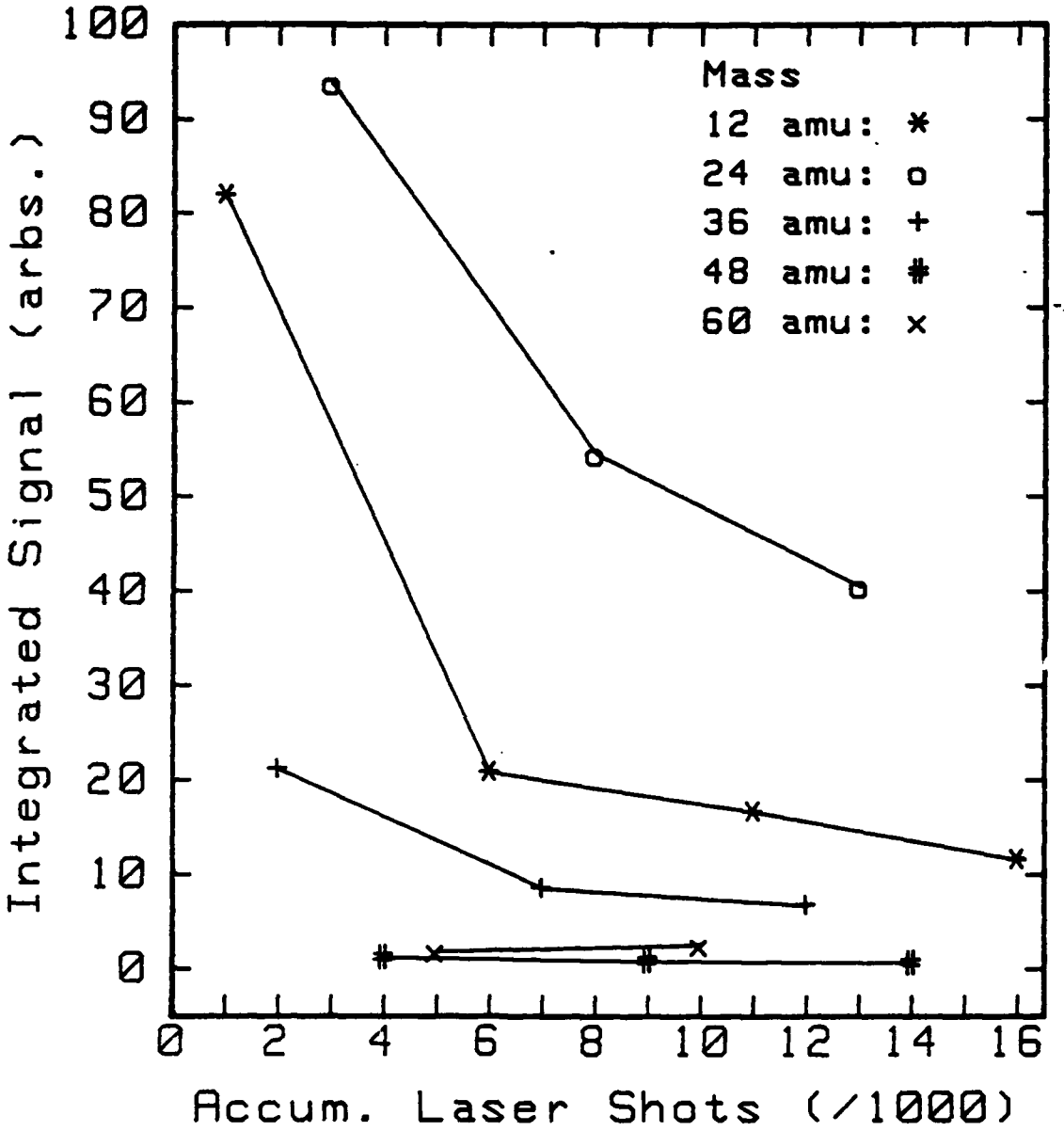
Mass
12 amu: *
24 amu: o
36 amu: +
48 amu: #
60 amu: x
Integrated Signal (arbs.)
100
90
80
70
60
50
40
30
20
10
0
0
2
4
6
8
10
12
14
16
Accum. Laser Shots (/1000)

FIGURE 2.

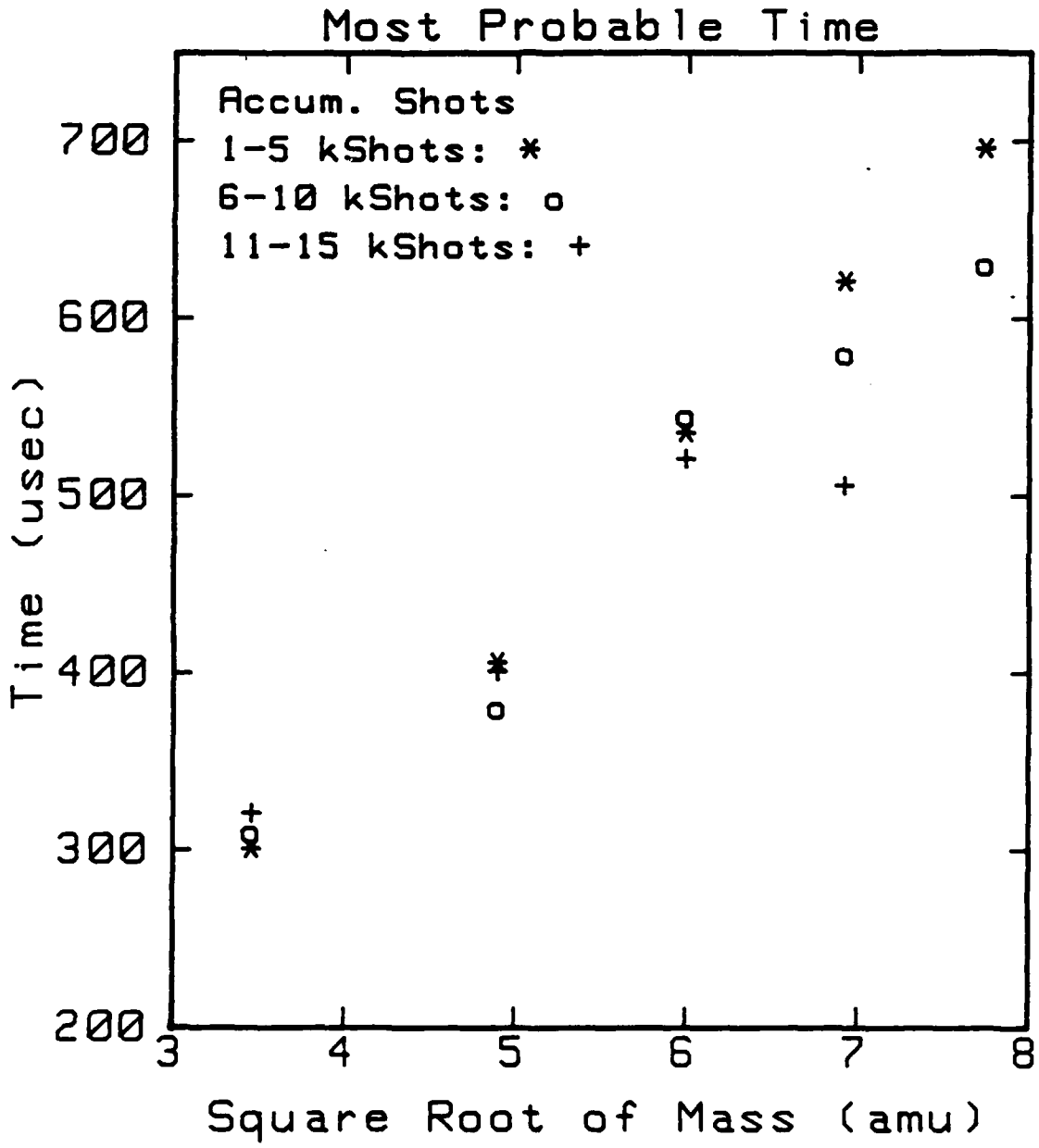
Most Probable Time
Accum. Shots
1-5 kShots: *
6-10 kShots: o
11-15 kShots: +
700
600
500
400
300
200
Time (usec)
3
4
5
6
7
8
Square Root of Mass (amu)

FIGURE 3.

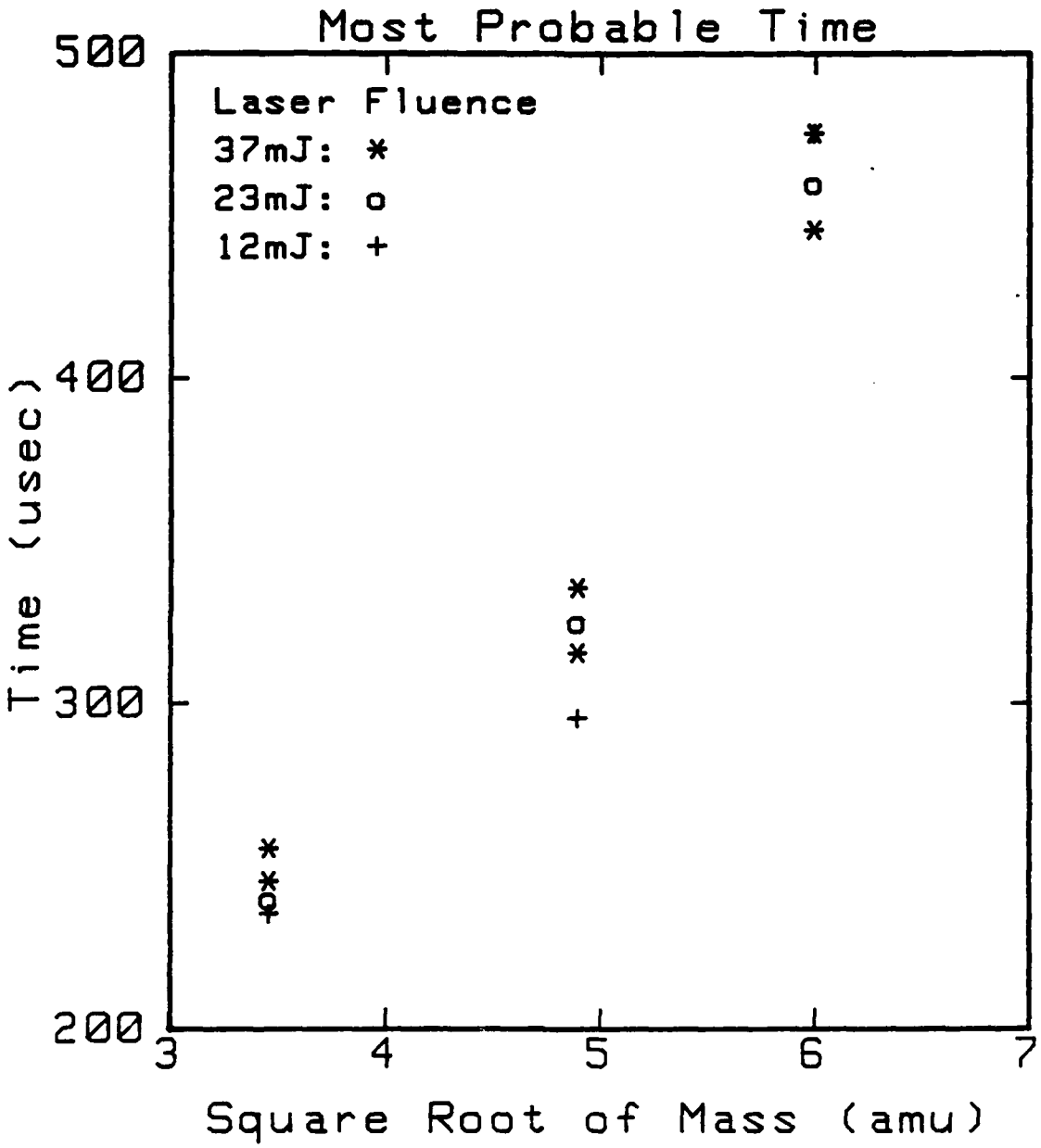
Most Probable Time
Laser Fluence
37mJ: *
23mJ: o
12mJ: +
500
400
300
200
Time (usec)
3
4
5
6
7
Square Root of Mass (amu)

FIGURE 4.

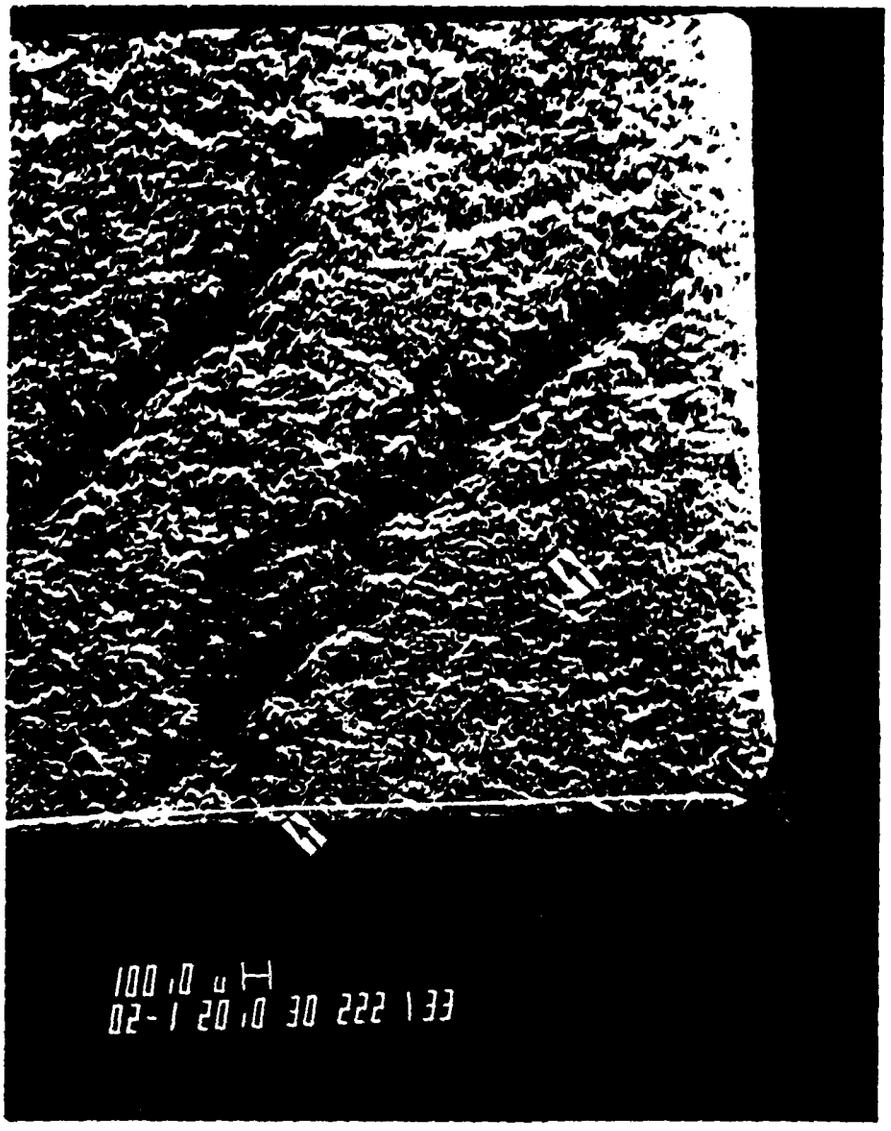

FIGURE 5.

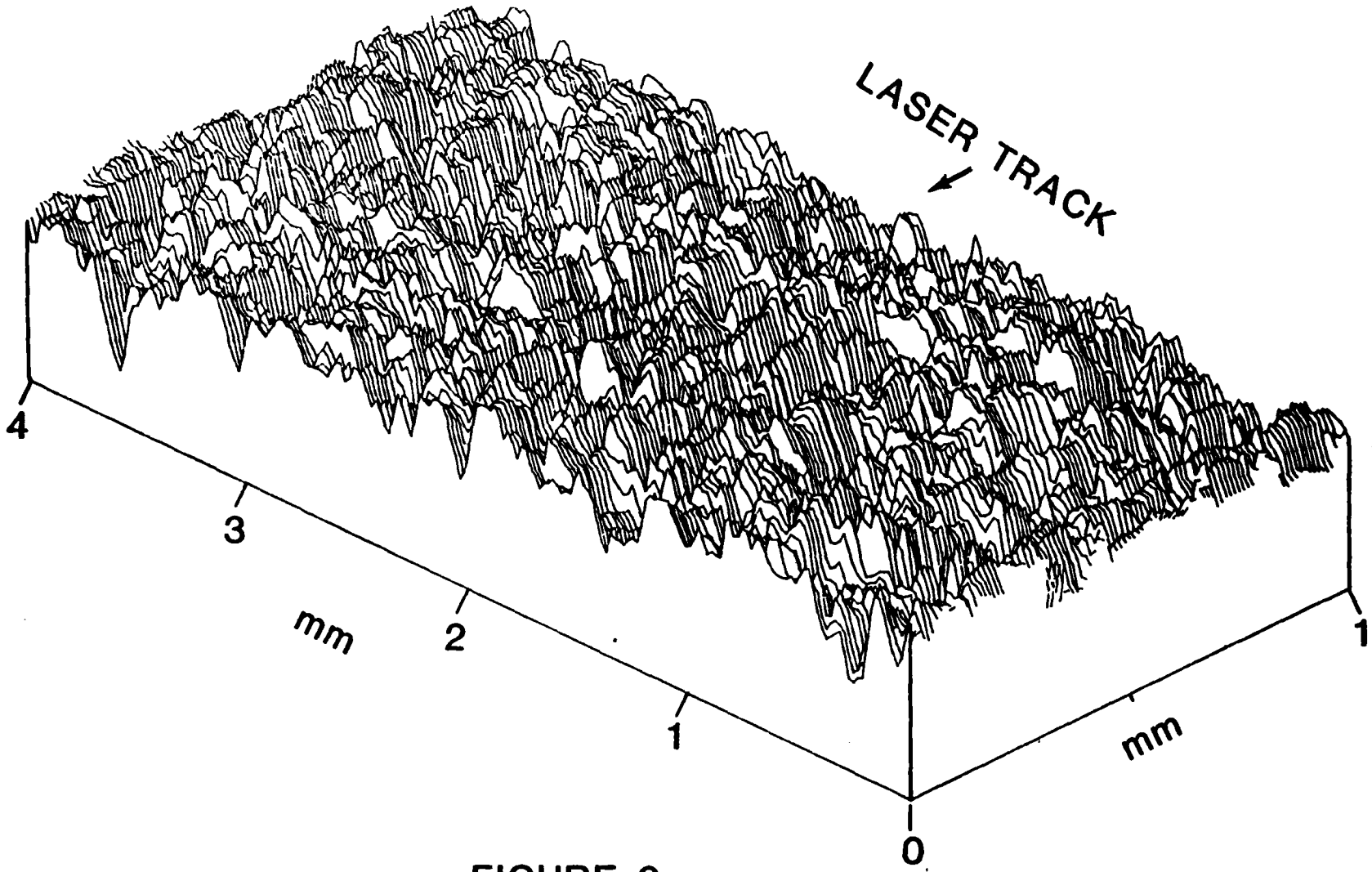

FIGURE 6.

END

FILMED

3-86

DTIC